UNIVERSITY OF OKLAHOMA

GRADUATE COLLEGE

INFLUENCE OF THERMOPLASTIC POLYMER TYPE ON INTERLAYER SHEAR STRENGTH BETWEEN EXOTHERMIC OVERLAYS AND EXISTING SUBSTRATES FOR RAPID BRIDGE DECK PROTECTION

A THESIS

SUBMITTED TO THE GRADUATE FACULTY

In partial fulfillment of the requirements for the degree of

MASTER OF SCIENCE

By

MUMTAHEENA REZA

Norman, Oklahoma

2026

INFLUENCE OF THERMOPLASTIC POLYMER TYPE ON INTERLAYER SHEAR STRENGTH BETWEEN EXOTHERMIC OVERLAYS AND EXISTING SUBSTRATES FOR RAPID BRIDGE DECK PROTECTION

A THESIS APPROVED FOR THE

SCHOOL OF CIVIL ENGINEERING AND ENVIRONMENTAL SCIENCE

BY THE COMMITTEE CONSISTING OF

Dr. Shreya Vemuganti, Chair

Dr. Royce Floyd

Dr. Syed Ashik Ali

Dedication

I dedicate this thesis to my family for their endless love, encouragement, and support throughout my academic journey. A special dedication goes to my husband, Md Mushfique Us Saleheen, for his constant motivation, patience, encouragement, and unwavering support during every stage of this work. His belief in me gave me the strength to overcome every challenge throughout this journey.

I also dedicate this work to my advisor, Dr. Shreya Vemuganti, for her endless support, guidance, and encouragement in helping me succeed throughout this research journey.

Acknowledgement

I would like to express my sincere gratitude to my advisor, Dr. Shreya Vemuganti, for her continuous guidance, support, encouragement, and motivation throughout this research journey. Her valuable advice and mentorship made this work possible, and I feel truly honored to work under her supervision.

I would also like to thank my committee members, Dr. Syed Ashik Ali and Dr. Royce W. Floyd, for their support, guidance, and valuable suggestions throughout this study.

I sincerely thank Mr. John Bullock for assisting me in conducting the experimental work throughout the program, and Mr. Kenneth Hobson for sharing his valuable knowledge and providing technical guidance during the laboratory work.

I would also like to thank my research team members, Benjamin K. Abu, Brandon Vu, Nawaraj Rai, Nazeefa Tasneem, Axel Josue Segura Alvarado, Luis G. Urbina Barrios, and Sijan Adhikari, for helping me during specimen fabrication, casting, and experimental testing.

Lastly, I sincerely acknowledge Mujtaba Ahmadi and Omar Yadak for assisting and training me throughout this work. I would also like to express my heartfelt gratitude to my husband, Md Mushfique Us Saleheen, for constantly motivating, encouraging, and supporting me whenever needed.

Abstract

Interlayer bonding plays a key role in the long-term performance and durability of bridge deck overlay systems. Weak bonding between overlay and substrate layers can result in premature failures such as de-bonding, reflective cracking, slippage, and delamination. This study evaluated the influence of different thermoplastic fiber-reinforced polymer (FRP) tapes and woven polymer lattice systems on the interlayer shear strength (ISS) performance of asphalt-asphalt (A-A), portland cement concrete-portland cement concrete (PCC-PCC), and portland cement concrete-polymer concrete (PCC-PC) systems. In the pilot study, different thermoplastic FRP systems, including C-PA6, C-PA410, G-PETG, G-PP, and G-HDPE, were evaluated using the Louisiana Interlayer Shear Strength Test (LISST). In addition, lattice systems with different opening sizes were investigated in slab-scale specimens. The effects of polymer type, tack coat application, fiber orientation, heating condition, and lattice opening size were studied. The results demonstrated that polymer type and lattice geometry significantly influenced interlayer bonding performance. G-PETG exhibited the highest ISS performance in the asphalt pilot study specimens, while G-PP demonstrated the best performance in PCC-PCC specimens. In PCC-PC specimens, C-GPETG showed the highest ISS because of strong embedment within the polymer concrete overlay. For slab specimens, the 1 in. × 1 in. opening configuration consistently exhibited better performance than the 1 in. × 0.5 in. configuration. PETG-based systems showed better performance in concrete slabs, whereas HDPE-based systems performed better in asphalt slab specimens. Overall, the findings demonstrated that thermoplastic FRP reinforcement systems have strong potential for improving interlayer bonding and enhancing the durability of bridge deck overlay systems and multilayer pavement structures.

Table of Contents

List of Figures

List of Tables

Chapter 01. Introduction

1.1 Background

Bridge decks are highly vulnerable to cracking and reinforcement corrosion under traffic and environmental stresses [1-4]. Bridge deck overlays are widely used as rehabilitation and preservation treatments to protect existing bridge decks from further deterioration, improve surface characteristics, restore structural functionality, and extend service life. By limiting the ingress of water, chlorides, and other deleterious substances, overlays help reduce reinforcement corrosion and delay the progression of deck deterioration [5]. The bond at the deck-overlay interface is critical for long-term performance. Monolithic behavior and efficient stress transfer are enabled by a strong bond, whereas insufficient bonding results in independent layer action and accelerated deterioration [6-8]. Distresses, including slippage, delamination, rutting, and reflective cracking, are caused by de-bonding, resulting in reduced service life and increased maintenance costs [9-16]. It has been demonstrated in previous studies that the quality of the interface bond plays a critical role in the initiation and progression of reflective cracking, with its development being accelerated by weaker bonds [17, 18].

The interface is mechanically complex, with stresses being induced by relative motion between layers and influenced by material properties, temperature, moisture, and surface preparation [19-22]. Although tack coats, membranes, and grids have been used to enhance adhesion, their performance is often inconsistent under real service conditions [23-25]. Consequently, weak interlayer bonding is regarded as a leading cause of premature failures, emphasizing the need for more reliable solutions capable of sustaining composite action over time. Therefore, this thesis investigates the interlayer bonding performance of bridge deck overlays incorporating thermoplastic FRP tapes.

1.2 Research Gap

Although previous studies have investigated conventional interlayer bonding techniques, including tack coats, fiber grids, and membrane systems, limited research has been conducted on the use of different types of thermoplastic fiber-reinforced polymer (FRP) lattice-like membrane systems as interlayer reinforcement materials for bridge deck protection applications. In particular, the influence of thermoplastic polymer type and lattice opening size on interlayer shear strength, stress transfer behavior, and interface failure mechanisms has not been comprehensively evaluated. Existing studies have primarily focused on conventional asphalt overlay systems, while limited attention has been given to exothermic overlay systems, such as polymer concrete overlays, where rapid curing behavior and thermal effects may significantly influence interfacial performance. In addition, the interactions between thermoplastic reinforcement systems and different substrate-overlay combinations remain insufficiently understood. Therefore, a need exists to investigate the influence of thermoplastic FRP membrane systems on the interlayer bonding performance of bridge deck overlays to support the development of more durable and reliable rapid rehabilitation solutions.

1.3 Scope of Research

This study evaluates the use of thermoplastic unidirectional FRP tapes as interlayer membranes in bridge deck overlays. The research focuses on assessing interlayer bonding through shear-strength testing of asphalt and epoxy polymer overlays and on estimating the potential for extended service life of bridge decks.

Chapter 02. Literature Review

2.1 Shear Stress Development at Substrate-Overlay Interfaces

Shear stress is defined as the internal resisting force developed parallel to a surface when external forces attempt to cause relative sliding between adjacent material layers. Unlike normal stress, which acts perpendicular to a plane, shear stress acts tangentially along the plane of interest [26, 27]. The average shear stress acting on a plane may be expressed as:

$$\tau = \frac{F}{A} \quad [1]$$

Where,

τ = Shear stress,

F = Applied force,

A = Area of cross-section

In structural systems, shear stresses are generated when components are subjected to transverse loading, bending, torsion, differential settlement, or incompatible deformation between connected elements. The development of shear stress represents the internal resistance of a material against sliding deformation and is essential for maintaining structural equilibrium and continuity. The magnitude and distribution of shear stress are influenced by the applied loading conditions, geometry of the structural system, support conditions, and mechanical properties of the materials involved. In layered systems, shear stress becomes particularly important because stresses must be transferred efficiently between adjacent layers to maintain composite action and structural stability [26-31].

In multilayer structural systems, including bridge deck overlays, interfacial shear stresses develop at the boundary between the overlay and substrate when differential movement occurs between the two bonded layers [2,4]. Under traffic loading, wheel loads induce repeated bending, compression, and horizontal shear forces within the overlay system [2,3]. As vehicles move across the bridge deck surface, vertical and horizontal stresses are generated within the overlay and substrate layers, causing differential deformation between the bonded materials [3,5]. Since the overlay and substrate often possess different mechanical and thermal properties, incompatible deformation behavior may develop under loading conditions [4,5]. Consequently, shear stresses are continuously generated at the overlay-substrate interface to resist relative sliding and maintain strain compatibility between the bonded layers [2].

Although bridge deck overlays are primarily used for deck preservation and rehabilitation, they behave mechanically as layered pavement systems. Traffic loads applied at the surface must be transferred through the overlay and across the deck–overlay interface, making interlayer bonding a critical factor governing structural performance and durability [32]. Rigid (concrete) and flexible (asphalt) pavement systems transfer and distribute applied traffic loads differently due to variations in material stiffness and structural behavior. Concrete pavements generally exhibit higher stiffness and distribute loads over a wider area, whereas asphalt pavements transfer loads through layered deformation within the pavement structure. These differences in load transfer behavior influence stress distribution and interfacial shear stress development within overlay systems. Figure 1 illustrates the load distribution mechanisms in rigid and flexible pavement systems.

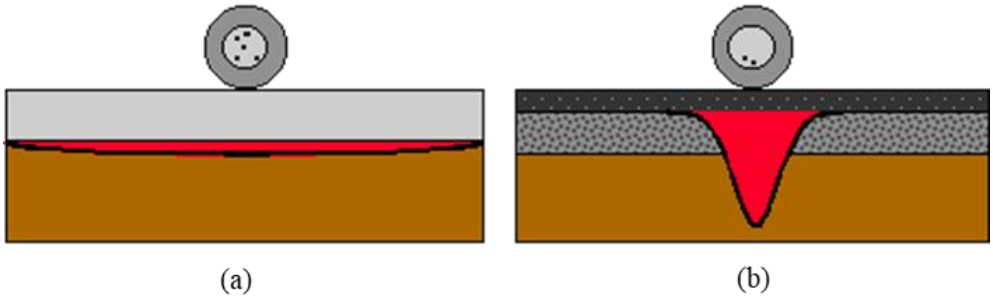

Figure 1: Load Distribution Mechanism in Rigid and Flexible Pavement, (a) Concrete (Rigid) Pavement, (b) Asphalt (Flexible) Pavement [33]

2.2 Interlayer Bonding and Shear Performance in Structural Overlays

The structural performance of composite pavements and bridge decks is strongly influenced by the bonding condition at the interface between layers. Whether the system behaves monolithically or independently is governed by the bond.

When a strong bond exists between the overlay and the substrate, the system exhibits monolithic behavior, meaning that loads applied at the surface are uniformly distributed throughout all layers. In this case, shear stresses at the interface are minimized, and tensile strains are primarily concentrated at the bottom of the overlay layer, where they can be controlled through design [9]. Efficient stress transfer results in a reduction of localized overstressing and a delay in crack initiation. In contrast, when the bond is weak or absent, the overlay and substrate behave independently. Rather than acting together, each layer carries the load individually, leading to discontinuities in stress distribution. Consequently, tensile strains are developed at the bottom of both the overlay and the substrate, while compressive strains are concentrated at the top surfaces. This shift in the stress–strain distribution creates zones of overstressing. Such effects accelerate fatigue, slippage, rutting, and reflective cracking, ultimately resulting in premature deterioration and increased maintenance requirements [11-15, 17, 18]. This mechanism is shown in Figure 2.

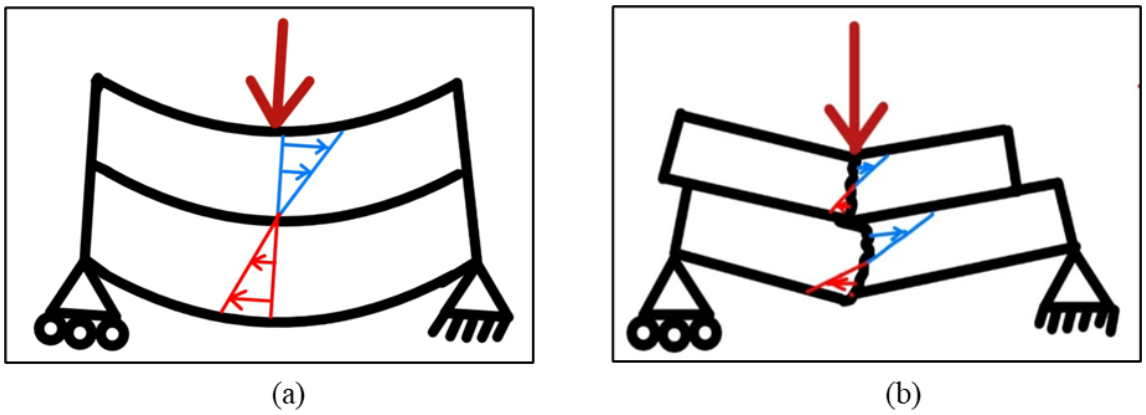

Figure 2: Layered system behavior under- (a) Monolithic Case, (b) De-bonding Case [10]

Similar issues are observed in bridge deck overlays. Bridge decks are exposed to cracking and reinforcement corrosion due to dynamic vehicular loading and environmental conditions [1-3, 22]. Environmental effects, including temperature fluctuations, moisture infiltration, drying shrinkage, and freeze-thaw cycling, further contribute to interfacial shear stress development within bridge deck overlay systems [27, 29, 30]. Thermal expansion and contraction may cause the overlay and substrate to deform at different rates due to differences in thermal properties, resulting in additional shear stress concentration at the interface [27]. The durability of the deck overlay system is dependent on the interlayer shear strength, which is reduced when relative motion between bonded materials generates stress concentrations [19-22].

2.3 Interlayer Failure Modes

Interlayer failure modes refer to the different modes through which deterioration and separation occur at the boundary between overlay and substrate layers in multilayer structural systems.

One of the most common interlayer failure modes is adhesive failure, which occurs when separation develops directly at the interface between two bonded materials [29-31]. In this type of

failure, the bond between the overlay and substrate becomes insufficient to resist applied stresses, resulting in de-bonding or slippage between the layers. Adhesive failure is often associated with inadequate surface preparation, insufficient tack coat application, contamination, moisture presence, or poor compatibility between the overlay and substrate materials [28, 31].

Cohesive failure occurs when cracking or fracture develops within one of the materials adjacent to the interface rather than directly along the interface itself [30]. In this case, the interfacial bond remains stronger than the internal strength of the overlay or substrate material. Cohesive failure may develop within asphalt overlays, polymer concrete overlays, or concrete substrates, depending on the relative material properties and stress distribution within the system [29]. This type of failure is generally considered indicative of stronger interlayer bonding compared to adhesive failure [28].

Delamination is another major interlayer failure mechanism commonly observed in bridge deck overlays. Delamination refers to the progressive separation of overlay layers from the substrate due to repeated loading, moisture intrusion, freeze-thaw action, or thermal cycling [27, 29, 30]. Once delamination initiates, load transfer efficiency across the interface decreases significantly, leading to localized stress concentration and accelerated deterioration of the overlay system. Delaminated regions may further develop stripping, cracking, or large-scale overlay separation under continued traffic loading [28].

Slippage failure may also occur when insufficient shear resistance exists at the interface. Under braking, acceleration, or turning movements of vehicles, horizontal shear forces are generated within the overlay system. If the interface cannot adequately resist these forces, relative sliding between the overlay and substrate may occur, resulting in permanent displacement, surface distortion, rutting, or cracking [28, 30, 31]. Slippage failures are particularly critical in asphalt overlay systems due to the viscoelastic nature of asphalt materials and their susceptibility to

temperature-dependent deformation [31]. An example of slippage failure is shown below in Figure 3.

Figure 3: Slippage Failure [34]

Reflective cracking is another important distress associated with interlayer failure mechanisms [27, 29]. Reflective cracks initiate from existing cracks or joints within the underlying substrate and propagate upward through the overlay due to repeated traffic loading and thermal movement [28]. Weak interfacial bonding may accelerate crack propagation by reducing the ability of the interface to redistribute stresses and maintain composite action between layers [30]. Consequently, reflective cracking is strongly influenced by interlayer bonding quality and interface stiffness characteristics. Reflective cracking in an asphalt pavement is shown below in Figure 4.

Figure 4: Reflective Cracking

The development of interlayer failure mechanisms is influenced by several factors, including material properties, surface roughness, moisture condition, temperature variation, loading frequency, overlay thickness, and interlayer reinforcement systems [28-31].

2.4 Role of Overlays

Overlay systems are utilized in bridge maintenance and rehabilitation to restore structural capacity, improve ride quality, and protect decks from environmental deterioration. Among these systems, asphaltic, cementitious, and polymer-modified overlays are characterized by distinct material properties and performance behaviors that influence their overall durability in service [35].

2.4.1 Asphalt Systems

Asphalt overlays are typically constructed with a thin asphalt surface placed over base and subbase layers of gravel or stone, supported by a compacted subgrade. Asphalt requires multiple layers and greater thickness for effective load transmission to the subgrade. In design, the structural performance of flexible pavements depends on the combined strength of all layers [33].

Asphalt continues to be widely utilized owing to its low initial cost, rapid construction, and ability to provide a smooth driving surface. Its flexibility allows small variations in terrain and temperature to be accommodated without cracking. However, shorter service life and more frequent maintenance requirements are associated with asphalt pavements, particularly in hot climates where bitumen may soften and deform. Despite these limitations, global pavement construction is still dominated by asphalt because of its affordability, recyclability, and ease of repair [36].

2.4.2 Polymer Concrete Systems

Polymer concrete (PC) overlays are regarded as a durable and lightweight alternative for bridge decks because of their superior wear resistance, skid resistance, and waterproofing capability. Typically applied in thin layers of 0.5-0.75 inches, PC overlays are characterized by rapid curing, often permitting traffic resumption within three hours, which makes them suitable for accelerated bridge construction. They also serve as protective barriers against galvanic corrosion and eliminate the need for additional corrosion-resistant primers on reinforcing steel. However, premature failures, including delamination and vertical cracking, have been reported when PC overlays are applied to Portland Cement Concrete (PCC) substrates [37-39]. Delamination is primarily caused by mismatched thermal expansion coefficients between the PC overlay and the PCC base, resulting in thermal stresses being induced at the interface and weakening of the bond [40].

2.4.3 Ultra High Performance Concrete

Ultra-High Performance Concrete (UHPC) overlays have gained significant attention for bridge deck rehabilitation and preservation because of their superior mechanical properties and

durability [41]. UHPC typically exhibits compressive strengths exceeding 120 MPa, substantially greater than those of conventional concrete. In addition, its dense microstructure provides extremely low permeability and chloride diffusivity, limiting the ingress of moisture and chlorides that contribute to reinforcement corrosion [42]. As a result, UHPC overlays can enhance bridge deck durability, improve structural performance, and extend service life while requiring relatively thin overlay sections [41]. However, the long-term performance of UHPC overlay systems remains highly dependent on the quality of the bond developed between the UHPC overlay and the existing concrete substrate. In bridge deck applications, the interface can be subjected not only to shear stresses generated by traffic loading but also to tensile stresses normal to the interface arising from UHPC shrinkage, temperature fluctuations, and wheel-load-induced blister action. Previous studies have shown that the tensile bond strength between fresh UHPC and existing concrete is influenced by several factors, including substrate surface preparation, the use of bonding agents, the mechanical properties of the overlay and substrate materials, and the testing method used to evaluate bond performance [43-45].

2.5 Thermal Behavior and Heat Generation in Overlay Systems

During asphalt overlay placement, asphalt mixtures are produced and compacted at elevated temperatures to ensure sufficient workability and compactibility. Hot mix asphalt is typically placed at temperatures ranging from approximately 135°C to 165°C, depending on binder grade and mixture design [46, 47]. After placement, heat loss occurs rapidly due to convection, conduction, and radiation between the asphalt layer and the surrounding environment. Heat is transferred from the hot asphalt mixture to the cooler underlying substrate, ambient air, and construction equipment, resulting in progressive temperature reduction within the overlay layer. Depending on haul distance, ambient temperature, wind conditions, layer thickness, and substrate

temperature, asphalt mixtures may experience temperature losses ranging from approximately 3°C to 14°C (5°F to 25°F) during transportation and placement operations [47-49]. Additional rapid cooling occurs after laydown due to heat transfer from the asphalt layer to the cooler surrounding air and underlying substrate. Thin asphalt layers are particularly susceptible to accelerated heat loss because of their lower thermal mass. Excessive temperature loss during placement may reduce compaction efficiency, increase mixture stiffness, and shorten the available compaction window [46-48].

Laboratory compaction is typically completed within a very short duration, generally in less than 5 minutes. This differs significantly from field compaction operations, where various roller types, rolling sequences, and pass patterns are employed, and where the target density may not be achieved until 30 minutes or more after the asphalt mixture has been placed by the paver. In addition, the asphalt mixture temperature remains relatively stable during laboratory compaction. In contrast, the pavement mixture in the field continuously loses temperature over time. Under laboratory conditions, compaction is generally performed before the mixture temperature decreases below approximately 115°C (240°F) for the Marshall and Superpave methods, depending on binder viscosity characteristics, or below 105°C (220°F) for the Hveem method. However, in field applications, the mixture temperature may decrease to nearly 80°C (175°F) before compaction has been fully completed [49].

In contrast to asphalt overlays, polymer concrete overlays generate heat internally through exothermic chemical reactions during curing. Polymer concrete systems commonly consist of polymer binders, such as methyl methacrylate (MMA), polyester, or epoxy resins, combined with mineral aggregates [50, 51]. During curing, polymerization reactions occur within the binder system, releasing thermal energy and causing a rapid increase in material temperature. Depending on the resin system, catalyst concentration, overlay thickness, and environmental conditions,

significant temperature increases may occur within the overlay layer. Previous studies have reported that MMA polymer concrete systems may develop peak exothermic temperatures ranging from approximately 60°C to over 120°C, depending on resin formulation, catalyst dosage, overlay thickness, and environmental conditions. In highly reactive systems or thicker overlay applications, localized temperatures may become even higher due to reduced heat dissipation during curing. The rapid heat generation associated with MMA overlays contributes to accelerated curing and early strength development, enabling rapid reopening of bridge decks to traffic [50-52].

2.6 Current Interlayer Systems

Tack coats remain the most widely used method for improving interlayer bonding in multilayer pavement systems.. These are typically composed of modified emulsified asphalt, valued for their ease of application and compatibility with overlays [25, 53-55] . Despite their popularity, field performance is inconsistent, with bond strength being influenced by factors such as surface texture, application rate, curing time, and environmental conditions [25, 56-65]. Other reinforcement systems, such as paving fabrics, Stress Absorbing Membrane Interlayers (SAMIs), and geotextiles, are used to delay crack propagation; however, lower shear and tensile strengths have been reported compared to control sections. Performance is generally improved when the substrate surface is milled before application [23, 62, 66].

Geogrids, particularly glass and polymeric types, have gained attention as reinforcement materials to improve stress distribution across overlays [23, 24, 64, 65]. Glass fiber geogrids are known for their high thermal and chemical stability and for possessing a modulus nearly twenty times greater than that of asphalt concrete, allowing stress to be distributed more effectively [25]. The open-mesh structure of glass fiber geogrids allows aggregate interlock, resulting in improved load transfer between asphalt layers and reduced shear potential. Bonding performance and

installation efficiency are further enhanced through the application of coatings and tack films [65]. Fiberglass grid placed on the pavement as reinforcement, followed by tack coat application to improve bonding with the overlay, is shown below in Figure 5.

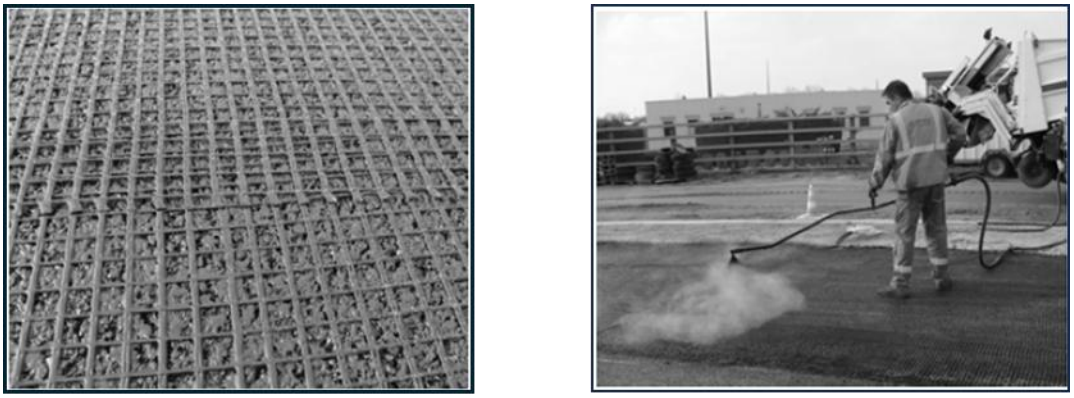

(a) (b)

Figure 5: (a) Fiber Glass Grid Placed on the Pavement, (b) Tack coat Application

In full-scale testing, the presence of a fiberglass grid significantly improved fatigue resistance; the unreinforced section exhibited approximately 70 percent cracking after 1.2 million load cycles, whereas the reinforced section showed no cracking over the same loading period, indicating a very substantial performance improvement. Similarly, in thin overlay maintenance experiments, sections without grid reinforcement became fully cracked, while the grid-reinforced section exhibited only about 10 percent cracked surface after 3.3 million loads, corresponding to roughly a 90 percent reduction in cracking extent. Paving fabrics, while effective for moisture control, mitigation of reflective cracking, and fatigue cracking, have often exhibited poor bonding with asphalt [23, 25].

Fiber-Reinforced Polymer (FRP) materials are composite materials consisting of high-strength reinforcing fibers embedded within a polymer matrix. The reinforcing fibers primarily provide strength and stiffness, while the polymer matrix functions as a binding material that transfers stresses between fibers and protects the reinforcement from environmental and

mechanical damage [67, 68]. Due to their high strength-to-weight ratio, corrosion resistance, and favorable mechanical properties, FRP materials have been increasingly utilized in civil infrastructure applications, including bridge rehabilitation, pavement reinforcement, structural retrofitting, and overlay systems [68, 69]. A comparison of FRPs and mild steel is illustrated in Figure 6.

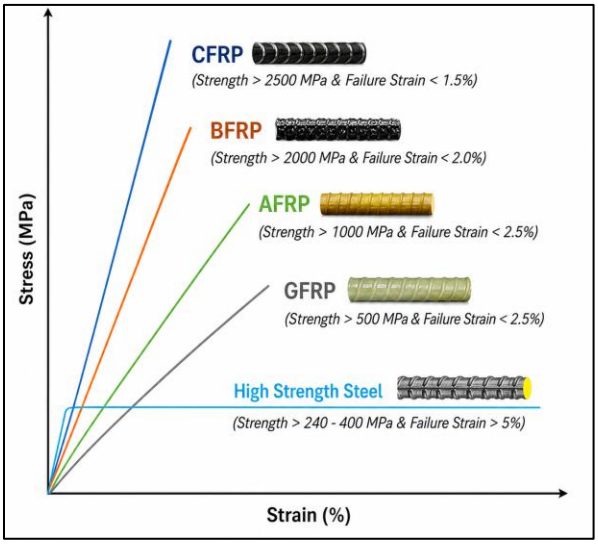

Figure 6: Comparison of Different FRP Materials and Mild Steel [70]

The mechanical behavior of FRP materials is primarily influenced by the type of reinforcing fiber, polymer matrix, fiber orientation, fiber volume fraction, and manufacturing process [67]. Common reinforcing fibers used in FRP systems include carbon fibers, glass fibers, aramid fibers, and basalt fibers [68]. Carbon fiber-reinforced polymers (CFRP) generally exhibit high stiffness, high tensile strength, and excellent fatigue resistance, whereas glass fiber-reinforced polymers (GFRP) provide lower material cost and good corrosion resistance [69]. The basic mechanical properties of FRP materials are presented in Table 1 [71].

Table 1: Fundamental Mechanical Properties of FRP Materials [72]

Property	CFRP	GFRP	AFRP	BFRP
Tensile Strength (MPa)	1650-3000	517-1207	1200-2068	1500-2400
Modulus of Elasticity (GPa)	152-165	41-55	50-74	90-130
Rate of Elongation (%)	1-1.5	3.5-5	2-2.6	1.2-1.6
Specific Gravity	1.5-1.6	1.5-2.0	1.25-1.4	1.9-2.1

The polymer matrix used in FRP materials may consist of either thermosetting or thermoplastic polymers. Thermosetting polymers, such as epoxy and polyester resins, undergo irreversible chemical curing and generally exhibit high stiffness and dimensional stability after hardening [67, 73]. In contrast, thermoplastic polymers soften upon heating and harden upon cooling without undergoing permanent chemical crosslinking. Thermoplastic FRP systems have recently gained increased attention due to their recyclability, rapid manufacturing capability, improved toughness, and enhanced impact resistance [73, 74]. Thermoplastic and thermoset polymers exhibit different thermal response mechanisms because of differences in their molecular structures. Thermoplastic polymers consist of linear or branched chains with weak intermolecular bonding, allowing the chains to move and soften when heated. As the temperature increases, thermoplastics can melt and be reshaped repeatedly. In contrast, thermoset polymers contain permanently crosslinked three-dimensional networks that restrict chain mobility. As a result, thermosets do not melt upon heating and instead undergo thermal degradation at elevated temperatures [75]. The schematic shown in Figure 7 describes this process.

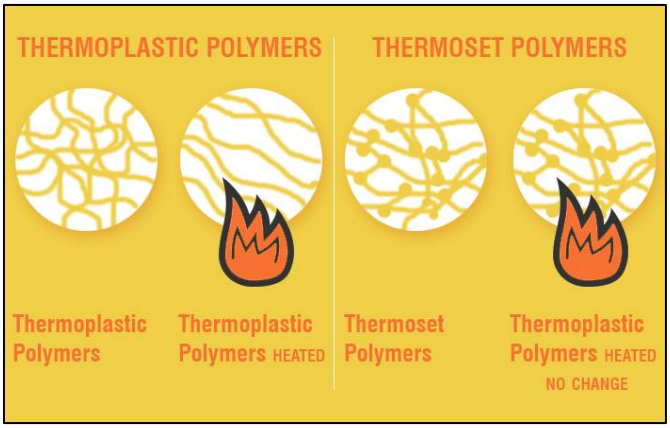

Figure 7: Comparison between Thermoplastics and Thermosets upon Heating [75]

FRP materials exhibit several advantageous characteristics compared to conventional steel reinforcement systems. Due to their low density, FRP materials significantly reduce additional dead load within structural systems while maintaining high tensile strength [68]. Furthermore, FRP materials are resistant to corrosion, moisture damage, and chemical attack, making them suitable for aggressive environmental conditions commonly encountered in bridge deck applications [76]. The noncorrosive nature of FRP systems is particularly beneficial in bridge environments exposed to deicing salts, moisture infiltration, and cyclic environmental loading.

The mechanical behavior of FRP materials is generally anisotropic, meaning that strength and stiffness vary depending on fiber orientation [67]. Consequently, load transfer efficiency and crack resistance may differ significantly based on reinforcement alignment within the structural system. In addition, some FRP systems may exhibit limited ductility and relatively brittle failure behavior compared to conventional metallic reinforcement materials [68]. Thermal sensitivity, interfacial bonding behavior, and compatibility with surrounding materials may also affect the long-term performance of FRP-reinforced overlay systems [73, 74].

2.7 Role of FRP membranes in the Interlayer

Interlayer systems have a critical influence on the bond quality between pavement layers, and it has been widely demonstrated that, regardless of the type of interlayer used, the interfacial bond governs the stress and strain distribution within composite pavement structures [10-14]. Consequently, the long-term performance of pavements, including their cracking behavior and deformation patterns, is strongly influenced by the condition and durability of the interlayer bond. Increased deflection, shear slippage, and premature deterioration under repeated traffic loading are often observed when the interface is weak, underscoring the need for reinforcement systems capable of enhancing composite action.

Glass fiber grids have gained particular attention due to their exceptional stiffness, tensile strength, and resistance to thermal and chemical degradation. Having a modulus of elasticity of approximately 70 GPa, nearly twenty times greater than that of asphalt concrete, glass fibers provide enhanced stress redistribution and improved resistance to crack initiation and propagation. The open-mesh configuration promotes aggregate interlock, facilitating efficient load transfer across layers and reducing shear potential at the interface [55].

When applied in conjunction with a tack coat, polymer-coated glass grids demonstrate superior tensile performance and bonding efficiency compared to uncoated or emulsion-coated alternatives [54]. Field and laboratory studies further report that interlayer systems installed on milled or roughened surfaces exhibit higher shear and tensile bond strength due to improved mechanical interlock and increased tack coat absorption [60]. These findings indicate that paving grids play an important role in keeping pavement layers bonded, improving interlayer shear strength, and increasing the overall service life of pavement systems. However, limited information is available regarding the bonding behavior of FRP membranes with common overlay materials.

This study aims to evaluate how effectively FRP membranes improve bonding between layers and enhance resistance to cracking in both asphalt and concrete overlays exposed to various environmental and loading conditions.

Previous studies on FRP-reinforced or FRP-strengthened concrete have generally demonstrated significant improvements in strength, ductility, confinement efficiency, and durability compared with unreinforced systems or steel-reinforced systems subjected to corrosion-prone environments. FRP confinement was reported to increase the compressive strength of concrete columns by approximately 20% to 120%, depending on the FRP type, confinement configuration, and concrete strength level [77]. In addition, flexural strengthening using CFRP and GFRP systems has commonly produced increases of 25% to 70% in load-carrying capacity and noticeable reductions in crack propagation and steel corrosion effects [68]. However, most available studies have focused on thermoset-based GFRP, CFRP, BFRP, and AFRP systems, while thermoplastic FRP applications in concrete have remained comparatively limited.

The primary advantage of thermoplastic FRP in concrete systems is its ability to combine structural reinforcement with enhanced damage tolerance and ductility. Because thermoplastic matrices can undergo greater deformation and energy absorption before failure, improvements in toughness and post-cracking behavior have been observed compared with brittle thermoset composites. Thermoplastic composite systems can exhibit impact energy absorption capacities approximately 30% to 50% greater than comparable thermoset composite systems because of improved matrix ductility and crack-arresting capability [78].

Chapter 03. Hypotheses, Objectives, and Goals

3.1 Hypotheses

In this study, the following hypotheses were tested:

i. Thermoplastic woven FRP systems incorporated within highly exothermic overlay materials are expected to improve interlayer bonding performance and interlayer shear strength compared to conventional overlay systems.

ii. Elevated temperatures generated during curing and placement of exothermic overlay materials may improve interaction between the thermoplastic systems and the surrounding overlay matrix, thereby improving interlayer stress transfer and bonding behavior.

iii. The incorporation of thermoplastic woven FRP systems is expected to improve mechanical interlocking and crack resistance within the interlayer region.

3.2 Objectives

The objectives of this study are listed below:

i. Evaluate how well the thermoplastic FRP membrane bonds to different exothermic overlay materials by performing mechanical tests.

ii. Measure and compare the interlayer shear strength (ISS) performance of overlay systems with and without thermoplastic woven FRP systems.

iii. Investigate the influence of polymer type, lattice geometry, and host material on interlayer stress transfer and failure behavior.

iv. Examine and relate the microscopic bonding features to the mechanical test results to identify the main factors that influence adhesion strength and long-term durability.

3.3 Goals

The following are the goals of this research:

i. Examine the potential of thermoplastic woven FRP systems to improve bonding performance through exothermic interactions and crosslinking behavior.

ii. Evaluate the feasibility of thermoplastic FRP-integrated overlays as durable bridge deck rehabilitation systems capable of improving interlayer performance and reducing premature de-bonding-related failures.

Chapter 04. Materials

This chapter discusses the experimental methodology and materials used in this study. It provides details on the testing matrix, the procedures adopted for incorporating FRP within the interlayer, the fabrication of asphalt specimens, the concrete mixing and casting processes, and the detailed descriptions of the testing setups and methods used.

4.1 Test Matrix

The experimental method in this study is divided into Part A and Part B. A total of 50 cylindrical specimens, each measuring 152.4 mm in diameter and 124 mm in height, were fabricated for Part A (pilot study). The pilot study was conducted to establish the experimental parameters and specimen configuration for Part B, which involved the fabrication of full-scale slab specimens measuring 12 in. × 16 in. × 4 in. from which core samples were extracted for testing. All the cylinder specimens followed the configuration illustrated in Figure 8.

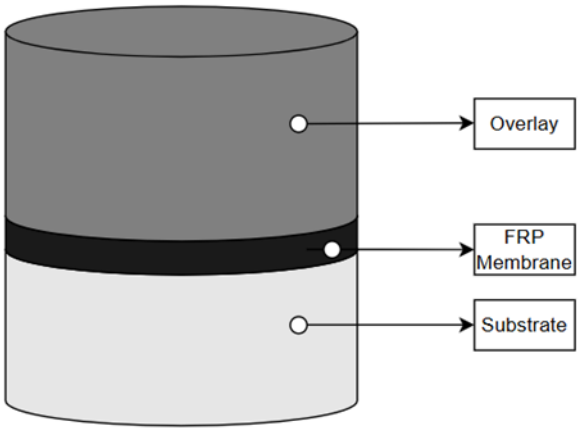

Figure 8: Schematic Representation of the Specimen Showing the Overlay, FRP Membrane, and Substrate Configuration

The pilot study evaluates three overlay-substrate combinations: asphalt-asphalt (A-A), portland cement concrete-portland cement concrete (PCC-PCC), and portland cement concrete-polymer

concrete (PCC-PC). For the A-A configuration, two specimen types were prepared: (i) specimens incorporating only the polymer tape, and (ii) specimens incorporating the polymer tape in combination with a tack coat. Four polymer tapes were evaluated: C-PA6, C-PA410, G-PP, and G-PETG, where C denotes carbon fiber reinforcement and G denotes glass fiber reinforcement. PA6 (polyamide 6), PA410 (polyamide 410), PP (polypropylene), and PETG (glycol-modified polyethylene terephthalate) refer to the thermoplastic polymer matrices used in the composite tapes. In addition, for the A-A configuration, 12 supplementary cases using G-HDPE polymer tapes were prepared and tested to further assess interlayer performance. Table 2 summarizes the test matrix for the pilot study. Control specimens were included for comparison. For the A-A configuration, two control cases were prepared: one without tack coat and one with tack coat. For the PCC-PCC and PCC-PC configuration, one control case without any polymer tape was prepared. Table 3 summarizes the additional G-HDPE cases for the A-A specimens.

Table 2: Test Matrix of Pilot Study

Interface Type	Control Case	With Tack Coat & Polymer Tape	Polymer Tape Only	Additional G-HDPE Cases	Total Specimens
Asphalt-Asphalt	4	16	8	12	40
PCC-PCC	2	-	6	-	-
PCC-PC	2	-	8	-	10
Total	6	16	16	12	50

Table 3: Additional G-HDPE Cases

Case	Total Specimens
Heated Tape	2
Surface Preparation	2
HDPE Tape Only	2
With Tack Coat (Inclined Angle)	2
With Tack Coat (Parallel Orientation)	2
With Tack Coat (Perpendicular Orientation)	2

Based on the performance observed in the initial study, two tapes were selected for further evaluation. In this phase, the polymer lattice of the chosen tape was placed as an interlayer membrane within the slabs. Four core samples were extracted from each slab and tested using the Louisiana Interlayer Shear Strength Test (LISST) to evaluate interfacial bonding performance and shear resistance. Figure 9 illustrates the experimental matrix used in the study in the form of a flowchart.

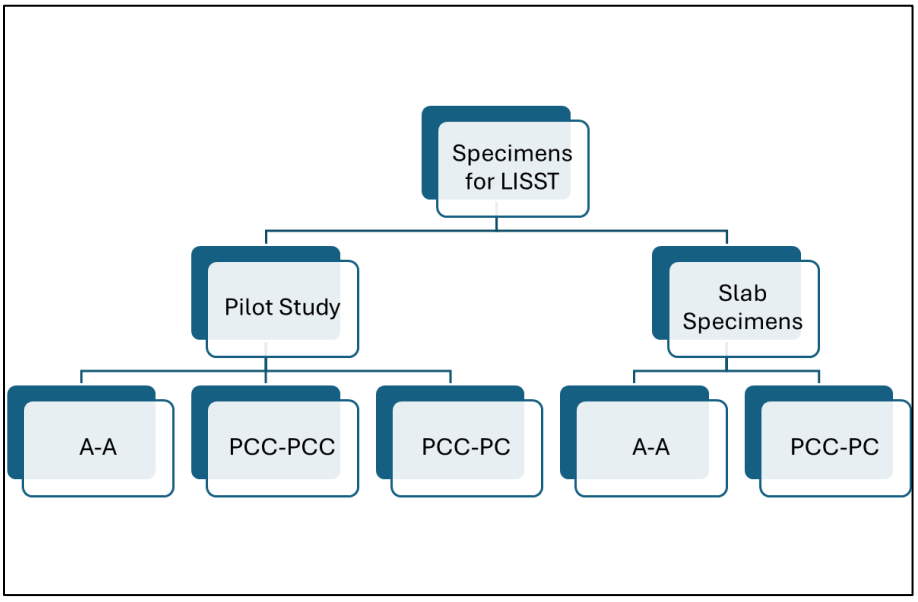

Figure 9: Experimental Matrix for LISST Specimens

Two types of thermoplastic FRP lattice systems, C-PETG and G-HDPE, were evaluated in Part B of this study. Two different lattice opening sizes, namely 1 in. × 1 in. and 1 in. × 0.5 in., were investigated for each FRP type. One slab specimen was prepared for each lattice configuration, resulting in a total of four slab specimens for the asphalt-asphalt (A-A) system, along with one control slab containing only tack coat. In addition, four slab specimens were prepared for the portland cement concrete-polymer concrete (PCC-PC) system.

4.2 Asphalt Mix

For the pilot study, an asphalt mix was collected from a local asphalt plant and material suppliers. The tack coat used was Polymer Modified Cationic Rapid Set 1s (PMCRS 1s) and was collected from a local material supplier.

The identification and selection of the materials and their suppliers were carried out in close cooperation with the ODOT Materials Division. A dense-graded surface course (S4) asphalt mix without any recycled material was collected from Tulsa Asphalt Co., Tulsa, Oklahoma. The mix ID for the collected mix was S4pv0262100600. Figure 10 shows photographic views of the material collection efforts.

Figure 10: Collection of Asphalt Mix from Plant

The collected mix consisted of 5.4% of PG 70-28 asphalt binder. The details of aggregate types and sources used in this mix are given in Table 4. The gradation curve of combined aggregates is presented in Figure 11.

Table 4: Aggregate Type and Source for the Collected Asphalt Mix

Bin No	Aggregate	Producer/ Supplier	% by weight
1	#67 Rock	Anchor Stone (Owasso, OK) P/S # m001156603	9
2	¾" Chips	Anchor Stone (Owasso, OK) P/S # m001156603	11
3	Mine Chat	Mine Chat @Tri City Area P/S # Mine Chat	25
4	Man. Sand	Anchor Stone (Owasso, OK) P/S # m001156603	17
5	Scrns.	Anchor Stone (Owasso, OK) P/S # m001156603	22
6	Sand	Anchor Sand, Delaware Ave. (Jenks, OK) P/S # m001137217	15
7	B. H. Fines	Contractor / Project Site P/S # Contractor	1

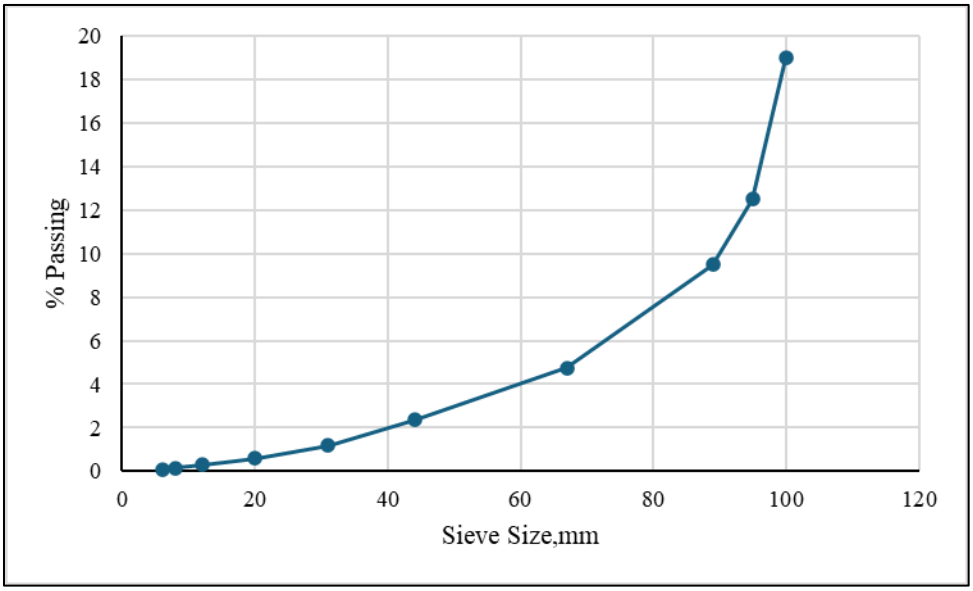

Figure 11: Aggregate Gradation Curve of the Asphalt Mix

For the fabrication of asphalt slabs, a dense-graded surface course (S4) asphalt mix without any recycled material was collected from Haskell Lemon Construction Co. The collected mix consisted of 4.9% of PG 64-22 asphalt binder. The details of aggregate types and sources used in this mix are given in Table 6. The gradation curve of combined aggregates is presented in Figure 12. The mix ID for the collected mix was S4qc0132401200.

Table 5: Aggregate Type and Source for the Collected Asphalt Mix

Bin No	Aggregate	Producer/ Supplier	% by weight
1	5/8” chips	Heidelberg Materials (Hanson Davis Quarry) P/S # m001985008	35
2	C-33 scrns	Martin-Marietta Mill Creek Granite P/S # m002303502	23
3	scrns	Dolese Co (Davis, OK) P/S # m002745002	30
4	Sand	General Materials	12

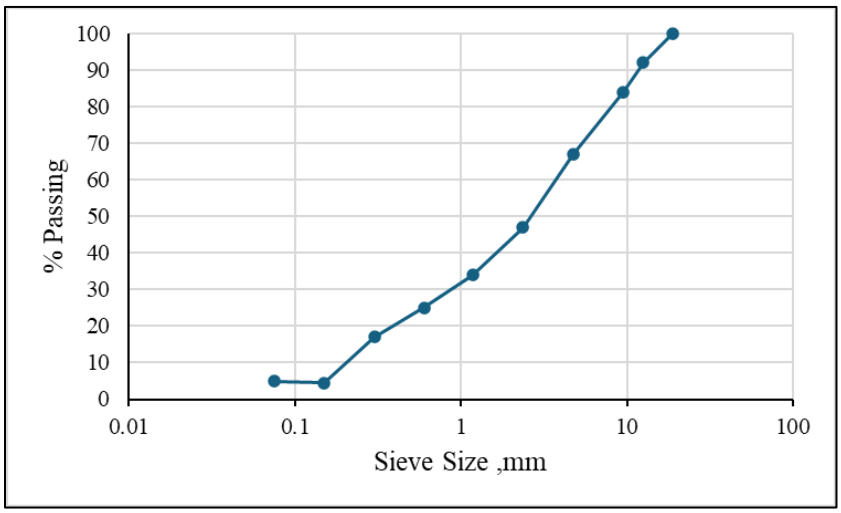

Figure 12: Aggregate Gradation Curve of the Asphalt Mix

4.3 Portland Cement Concrete Mix without Coarse Aggregate

Type I/II portland cement, water, fine aggregate, and a superplasticizer were used in the portland cement concrete (PCC) mixture prepared for the pilot study. The materials were mixed in the proportions stated in Table 6 with a water-to-cement ratio of 0.3. MasterGlenium 7920 superplasticizer was used in this study, 738 cc per 100 kg, which is within the recommended dosage of 130 cc to 780 cc per 100 kg for cementitious materials. The nominal maximum size of the fine aggregate used in this mix is 2.36 mm. The well-graded fine aggregate was selected for the specimen's small size. Figure 13 shows the size distribution of the fine aggregate for Portland cement concrete.

Table 6: PCC Material Mix Design

Material	Units	Amount
Superplasticizer		5.8
Water	$\frac{kg}{m^3}$	141.1
Portland Cement		455.3
Aggregate		910.6

The well-graded fine aggregate was selected for the specimen's small size. Figure 13 shows the size distribution of the fine aggregate for Portland cement concrete.

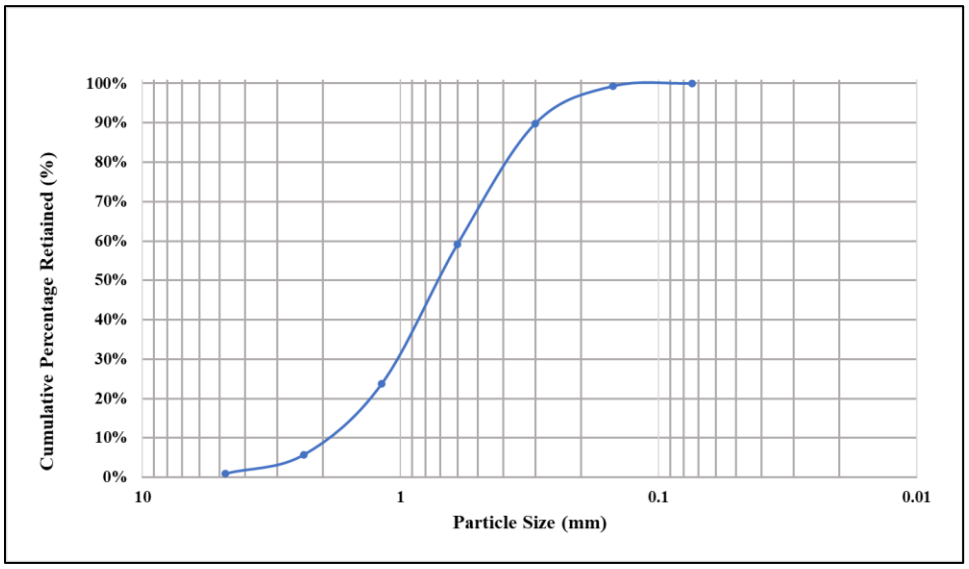

Figure 13: Fine aggregate for Portland cement concrete specimen

4.4 Portland Cement Concrete Mix with Coarse Aggregate

Specimens were prepared using a Portland cement concrete (PCC) substrate and a polymer concrete (PC) overlay to simulate a concrete bridge deck with a polymer concrete overlay. The ODOT Class AA mix design used to prepare the PCC substrate is presented in Table 10. The coarse aggregate conformed to ODOT No. 67 gradation, with a nominal maximum aggregate size of 25 mm (1 in.). The gradation curve of the sand used in this study is presented in Figure 14. MasterGlenium 7920 was used as a high-range water-reducing admixture).

Table 7: Mix Design of PCC substrate

Material	Quantity	Unit
Cement	349	Kg/m^3
Coarse Aggregate (Rock)	1085.6	Kg/m^3
Fine Aggregate (Sand)	759	Kg/m^3
Water	153	Kg/m^3
High Range Water Reducer	874	mL/m^3
Air Entraining Agent	341	mL/m^3

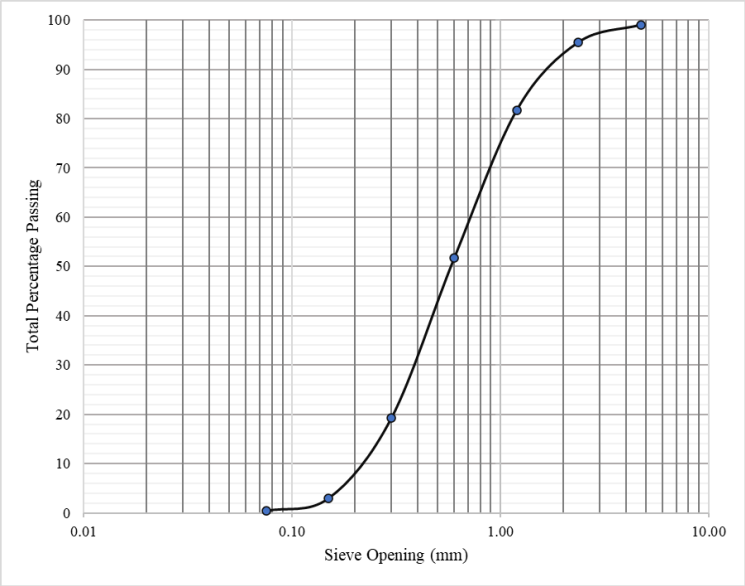

Figure 14: Gradation Curve of Fine Aggregate for Portland Cement Concrete Specimen

4.5 Polymer Concrete Mix

The polymer concrete mix used in this study was obtained from Transpo Industries and consisted of the commercially available T-17 Polymer Concrete. The material is a prepackaged methyl methacrylate (MMA)-based polymer concrete mixture. The mix design used for the polymer concrete overlays is presented in Table 11.

Table 8: Mix Design for Polymer Concrete

Material	Units	Amount
Powder	$\frac{kg}{m^3}$	2063.6
Liquid		199.5

4.6 Polymer Tapes

Five types of polymer tapes were used in this study. Their chemical composition and characteristics are discussed below:

4.6.1 Polyamide 6 (C-PA6)

Polyamide 6 (C-PA6) is classified as a high-performance thermoplastic composite in which the excellent toughness, abrasion resistance, and thermal stability of polyamide 6 (nylon 6) are combined with the superior stiffness and strength of carbon fibers (Oribi Composites, n.d.). Polyamide 6 (PA6) is synthesized through the ring-opening polymerization of caprolactam [79].

4.6.2 Polyamide 410 (C-PA410)

Polyamide 410 is classified as a high-performance, aliphatic, bio-based polyamide in which the advantages of both short-chain and long-chain polyamides, including low moisture absorption and excellent mechanical performance, are combined [80]. This polyamide is derived from 1,4-diaminobutane and sebacic acid [81].

4.6.3 Polyethylene Terephthalate Glycol (G-PETG)

Polyethylene Terephthalate Glycol (PETG) is classified as a glycol-modified form of Polyethylene Terephthalate (PET). PETG is produced through the copolymerization of polyethylene terephthalate with cyclohexane dimethanol, resulting in the chemical composition $(C_{10}H_8O_4)_x \times (C_{10}H_{14}O_4)_y \times (C_2H_6O_2)_z$, where x, y, and z represent the mole fractions of terephthalic acid, cyclohexane dimethanol, and ethylene glycol, respectively [82]. Resistance to wear and impact is significantly improved through the incorporation of glass fibers [83].

4.6.4 Polypropylene (G-PP)

Polypropylene (G-PP) is classified as a lightweight thermoplastic composite that is widely used in structural and infrastructure applications due to its favorable balance of mechanical strength, chemical resistance, and cost efficiency. Polypropylene is synthesized from propylene monomers with the chemical repeat unit $(C_3H_6)_n$. It is classified as a semi-crystalline polymer that is known for its low density, high fatigue resistance, and excellent resistance to acids, bases, and moisture [84].

4.6.5 Polyethylene (G-HDPE)

High-density polyethylene (HDPE) is classified as a nonpolar, highly crystalline thermoplastic resin that exhibits good mechanical strength and excellent chemical resistance [85]. Its chemical formula is expressed as $(C_2H_4)_n$. When compared to other polyethylene types, a relatively low degree of chain branching is exhibited by high-density polyethylene. When HDPE is reinforced with glass fibers, significantly improved tensile strength, elastic modulus, and dimensional stability under mechanical loading are achieved [86].

The general molecular structure of the tapes has been shown in Table 8. The micro and macrostructure are presented in Figure 15.

Table 9: Chemical Structure and Glass Transition Temperature (T_g) of Thermoplastic Tapes

Types of Polymer	Chemical Structure	Glass Transition Temperature T_g	Source
Polyamide 6 (PA6)	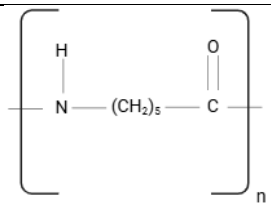	29.0°C to 60.0°C	[79]
Polyamide 410 (PA410)	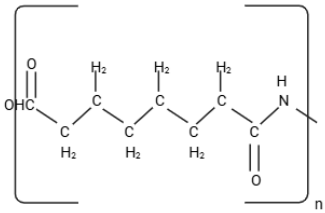	70°C	[80]
Polyethylene terephthalate glycol (PETG)	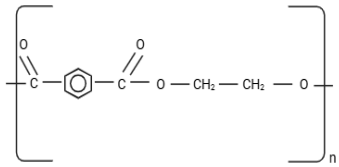	80°C to 82°C	[87]
Polypropylene (PP)	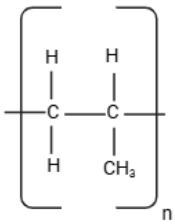	-20°C to -10°C	[88]
High-density polyethylene (HDPE)	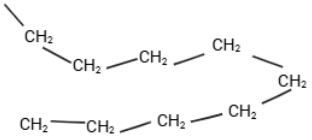	-100°C to -130°C	[89]

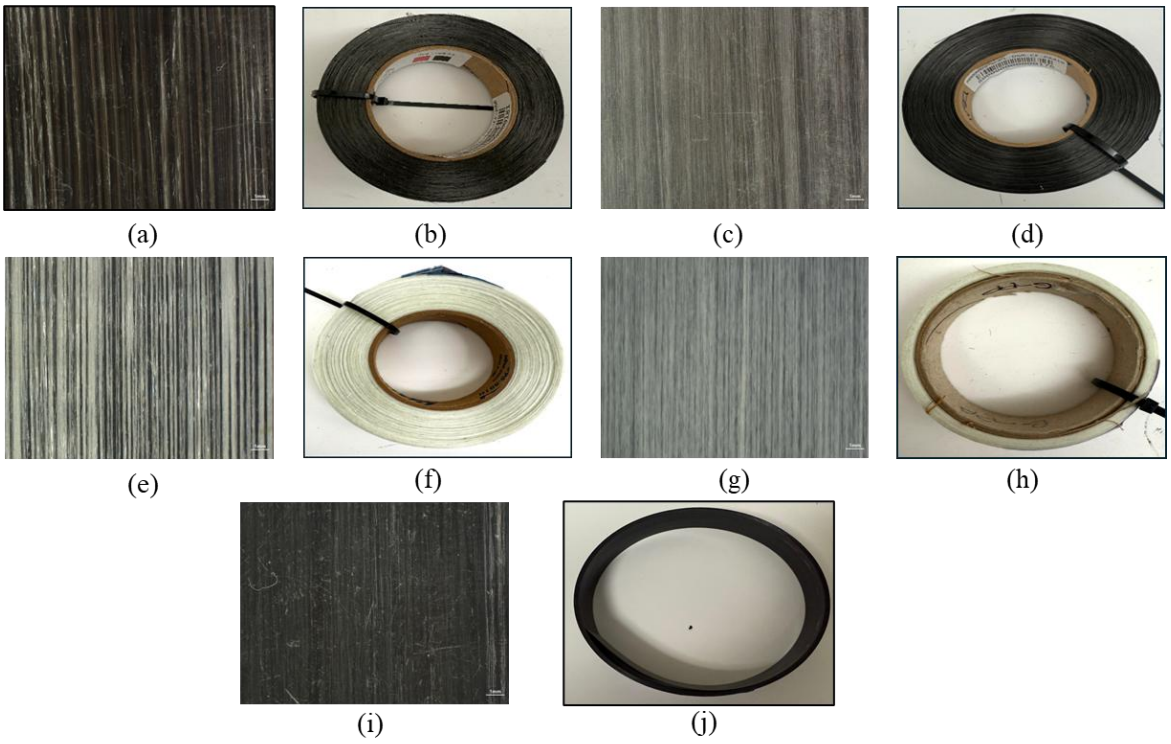

Figure 15: Micro and Macrostructure Images of FRP Tapes- (a-b) C-PA6, (c-d) C-PA410, (e-f) G-PETG, (g-h) G-PP, and (i-j) G-HDPE

4.7 Polymer Lattice

Woven lattice structures made of unidirectional glass fiber-reinforced HDPE (G-HDPE) and carbon fiber-reinforced PETG (C-PETG) were provided by Weav3D for further investigation. The lattices were fabricated using thermoplastic prepreg tapes with a nominal width of 1 inch, arranged in an orthogonal weaving configuration. Thermoplastic FRP systems offer several manufacturing and processing advantages compared with conventional thermoset composites because consolidation is achieved primarily through heating and cooling cycles rather than irreversible curing reactions. During fabrication, continuous fibers are impregnated with thermoplastic resin to produce prepreg tapes, which are subsequently arranged into engineered woven or lattice-type reinforcement geometries. The thermoplastic material is then subjected to

elevated temperatures during molding and consolidation processes, allowing the polymer matrix to soften and promote thermal bonding and mechanical interlocking within the composite structure. After consolidation, the material is cooled under controlled conditions to achieve dimensional stability and structural integrity [90]. This process is described below in Figure 16.

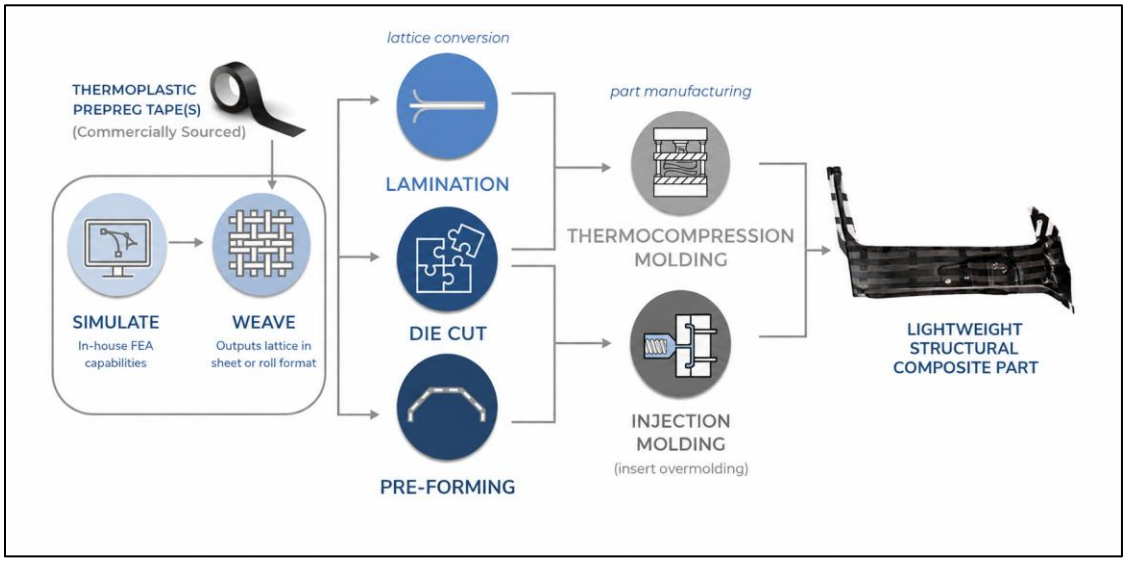

Figure 16: Process of Manufacturing Polymer Lattice [90]

The resulting lattice geometry consisted of regularly spaced square openings measuring 1 in. × 1 in., along with rectangular openings measuring 1 in. × 0.5 in. formed through the alternating tape arrangement. The C-PETG lattice was manufactured with an overall width of 28 inches, whereas the G-HDPE lattice was fabricated with a total width of 16 inches. The uniform tape width and repeating opening geometry ensured consistent spacing and alignment throughout each lattice system. Figure 17 shows the lattices used in this study.

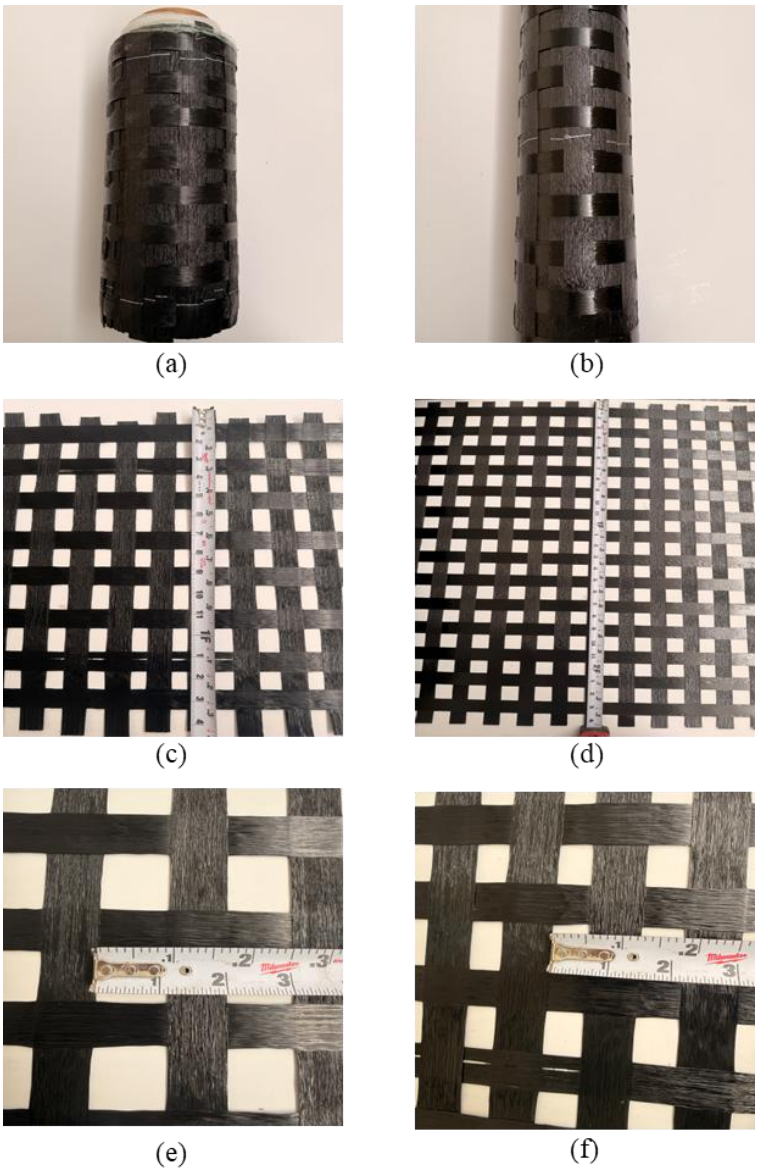

Figure 17: Woven FRP Lattice (a) Rolled G-HDPE, (b) Rolled C-PETG, (c) Overall Width of G-HDPE, (d) Overall Width of C-PETG, (e) Opening Size of 1 in. × 1 in., (f) Opening Size of 1 in. × 0.5 in.

Chapter 05. Methods

5.1 Part A: Preparation of Pilot Study Specimens

5.1.1 Asphalt-Asphalt (A-A) Pilot Study Specimens

Cylindrical specimens were fabricated with a diameter of 152.4 mm and a height of 124mm, comprising two asphalt layers. The bottom layer was compacted to a height of 62 mm and a target air void content of 7 ± 0.5% using a Superpave Gyratory Compactor (SGC). Some preliminary laboratory tests were conducted before specimen preparation, which is described below.

5.1.1.1 Theoretical Maximum Specific Gravity (G_{mm}) Test

The Rice test of asphalt, also known as the Theoretical Maximum Specific Gravity (G_{mm}) test, was used to determine the maximum specific gravity of the asphalt mixture without air voids according to AASHTO T 209 [91].

Approximately 2500 g of loose asphalt mixture was first dried to a constant mass at a temperature of 105 ± 5°C and then allowed to cool to room temperature. The cooled sample was placed directly into a 10,000 mL vacuum container. The mass of the sample and container was measured, and the mass of the empty container was subtracted to determine the net dry mass of the sample, recorded as (A).

Sufficient water at a temperature of approximately 25°C (77°F) was added to completely cover the sample. Entrapped air was removed by gradually applying a vacuum until a residual pressure of 3.7 ± 0.3 kPa (27.5 ± 2.5 mmHg) was reached. This pressure was maintained for 15 ± 2 minutes while continuously agitating the container and its contents using a mechanical agitation device. For glass containers, agitation was performed on a resilient rubber or plastic surface to

avoid excessive impact during vacuuming. At the end of the vacuum period, the vacuum was released at a rate not exceeding 8 kPa (60 mmHg) per second.

The theoretical maximum specific gravity was calculated at 25°C (77°F) using:

$$G_{mm} = \frac{A}{A + B - C} \quad [2]$$

Where,

A = mass of the oven-dry sample in air,

B = mass of the container filled with water, and

C = mass of the container filled with the sample and water.

The procedure was repeated three times, and the average G_{mm} value was determined to be 2.414. Photographs from the experimental procedure are shown below in Figure 18.

Figure 18: Vacuuming process during the G_{mm} test

5.1.1.2 Bulk Specific Gravity of Compacted Hot Mix Asphalt

Using the G_{mm} value, the required dry weight was determined to be 2415 g to produce specimens with a target air void content of 7% ± 0.5%. Additional G_{mb} tests confirmed this finding following AASHTO T 166 [92].

The specimen was allowed to cool at room temperature for 24 hours. The asphalt specimen was then immersed in water at 25 ± 1°C for 4 ± 1 minutes, and the immersed mass was recorded as C. The specimen was removed from the water and quickly surface dried using a damp towel to remove excess surface moisture. The process is shown in Figure 19. The saturated surface-dry (SSD) mass of the specimen was then recorded as B. The bulk specific gravity was calculated using the following formula:

$$Bulk\ Specific\ Gravity = \frac{A}{B - C} \quad [3]$$

Where,

A = Mass in grams of specimen in air

B = Mass in grams of surface dry specimen in air, and

C = Mass in grams of specimen in water

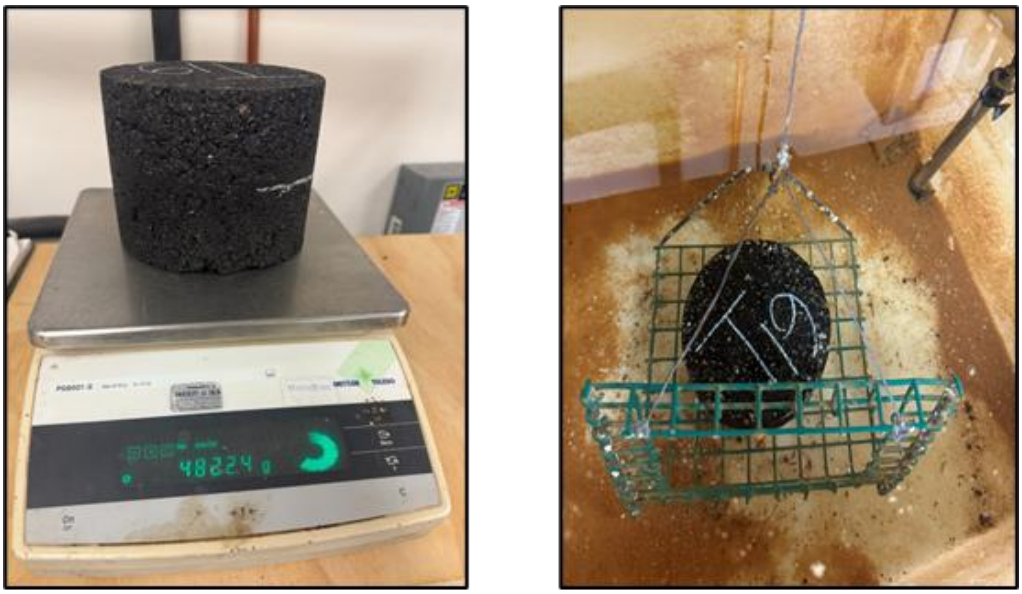

Figure 19: (a) Taking the Weight of Specimen in Air, (b) Taking the Weight of Specimen in Water

Afterwards, the percent of air voids was calculated using the following equation in accordance with AASHTO T 269 [93]:

$$Va = \left(1 - \frac{G_{mb}}{G_{mm}}\right) * 100 \quad [4]$$

An air void content of 6.8% was obtained, which falls within the acceptable range.

5.1.1.3 Residue of Emulsified Asphalt

Asphaltic residue of tack coats was measured according to the procedure 'A' specified in the ASTM D 6834 "Standard Test Method for Residue by Evaporation of Emulsified Asphalt" [94]. The residue content of the asphalt emulsion was determined using three replicate samples. The mass of each beaker containing a glass rod was first measured to the nearest 0.1 g. Then, 50 ± 0.1 g of thoroughly mixed asphalt emulsion was poured into each beaker. The beakers containing the glass rods and emulsion samples were placed in an oven at 163 ± 3°C for 2 hours. After this period,

each beaker was removed, and the residue was thoroughly stirred using the glass rod. The beakers were then returned to the oven for an additional 1 hour. After heating, the beakers were removed from the oven, allowed to cool to ambient temperature, and weighed with the glass rods to determine the remaining residue mass. The percentage of residue on each beaker was calculated using the following equation:

$$residue, \% = 2 \times (A - B) \quad [5]$$

Where,

A = mass of beaker, rod, and residue, g, and

B = tare of beaker and rod, g.

The average of the three test results was used to determine the residue percentage of the tack coat, which was found to be 61.2 %. The calculation procedure is presented below in Figure 20. The residual application rate of 0.2 gal/yd² was selected from Table 407:1 for the surface type "new fabric" in the Oklahoma Department of Transportation (ODOT) 2019 Standard Specifications for Highway Construction [95].

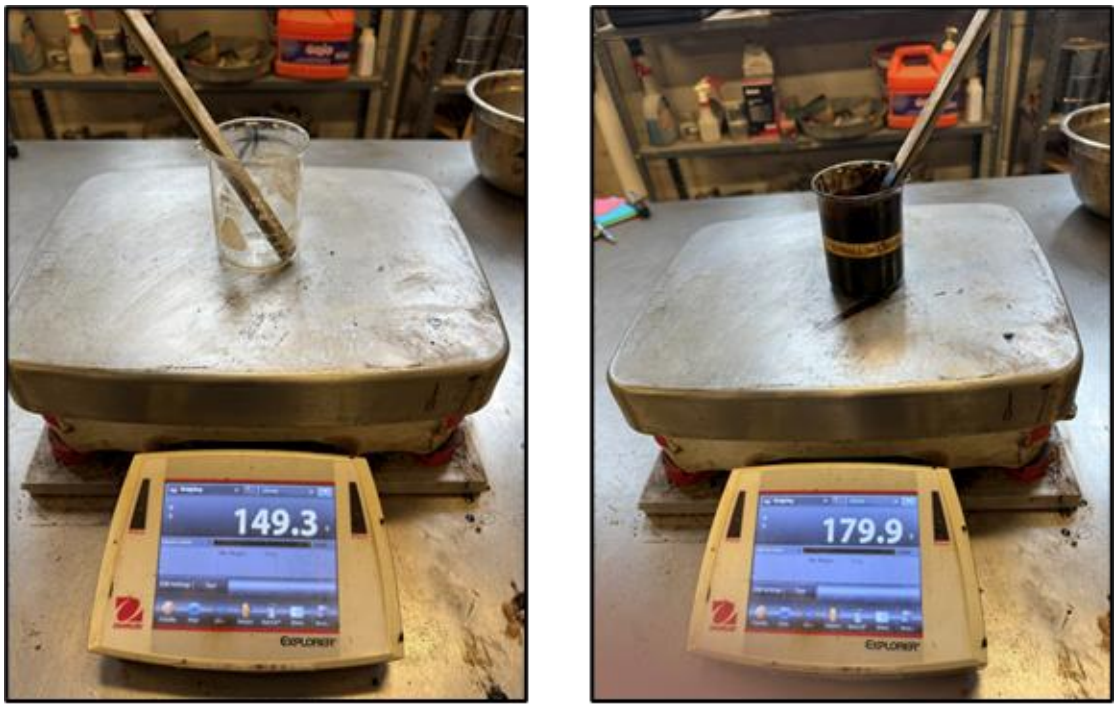

Figure 20: (a) Weight of Beaker and Rod, and (b) Weight of Beaker, Rod, and Residue

5.1.1.4 Fabrication of Pilot Study A-A Specimens

At first, the asphalt mixture was heated in an oven at 149°C for 2 hours. To slide the bottom layer easily inside the mold to compact with the top layer, the bottom layer was molded to a slightly smaller diameter than the internal diameter of the SGC mold. This was achieved by inserting custom paperboard strips along the inner wall of the mold during bottom-layer compaction, as shown in Figure 21.

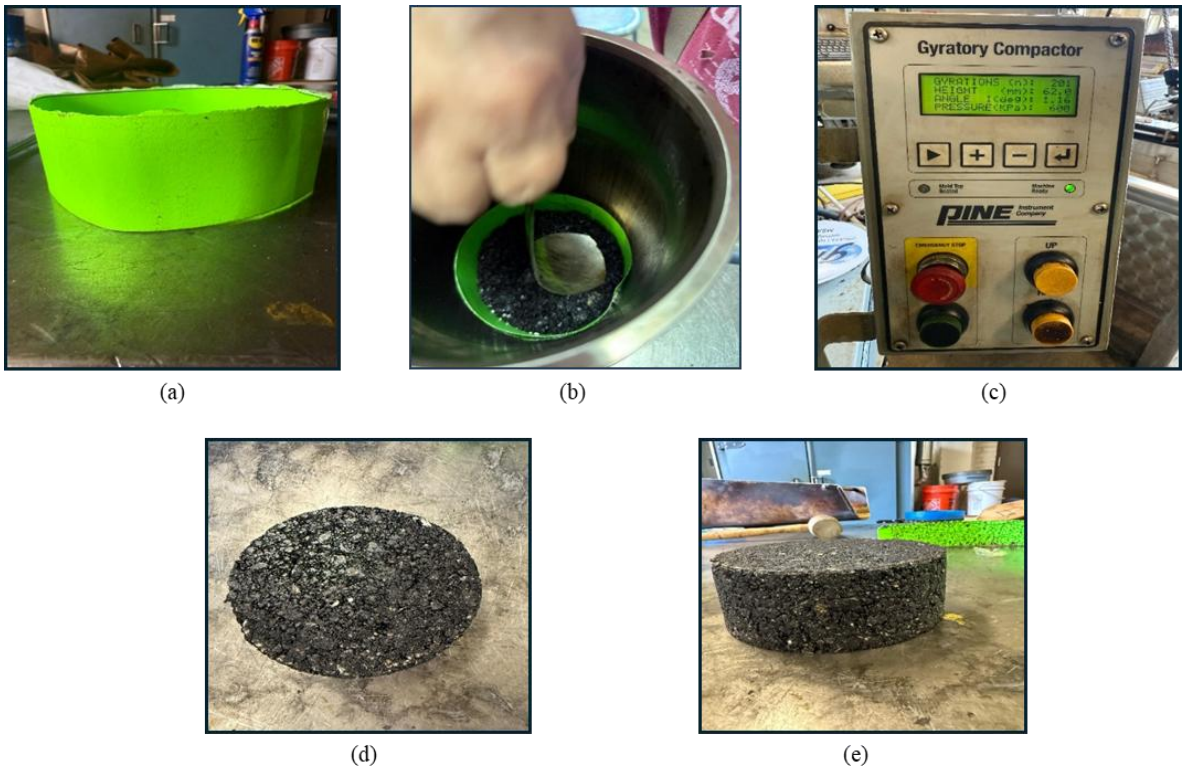

Figure 21: Preparation of the Bottom Layer Specimen for Composite Asphalt Sample Fabrication, (a) Paperboard Strip Used to Reduce the Internal Diameter of the SGC Mold, (b) Placement of Paperboard Liner Inside the Mold and Tamping to Compact a Slightly Smaller Bottom Layer Specimen, (c) Gyratory Compactor Settings Used During Compaction: 201 Gyrations, 62.0 mm Height, 1.16° Angle, and 600 kPa Pressure, (d) Top-View of the Compacted Bottom Layer, (e) Compacted Bottom Layer Specimen after Removal from the Mold

Two types of interlayer configurations were prepared:

i. FRP only, and

ii. FRP + Tack Coat.

After a 24-hour cooling period, different interlayer configurations were prepared by selectively treating the surface of the bottom layer. The bottom surface was marked to identify the fiber orientation. Two strips of polymer tape were placed in each specimen. The strips were positioned along the specimen diameter, with each strip located 1.5 in. from the specimen edge, as shown in the schematic in Figure 22.

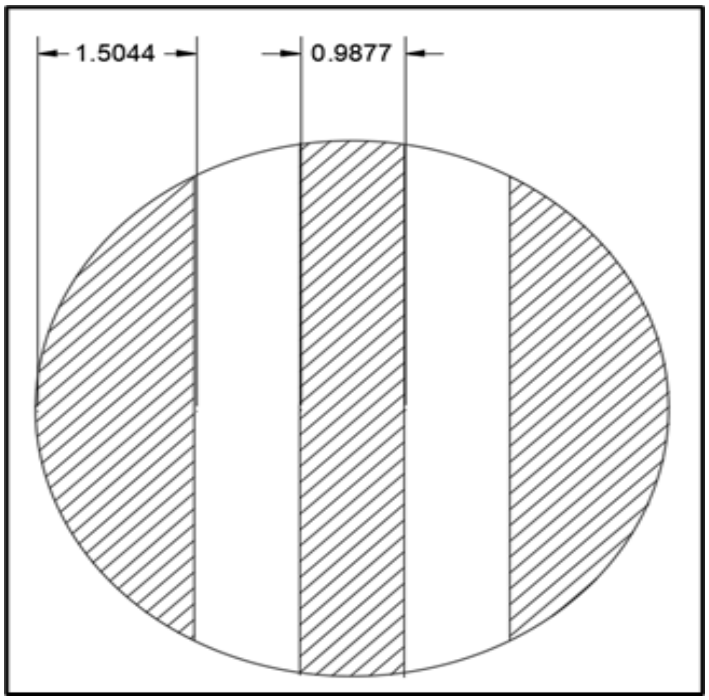

Figure 22: Schematic arrangement of FRP strips at the interlayer

For specimens incorporating a tack coat, the tack coat was applied at a residual application rate of 0.20 gal/yd², while for specimens without FRP and containing only tack coat, a residual application rate of 0.035 gal/yd² was used, both in accordance with the guidelines of the Oklahoma Department of Transportation 2019 Standard Specifications for Highway Construction [95] . The top layer was compacted to a thickness of 62 mm with a target air void content of 7 ± 0.5%. This process is shown in Figure 23. For the additional HDPE cases subjected to thermal treatment, the GHDPE tapes were locally heated prior to placement using a heat gun. The tapes were heated to approximately their glass transition temperature to soften the material and promote adhesion at the interface.

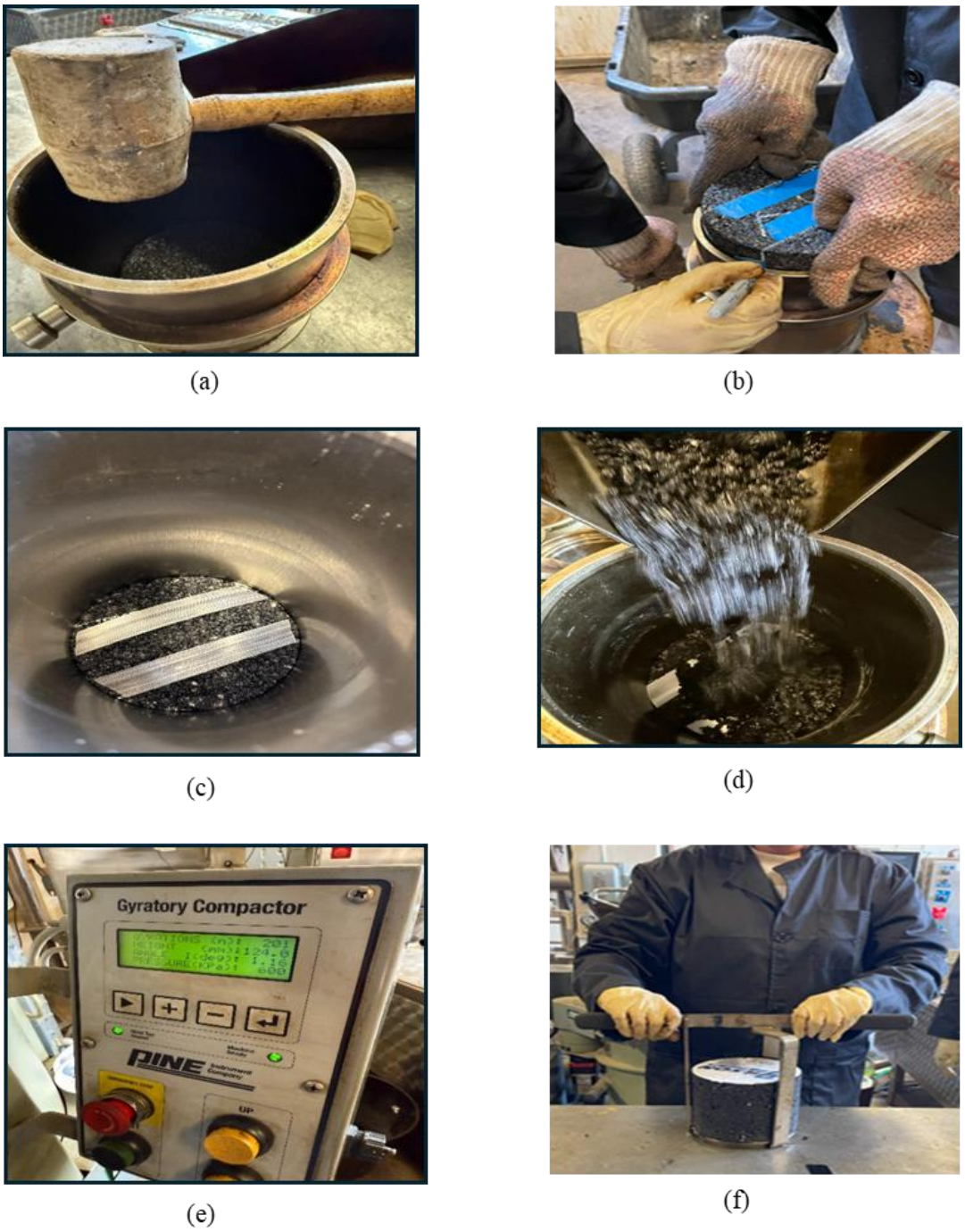

Figure 23: Preparation and Testing Process for Polymer-Reinforced Asphalt Specimens, (a) Placement of the Compacted Bottom Layer into the SGC Mold Using a Rubber Mallet, (b) Marks were Made on the Bottom Surface of the Specimen and the Mold, (c) Alignment of FRP Tapes on the Surface of the Compacted Bottom Layer before Pouring the Top Layer, (d) Pouring Hot Asphalt Mix to Form the Top Layer over the FRP-Reinforced Bottom Layer, (e) Gyratory Compactor Control Panel Displaying Compaction Settings for the Top Layer, (f) Completed a Double-Layer Asphalt Specimen after Compaction

Following compaction, the composite specimen was allowed to cool overnight before testing in the LISST device. A shear rate of 2.54 mm/min was used to conduct the test as per TP 114 [96] . This procedure was repeated for each asphalt overlay material. Inclined, parallel, and perpendicular fiber orientations relative to the shear plane were investigated (Figure 24) to examine the influence of fiber alignment on interfacial shear performance. However, not all composite systems were evaluated under each orientation.

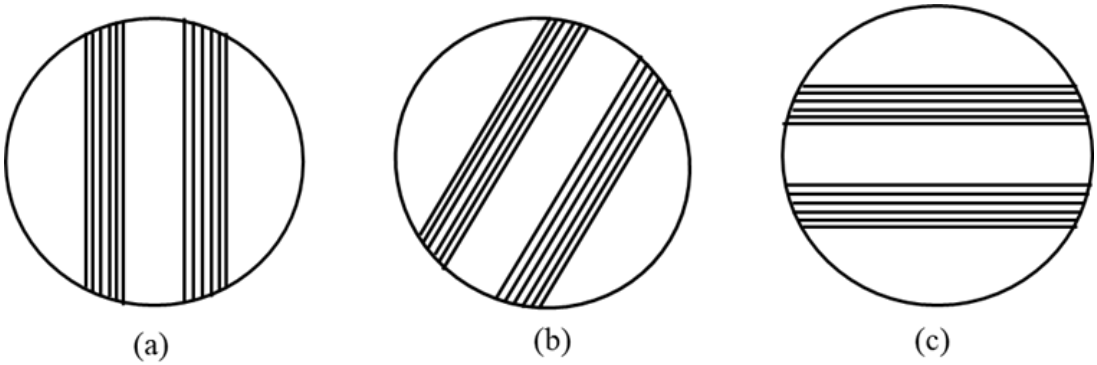

Figure 24: Illustration of the fiber orientations tested using the LISST apparatus with respect to the shear plane: (a) Parallel, (b) Inclined, and (c) Perpendicular

5.1.2 PCC-PCC Pilot Study Specimens

The superplasticizer was added to the water and mixed well before the casting process. Dry materials were placed in the mixer and then mixed to improve the material distribution. The water and superplasticizer mix were then added incrementally, and the mixture was continued for 3-5 minutes. Afterwards, the mix was poured into the plastic cylindrical molds. Each layer was made 62 ± 5 mm in height and 152.4 mm in diameter. The concrete was cast following the ASTM C192 [97]. Procedure. The specimens were vibrated using a concrete vibratory shaker table to achieve adequate compaction and minimize air voids. The mixing and casting procedure is shown in Figure 25.

(a) (b)

Figure 25: (a) Mixing the materials in the mixer (b) Shaking in a Concrete Vibratory Shaker Table

After 24 hours, the substrate layer was demolded and cured for 14 days. The cured substrates were then surface prepared using a surface grinder in accordance with ICRI guidelines to achieve a Concrete Surface Profile (CSP) of 5-9. The procedure is described in Figure 26.

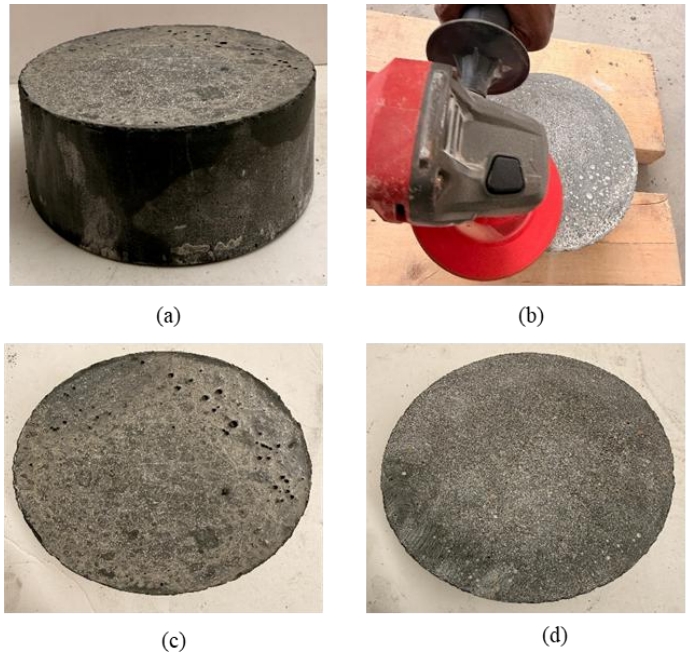

(a) (b)

(c) (d)

Figure 26: (a) Demolded substrate, (b) Grinding with a surface grinder, (c) Surface before grinding, (d) Surface after grinding

Two strips of FRP tape were placed at the interface in a configuration similar to that used for the A–A specimens. The concrete mixture was prepared according to the substrate mixing procedure

and was subsequently placed over the FRP strips. Following a curing period of 7 days, the specimens were removed from the curing and tested.

5.1.3 PCC-PC Pilot Study Specimens

For the pilot study specimens containing coarse aggregate, a standard ODOT Class AA concrete mixture was used. To prepare the mixture, the air-entraining agent was first added to the fine aggregate in a mixing bucket. Then, the fine and coarse aggregates were added to the mixer and mixed for 1 minute. The total mixing water was divided into two equal parts. One-half of the high-range water reducer (HRWR) was added to one portion of the water, while the remaining half was added directly into the mixer. The water containing the HRWR was then introduced into the mixer with the aggregates and mixed for 1 minute. Afterwards, cement was added, followed by the remaining water without HRWR and the remaining portion of the HRWR. The mixture was then mixed until a consistent and uniform consistency was achieved. After mixing, air content and slump tests were conducted. An air entrainment of 3.4% and a slump of 2.75 in. were obtained, as shown in Figure 27 (a) and (b), respectively.

(a) (b)

Figure 27: (a) Air Entrainment Test, and(b) Slump Test

The fresh mixture was subsequently cast into standard cylindrical molds with a diameter of 6 in. and cube molds measuring 2 in. × 2 in. × 2 in. in accordance with ASTM C192 [97]. Some parts of the mixing procedure are shown in Figure 28.

(a) (b) (c)

Figure 28: (a) All Materials before Mixing, (b) Mixing Air Entraining Agent with Fine Aggregate, and (c) Compaction using a Vibrating Table

The specimens were cured for 7 days, after which compressive strength tests were carried out. Following curing, the surface was ground using a surface grinder to ensure proper interface conditions, in accordance with the guidelines of the ICRI, similar to the procedure described previously and shown in Figure 14. Afterwards, two strands of FRP strips were then placed at the interface, and polymer concrete was cast on top. The composite was mixed for 3 minutes using a mechanical drill with a mixing paddle and a bucket until a homogenous mixture was obtained. Since polymer concrete is a rapid-setting material, the concrete specimens were cast within 3-5 minutes to avoid material hardening. The casted overlays were cured for 24 hours before demolding them and 7-day curing in room conditions before testing. This procedure is shown below in Figure 29.

(a) (b) (c)

Figure 29: (a) Placement of Strips on the Prepared Substrate Surface, (B) Mixing of Polymer Concrete Using a Paddle, and (C) Polymer Concrete Placed on the Shaker Table.

The 6 in. specimens were cored to 3.75 in. using a core drill, as shown in Figure 30. This was performed to comply with the testing capacity limitations of the LISST equipment, which is designed for testing 4 in. specimens. The remaining gap was filled with Hydrostone, and the specimens were allowed to cure for 24 hours before testing.

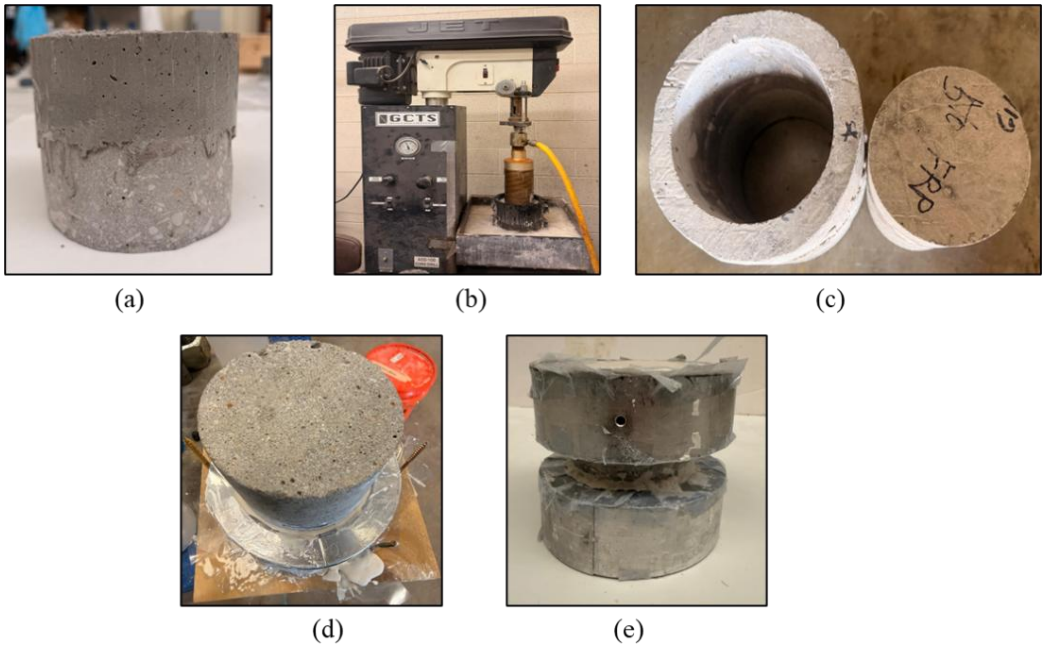

(a) (b) (c)

(d) (e)

Figure 30: (a) Finished Specimen of PCC Substrate and PC Overlay, (b) Coring of 6 in. Specimen, (c) Cored Specimen, (d) Pouring Hydrostone to Fill the Gap, and (e) Finished Specimen Prepared for Testing

5.2 Part B: Preparation of Slab Specimens

Slab specimens were prepared to simulate practical field conditions more accurately. Laboratory specimen preparation and compaction conditions differ significantly from actual field construction conditions. As discussed previously, asphalt mixtures experience heat loss during transportation, placement, and compaction due to environmental exposure and weather conditions. For concrete and polymer concrete, overlays are placed over larger surface areas, resulting in different heat dissipation and curing behavior compared to small laboratory specimens. In addition, field substrates may contain surface irregularities and experience temperature fluctuations that are difficult to fully replicate under controlled laboratory conditions. Therefore, slab-scale specimens were prepared to better represent practical overlay-substrate interaction and interfacial bonding behavior under field-like conditions

5.2.1 Preparation of Asphalt A-A Slabs

The preliminary tests conducted before fabricating the pilot study specimens were also repeated for the asphalt slabs. The theoretical maximum specific gravity G_{mm} was determined to be 2.539, while the residual percentage of the tack coat was found to be 63.8%.

Asphalt slabs measuring 16 in. × 12 in. × 4 in. were prepared, consisting of two layers each with a thickness of 2 in., resulting in a total slab thickness of 4 in. A schematic representation of the slab is shown in Figure 31.

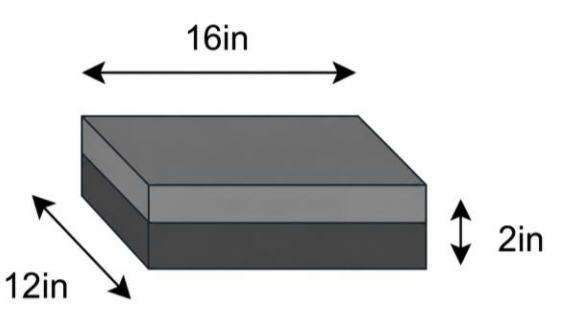

Figure 31: Schematic Representation of Asphalt Slab

The asphalt mixture was heated at 149°C for 2 hours before compaction. Paper lining was used to ensure that the substrate dimensions were slightly smaller, allowing the specimen to be easily inserted into the mold. The heated asphalt mixture was then placed into the mold and compacted using a PMW Kneading Roller Compactor until a compaction pressure of 600 psi was achieved. This procedure is shown in Figure 32.

Figure 32: (a) Pouring of Hot Asphalt Mix into the Mold, and (b) Compaction Using the PMW Kneading Roller Compactor

The substrates were allowed to cool for 24 hours before removal from the mold. The polymer lattices were then cut to dimensions of 16 in. × 12 in. The surface of the substrate was marked according to the polymer lattice pattern. Another batch of asphalt mixture was heated at 149°C for 2 hours for the preparation of the overlay layer. Tack coat was applied at a residual

application rate of 0.20 gal/yd² and allowed to break before placement of the polymer lattice. After the tack coat had broken, the polymer lattice was positioned on the substrate surface, and the heated asphalt mixture was poured over the lattice and compacted in the same manner as the substrate layer. This procedure is shown below in Figure 33.

(a) (b) (c)

Figure 33: Fabrication of Overlay- (a) Marking the Substrate, (b) Application of Tack Coat, and (c) Placement of Lattice

5.2.2 Preparation of Concrete PCC-PC Slabs

At first, the PCC substrate was mixed according to the mix design presented in Table 8. The substrate was then cast following ASTM C192 [97] and cured for 7 days. This process is shown in Figure 27. After curing, the top surface of the substrate was ground using a surface grinder to ensure proper interface conditions. The lattice was cut to match the dimensions of the substrate, then markings were made. Then, polymer concrete was cast on top. The casted overlays were cured for 24 hours before demolding them, and 7-day curing in room conditions before testing.

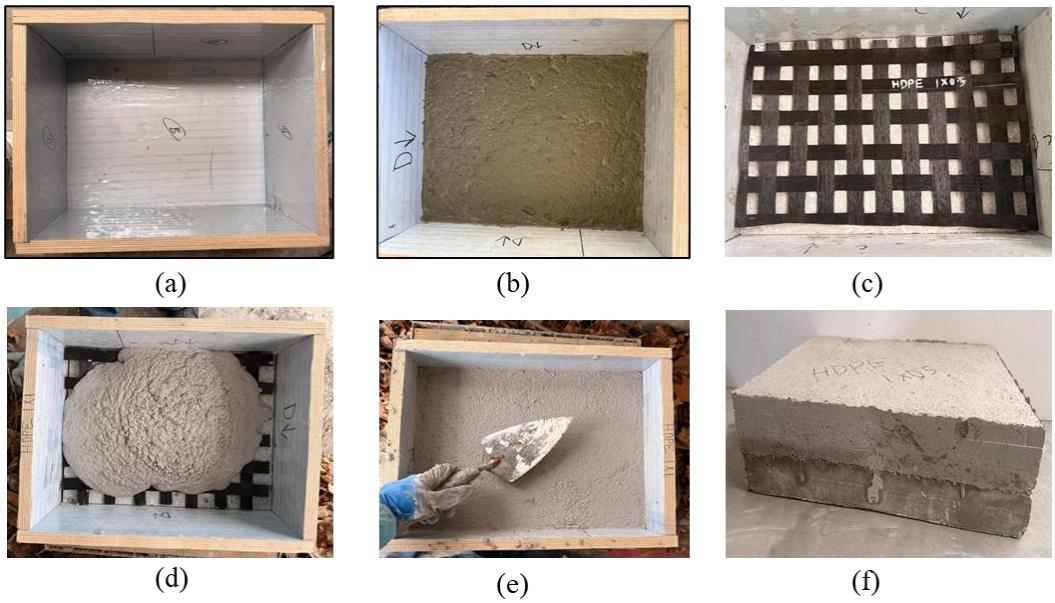

Figure 34: (a) Mold of 12 in. × 16 in. × 7 in., (b) PCC Substrate Casting, (c) Placement of Polymer Lattice on PCC Substrate in the Mold, (d) Pouring of Polymer Concrete Mixture, (e) Smoothening of the Overlay Surface, and (f) Finished PCC-PC Specimen

5.2.3 Extraction of Cores from Slabs

Four core specimens, each with a diameter of 4 in., were extracted from the prepared slabs using a Husqvarna DMS 240 core drill. A customized iron stand was fabricated to securely hold both the slab and the coring equipment in position during the extraction process. Initially, AutoCAD models, as shown in Figure 35, were prepared to determine the exact locations for core extraction. The cores were positioned such that each core contained a minimum of four openings of the polymer lattice.

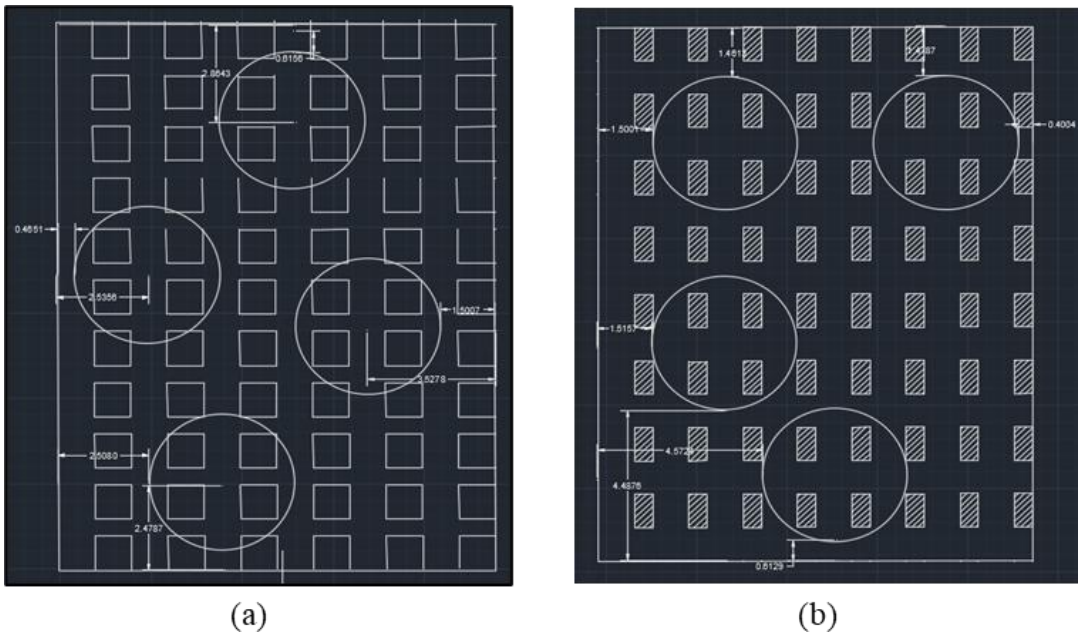

Figure 35: AutoCAD Drawings of (a) 1 in. × 1 in. Opening Size Lattice, and (b) 1 in. × 0.5 in. Opening Size Lattice

The slabs were then marked according to the predetermined dimensions to ensure accurate core positioning. Four cores were extracted from each slab at four different locations. Care was taken to avoid extracting cores near the slab edges to prevent tearing or damage to the slab during the coring process. This process is presented in Figure 36 below.

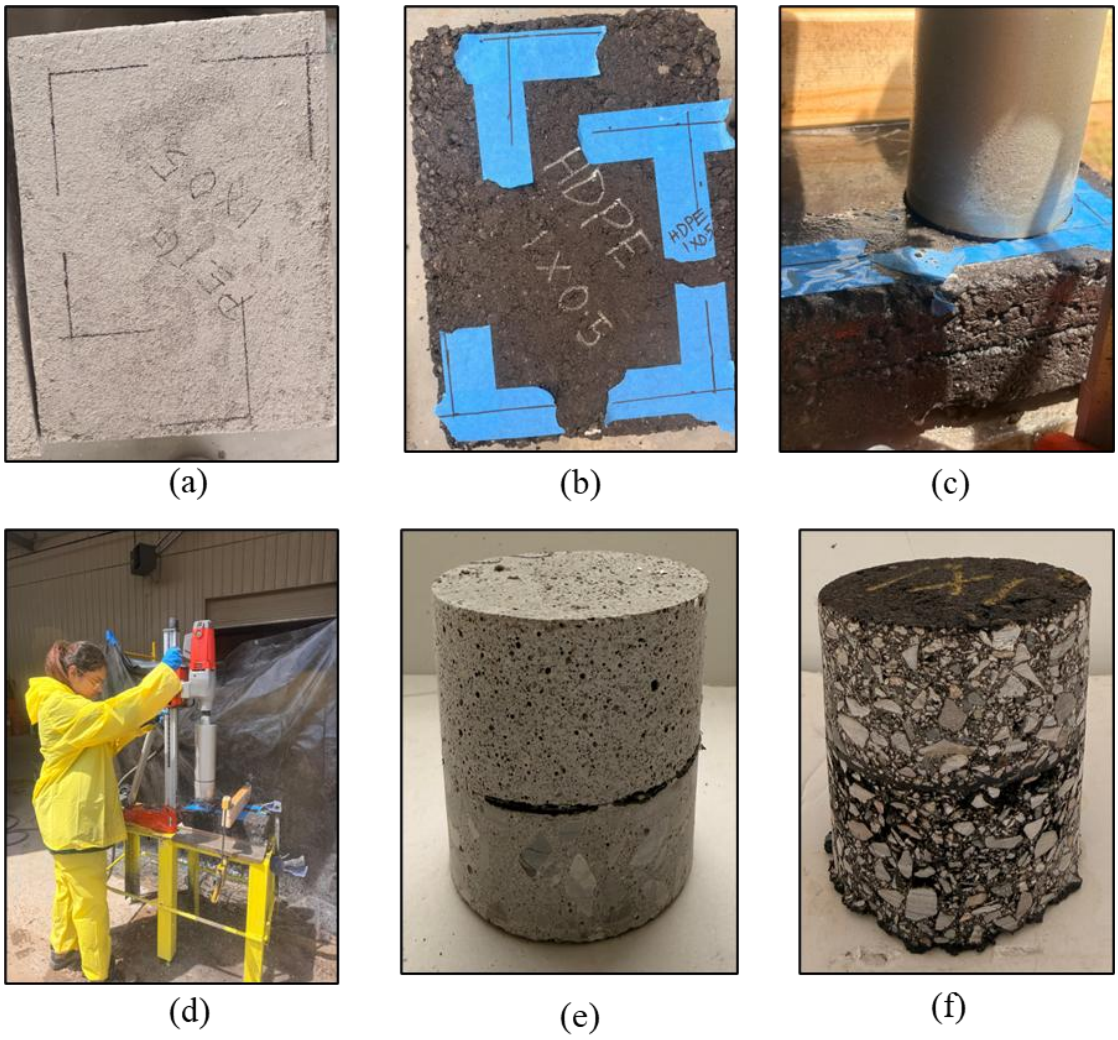

Figure 36: (a) Marked PCC-PC Slab, (b) Marked A-A Slab, (c) Coring Based on the Markings, (d) Coring of the Slab, (e) Extracted PCC-PC Core, and (f) Extracted A-A Core

5.3 Louisiana Interlayer Shear Strength Test (LISST)

The Louisiana Interlayer Shear Strength Test (LISST) apparatus, shown in Figure 9, was used to quantify the Interlayer Shear Strength (ISS) of fabricated specimens. The resulting ISS data were analyzed to determine the best-performing polymer type.

The LISST setup comprises two fixtures: a stationary jaw and a movable jaw capable of translating vertically and parallel to the interface plane. Once the double-layered asphalt specimen was secured within the fixture, the movable jaw applied a controlled vertical displacement parallel

to the interlayer, generating shear stresses along the bonded interface, as shown in Figure 37. Loading was applied at a displacement rate of 2.54 mm/min (0.1 in./min) until interfacial failure occurred according to AASHTO TP-114 [96].

The Smart Loader with a load capacity of 10 kips was used to test the pilot study specimens for the asphalt-asphalt (A-A) and portland cement concrete-portland cement concrete (PCC-PCC) systems. However, because polymer concrete possesses higher tensile strength compared to conventional PCC, an MTS testing frame with a capacity of 55 kips was utilized to test the remaining pilot study specimens and slab specimens. The Interlayer Shear Strength (ISS) was computed by dividing the maximum load at failure by the cross-sectional area of the specimen, as expressed in Equation 6.

$$\text{ISS} = \frac{\text{Peak Axial Load}}{\text{Cross} - \text{Sectional Area}} \quad [6]$$

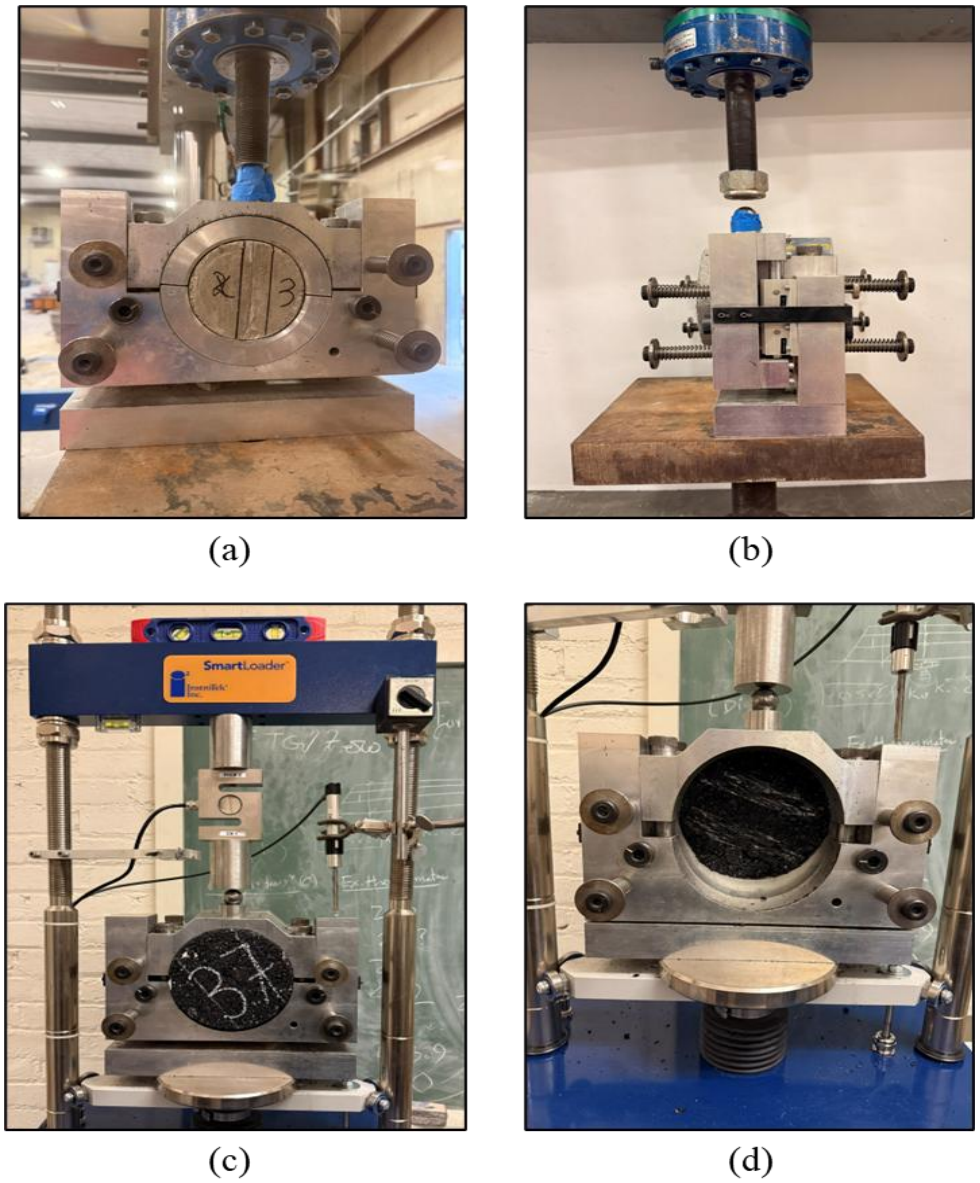

Figure 37: (a) LISST Test Setup with an MTS Frame, (b) LISST Test Running on an MTS Frame, (c) LISST Test Setup on an Asphalt Pilot Study Specimen with a Smart Loader, and (d) Specimen after Failure

Chapter 06. Results and Discussion

6.1 Compressive Strength Test

A total of six 4-in. × 8-in. cylindrical specimens with an age of 7 days were prepared to determine the compressive strengths of the polymer concrete and portland cement concrete mixtures made with the Oklahoma Department of Transportation (ODOT) Class AA mix design. In addition, three cubes were prepared to determine the compressive strength of the other PCC mix.

The average 7-day compressive strength of the ODOT Class AA concrete mixture was determined to be 20.0 ± 0.4 MPa (mean ± standard deviation), with a coefficient of variation (COV) of 1.98% . Based on the 7-day test results, the 28-day compressive strength is expected to range between 27 and 31 MPa, satisfying the minimum strength requirement specified by ODOT.

For the polymer concrete, an average compressive strength of 23.95 ± 2.24 MPa with a COV% of 9.3% was achieved after 7 days of curing. Moreover, the average compressive strength of the cube specimens was determined to be 37.99 ± 3.5 MPa with a COV% of 9.2%. Images from the tests are shown below in Figure 38.

(a) (b) (c)

Figure 38: Failed Specimens of (a) PCC Cube, (b) ODOT Class AA Cylinder, and (c) Polymer Concrete Cylinder

6.2 LISST Test Result of A-A Pilot Study Specimen

While conducting the LISST test on the asphalt pilot study specimens, several effects were observed and analyzed, as described below.

6.2.1 Effect of Polymer Type

Figure 39 presents the average interlayer shear strength (ISS) results for specimens with different polymer types tested without tack coat (NT) and oriented inclined to the shear plane. The associated variability of the test results is represented by the error bars corresponding to the standard deviation. In addition, the percentage change in ISS relative to the no tack coat control specimen is also presented. Representative failure images are presented in Figure 39.

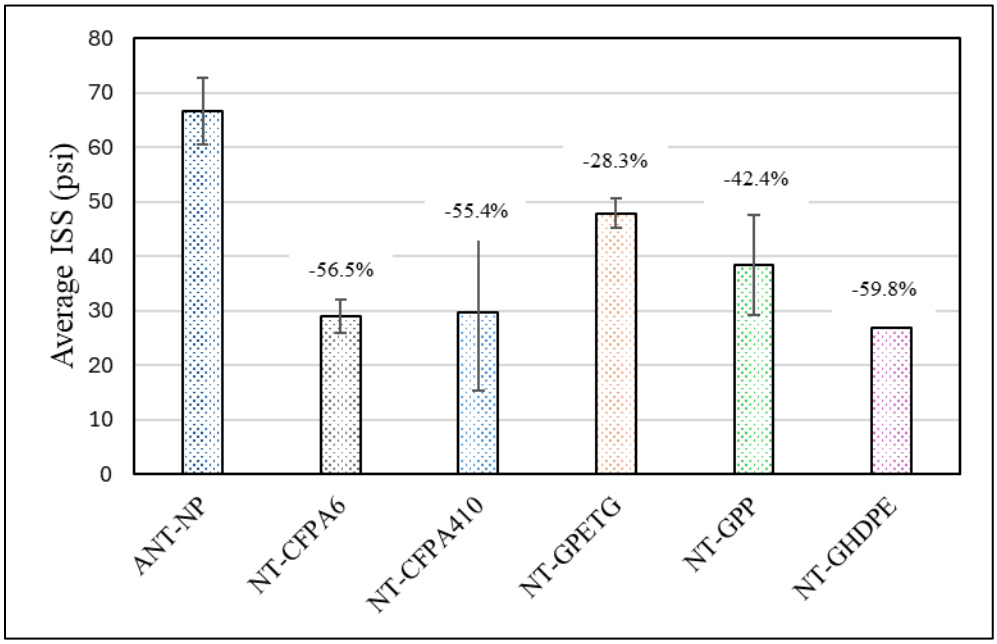

Figure 39: Effect of Polymer Type without Tack Coat on Shear Strength Tested Inclined to Shear Plane

Among the polymer types studied, NT-GPETG exhibited the highest average interlayer shear strength (ISS), with a mean value of 47.85 psi, indicating superior interlayer shear resistance

compared to the other polymers. However, NT-GPETG also showed the highest variability, with a standard deviation of 14.35 psi and a coefficient of variation (COV) of 30%, suggesting considerable inconsistency in bonding performance. This variability is likely associated with sensitivity to fiber orientation, which is discussed in detail later in this study. Compared to the no tack coat control specimen (ANP-NT), NT-GPETG exhibited a 28.3% reduction in ISS.

The NT-GPP specimens demonstrated the second-highest average ISS of 38.43 ± 2.67 psi with a relatively low COV of 2.67%, indicating stable and consistent interlayer bonding performance. Although its effectiveness was lower than that of GPETG, the lower variability suggests more uniform bonding behavior. Relative to the control specimen, NT-GPP exhibited a 42.4% decrease in ISS.

Both carbon fiber reinforced polyamides, NT-CFPA6 and NT-CFPA410, exhibited similar average ISS values of 29.00 ± 4.10 psi and 29.73 ± 3.10 psi, respectively, reflecting moderate interlayer bonding performance. The corresponding COV values were 14.14% for NT-CFPA6 and 10.35% for NT-CFPA410, indicating comparatively consistent behavior among the carbon fiber reinforced systems. The ISS values for NT-CFPA6 and NT-CFPA410 were reduced by 56.5% and 55.4%, respectively, compared to the control specimen.

The lowest average ISS was observed for NT-GHDPE, with a mean value of 26.83 ± 9.23 psi and the highest COV value of 34.4%, indicating substantial variability in bonding performance. Compared to the control specimen, NT-GHDPE demonstrated a 59.8% reduction in ISS, indicating the least effective interlayer bonding performance among the polymer systems studied. Post-failure examination of the specimens revealed partial de-bonding and damage to the polymer tapes in all cases shown in Figure 40.

.

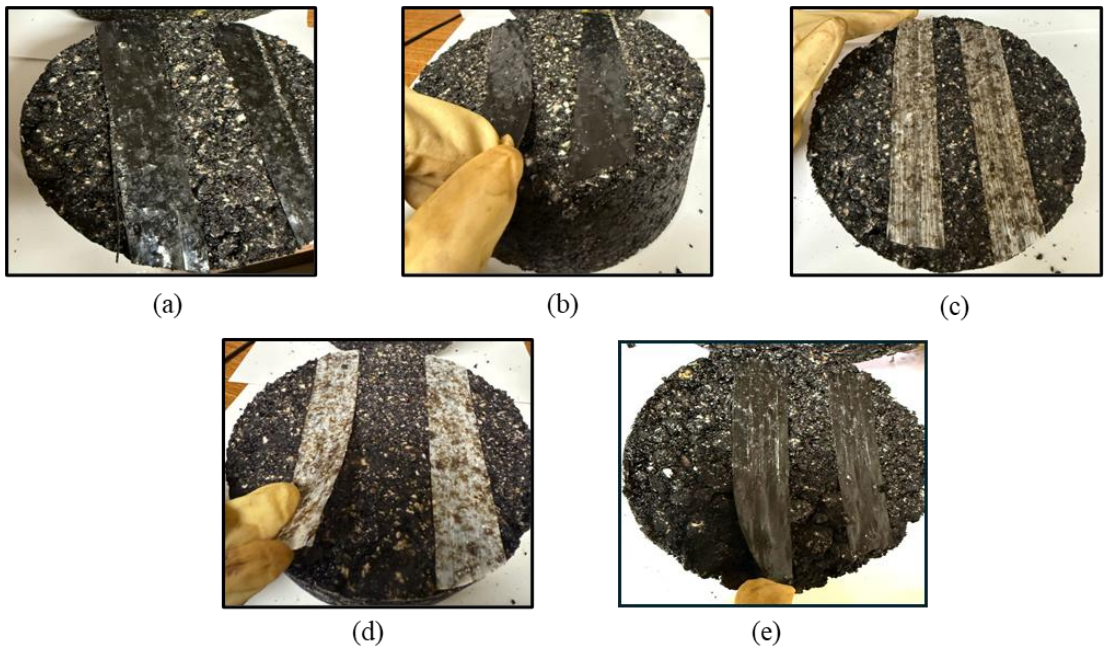

Figure 40: Failed Interlayers of: (a) NT-CPA6, (b) NT-CPA410, (c) NT-GPETG, (d) NT-GPP, (e) NT-GHDPE

The least partial de-bonding was observed in the G-PETG specimens, indicating comparatively improved interfacial adhesion. However, failure was predominantly observed at the interface for all specimens, signifying that interlayer bonding remained the governing weakness.

The reduced interlayer shear strength of the GHDPE specimens can be attributed to the exceptionally low glass transition temperature of HDPE (approximately -100°C to -130°C), which results in a soft and highly mobile amorphous phase at room temperature [89]. As a result, premature local deformation and early interfacial de-bonding were observed at the GHDPE interfaces (Figure 13(e)), thereby limiting the ability of the interface to transfer shear stresses and resist sliding [14].

In contrast, PETG is characterized by a substantially higher glass transition temperature (approximately 80°C to 82°C), allowing a rigid, glassy state to be maintained at room temperature [87]. This increased stiffness was associated with enhanced interfacial confinement and shear stress

transfer, which is consistent with the improved bonding behavior and the highest interlayer shear strength values observed for the G-PETG specimens.

6.2.2 Effect of Tack Coat

The average interlayer shear strength values and percent changes relative to the corresponding no tack coat cases tested inclined to the shear plane are illustrated in Figure 41. For the control specimens, the application of tack coat increased the average ISS from 66.7 ± 8.2 psi for ANT-NP to 79.8 ± 4.1 psi for AT-NP, corresponding to a 19.6% increase in interlayer shear resistance.

For the C-PA6 system, the NT-CPA6 specimens exhibited an average ISS value of 29.0 ± 4.1 psi, corresponding to a 56.5% reduction relative to the control specimen. Following tack coat application, the T-CPA6 specimens exhibited an increased ISS value of 46.4 ± 6.15 psi, reducing the ISS loss to 30.4%.

Similarly, the C-PA410 system demonstrated improved performance after tack coat application. The NT-CPA410 specimens exhibited an ISS value of 29.7 ± 3.1 psi, corresponding to a 55.4% reduction relative to the control specimen. The T-CPA410 specimens showed an ISS value of 42.8 ± 3.08 psi, corresponding to a smaller reduction of 35.9%.

Among the evaluated thermoplastic systems, the GPETG specimens exhibited the highest overall ISS values. The NT-GPETG specimens demonstrated an ISS value of 47.9 ± 14.35 psi, corresponding to a 28.3% reduction relative to the control specimen. After tack coat application, the ISS increased to 52.9 ± 2.05 psi for the T-GPETG specimens, corresponding to only a 20.6% reduction relative to the control specimen.

For the GPP system, the NT-GPP specimens exhibited an ISS value of 38.4 ± 2.67 psi, corresponding to a 42.4% reduction relative to the control specimen. The T-GPP specimens showed a slightly improved ISS value of 39.9 ± 3.08 psi, corresponding to a 40.2% reduction.

In contrast, the GHDPE system exhibited the lowest overall interlayer performance. The NT-GHDPE specimens demonstrated an ISS value of 26.8 ± 9.23 psi, corresponding to a 59.8% reduction relative to the control specimen. After tack coat application, the ISS further decreased to 18.1 ± 2.05 psi for the T-GHDPE specimens, corresponding to a 72.8% reduction.

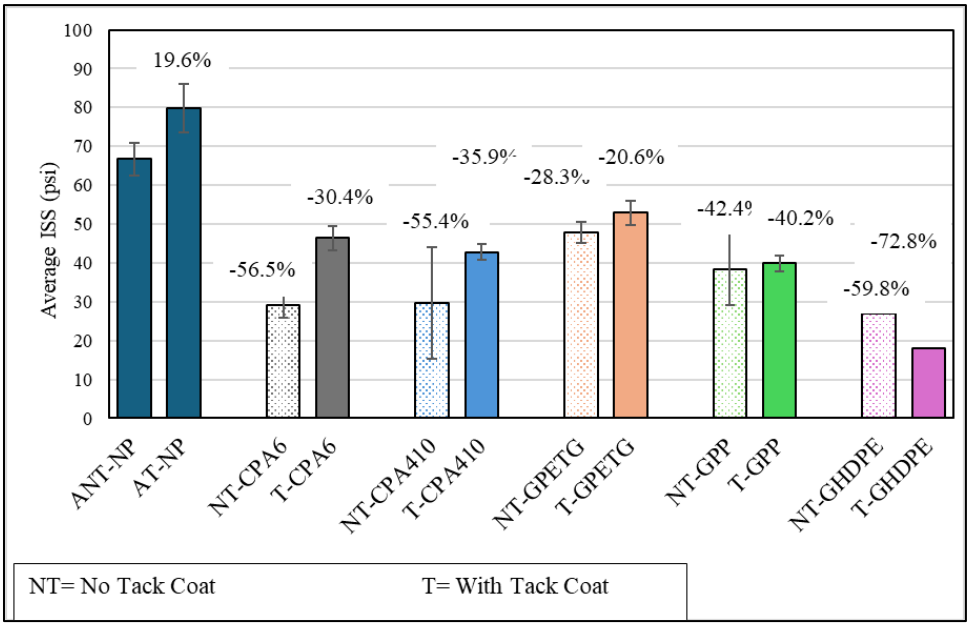

Figure 41: Comparison of the Average Shear Strength Values between Polymers with and without Tack Coat Tested Inclined to Shear Plane

The increase in ISS values in tack-coated cases relative to those without tack coat has been observed for polyamide-based interfaces, which was attributed to the relatively high surface energy of these materials. Polyamide-based tapes, including CFPA6 and CFPA410, are reported to exhibit surface energy values of approximately 42.9 mJ/m^2 [98] and 41.3 mJ/m^2 [99], respectively, arising from the presence of amide functional groups that contribute to their polar surface characteristics.

This relatively high surface energy promotes improved wetting and adhesive interaction with the asphalt tack coat, resulting in enhanced interfacial bonding and increased shear resistance. In contrast, polymer tapes with lower surface energy, such as polypropylene and HDPE, exhibited reduced wettability and weaker adhesive interaction with the tack coat [71]. It was also observed from the post-failure images of G-HDPE and G-PP that little to no tack coat was absorbed by these tapes, as shown in Figure 42. As a result, the tack coat acted as a slipping layer rather than improving interfacial bonding.

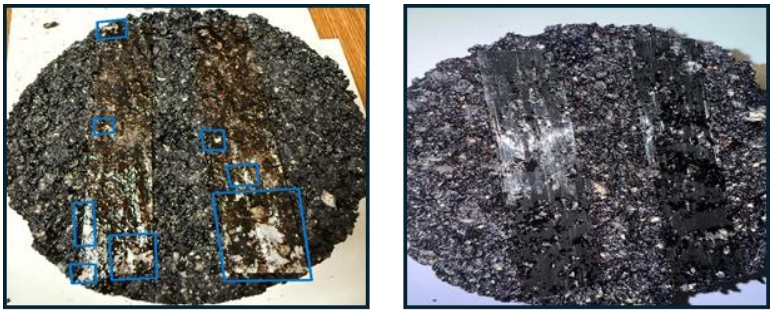

(a) (b)

Figure 42: Post-Failure Image of (a)G-PP, and (b)G-HDPE

6.2.3 Effect of Heated Tape

A study was conducted to identify polymer tapes that begin softening near the asphalt placement temperature of 160°C to justify further heating-based investigation. G-HDPE exhibited gradual texture change and softening between approximately 130°C and 135°C, followed by clear adhesion to asphalt at an average temperature of about 187°C. This temperature range was considered compatible with conventional asphalt placement conditions. Although a burning odor was observed at temperatures above 218°C.

In contrast, CF-PA410, CF-PA6, G-PETG, and G-PP exhibited unfavorable responses, including early curling, color change, thermal degradation, and inconsistent or absent adhesion to

asphalt even at elevated temperatures. These behaviors indicated inadequate thermal stability and poor interfacial compatibility with asphalt. Images from the heating trials are shown in Figure 43.

(a) (b) (c)

Figure 43: (a) Burning and Curling of G-PETG Tape, (b) Softening of G-HDPE Tape, (c) Extreme Softening without Asphalt Adhesion of C-PA6 Tape

Accordingly, G-HDPE was selected as the only suitable material for continued evaluation. The GHDPE tapes were subjected to localized heating using a heat gun, as shown in Figure 5. The tapes were heated to approximately their glass transition temperature to soften the material and promote adhesion at the interface. However, the average interlayer shear strength obtained by testing the tapes inclined to the shear plane with the heated tapes was 13.05 ± 2.05 psi, which represents a 51.36% reduction compared to the average shear strength measured for specimens without tape heating tested at an inclined orientation to the shear plane. This result indicates that localized heating of the GHDPE tape adversely affected interlayer shear performance rather than improving adhesion. Figure 44 (a) shows a comparison of the average interlayer shear strength between specimens with heated tapes and those without heated tapes, and Figure 44 (b-c) presents representative post-experiment images.

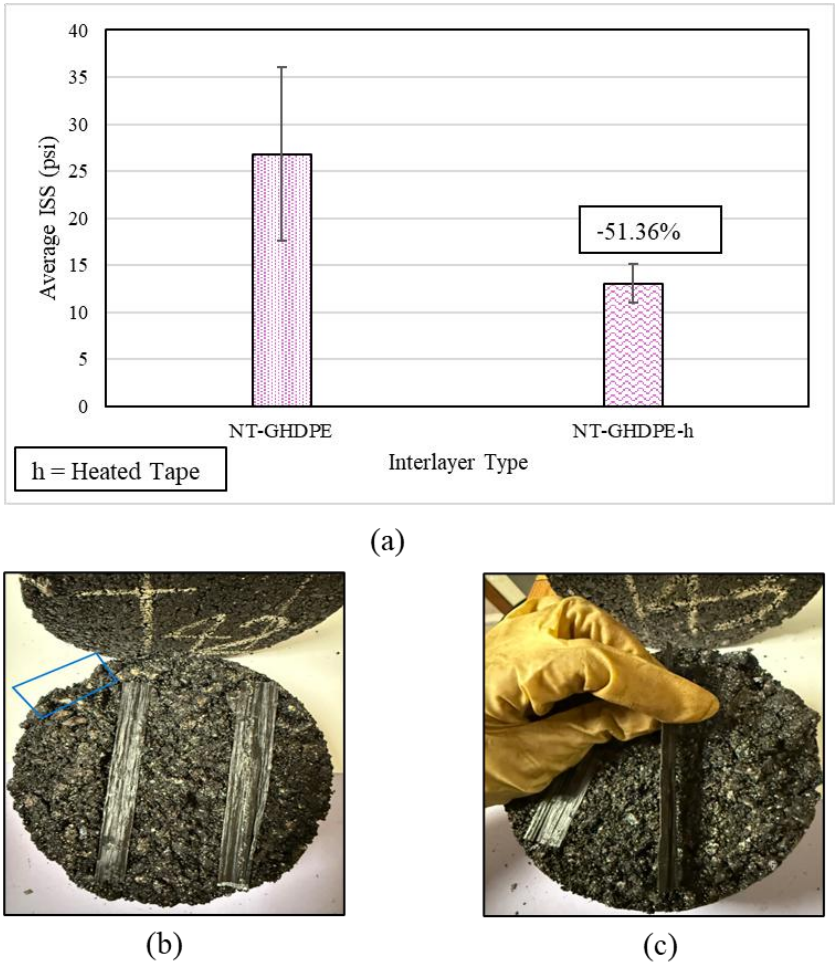

Figure 44: (a) Average ISS Comparison between Specimens with and without Heated Tapes Tested Inclined to Shear Plane, (b-c) Post-Failure Image of Interfacial De-bonding of Tape, and Folding of Tape

6.2.4 Effect of Loading Direction

Parallel and perpendicular orientations relative to the shear plane were evaluated along with inclined fiber orientations. All specimens were prepared with tack coat. Figure 47 compares the average interlayer shear strength (ISS) values for the different fiber orientations together with the corresponding percentage changes relative to the no tack coat control specimen (ANP-NT). Overall, the incorporation of FRP tapes resulted in lower ISS values compared to the control

specimen; however, the orientation of the fibers significantly influenced the interlayer bonding performance.

For the T-CFPA6 system, the inclined orientation exhibited the highest ISS value of approximately 46 psi, corresponding to a 30.4% reduction relative to the control specimen. The parallel orientation resulted in a lower ISS value with a 43.5% reduction, whereas the perpendicular orientation demonstrated improved performance compared to the parallel case, with only a 26.1% reduction.

Similarly, for the T-CFPA410 system, the inclined orientation produced an ISS value corresponding to a 35.8% reduction relative to the control specimen. The parallel orientation exhibited slightly improved performance with a 30.4% reduction, while the perpendicular orientation resulted in a 39.1% decrease in ISS.

Among all evaluated systems, T-GPETG exhibited the highest ISS in the inclined orientation, reaching approximately 53 psi and corresponding to only a 20.7% reduction relative to the control specimen. In contrast, the parallel and perpendicular orientations resulted in larger reductions of 45.7% and 37.0%, respectively, indicating that inclined fiber orientation significantly improved interlayer shear resistance for the GPETG system. A comparison of the fiber angles is shown below in Figure 45.

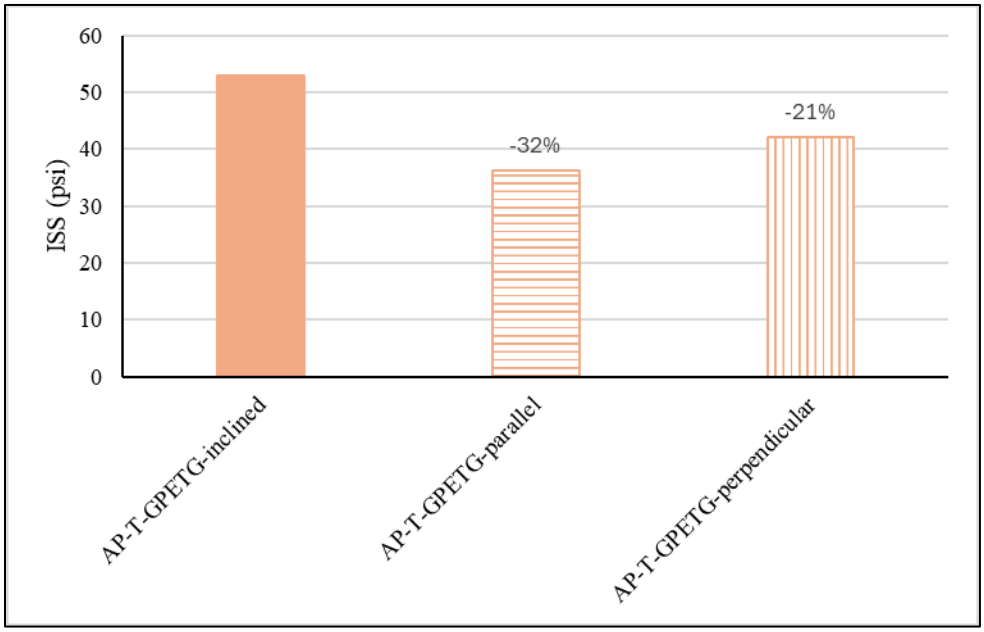

Figure 45: Influence of Fiber Orientation on ISS Performance of T-GPETG Specimens

For the T-GPP specimens, the inclined orientation again produced the highest ISS value, corresponding to a 42.4% reduction relative to the control specimen. The parallel and perpendicular orientations demonstrated larger reductions of 54.3% and 47.8%, respectively, indicating lower interfacial resistance when fibers were aligned parallel or perpendicular to the shear plane. A comparison is shown below in Figure 46.

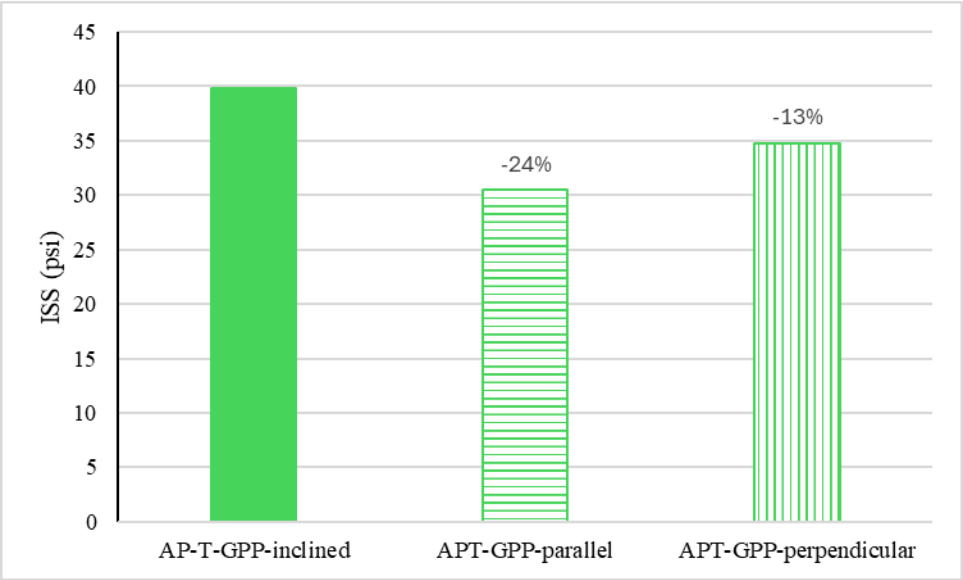

Figure 46: Influence of Fiber Orientation on ISS Performance of T-GPP Specimens

The T-GHDPE specimens exhibited the lowest overall ISS values among the evaluated systems. The inclined orientation resulted in a 59.8% reduction relative to the control specimen, whereas the parallel and perpendicular orientations demonstrated reductions of 40.0% and 21.3%, respectively. Unlike the other polymer systems, the perpendicular orientation for GHDPE produced comparatively improved interlayer performance.

Overall, fiber orientation was found to significantly influence interlayer shear resistance. Inclined fiber orientations generally resulted in improved ISS performance for most polymer systems, particularly for GPETG and GPP specimens, suggesting that inclined fiber alignment may enhance stress transfer and resistance to interfacial sliding.

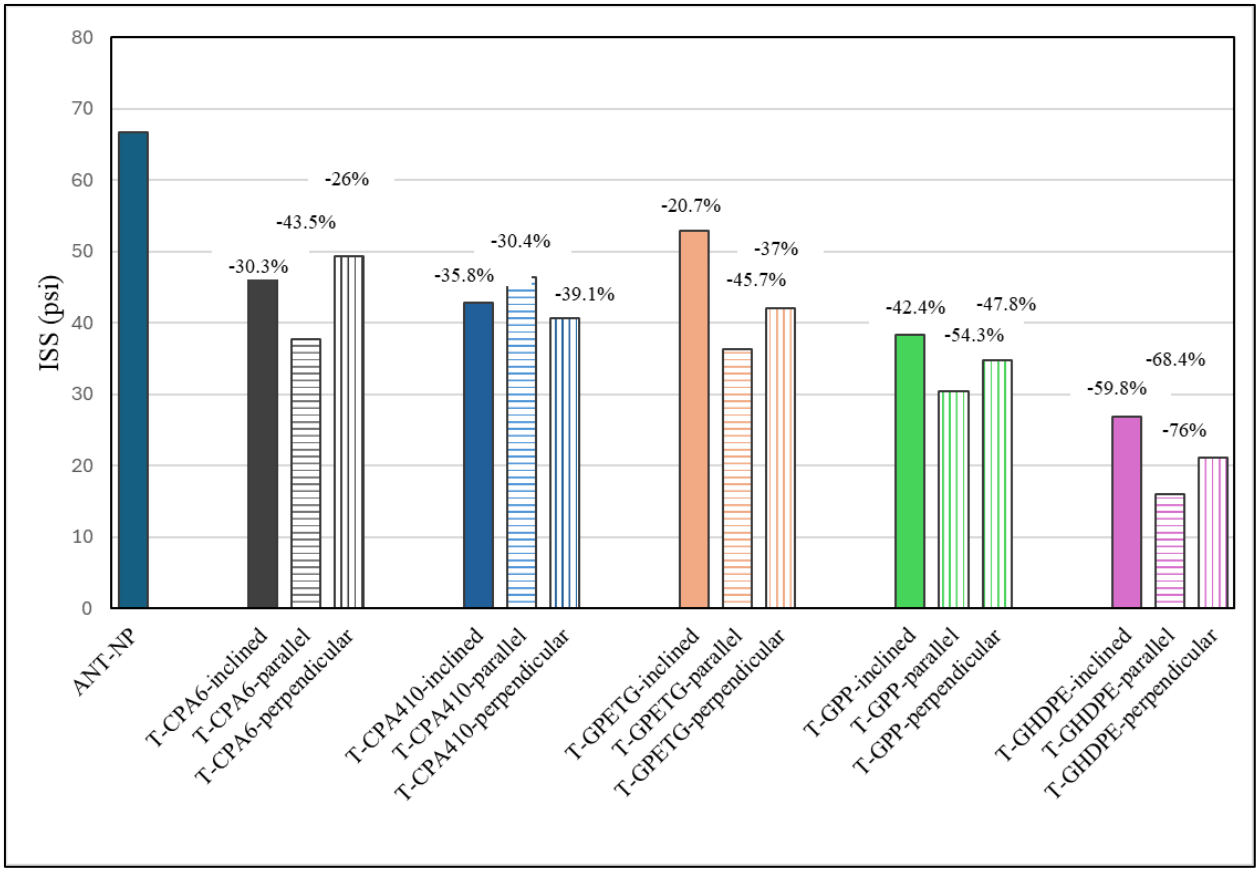

Figure 47: Comparison of the Shear Strength Values between Polymers Tested at Different Fiber Orientations

As shown in Figure 47, specimens with inclined fiber orientation generally exhibited higher average interlayer shear strength than specimens with fibers oriented either parallel or perpendicular to the shear plane, despite the conventional expectation that fibers aligned with the loading direction would provide higher tensile resistance [100]. For most polymer systems, parallel and perpendicular orientations resulted in reductions in average ISS relative to the inclined fiber orientation configuration. This behavior can be explained by the microscopic observations obtained using the Keyence VHX-7000 microscope equipped with the E20 lens, as presented in Table 8. The presence of fibers within the tape was observed to restrict crack initiation and propagation across the interface. When fibers are oriented at intermediate angles rather than strictly parallel or

perpendicular to the shear plane, more effective crack-resistance to shear-induced damage was provided, resulting in higher average interlayer shear strength.

From the post-failure images shown in Figure 48, similar failure patterns were observed across all specimens, irrespective of loading direction. Cracking was predominantly concentrated at the interface, while only minimal cases of partial de-bonding were identified.

(a) (b)

Figure 48: Post-Failure Image of (a) T-CPA410-perpendicular, and (b)T-GPETG-parallel

6.3 LISST Test Result of PCC-PCC Pilot Study Specimens

Figure 49 presents the average interlayer shear strength (ISS) values of different PCC-based specimen configurations along with their corresponding standard deviations and percentage changes relative to the control PCC specimen. The control PCC specimen exhibited an average ISS of 174.59 ± 13.45 psi.

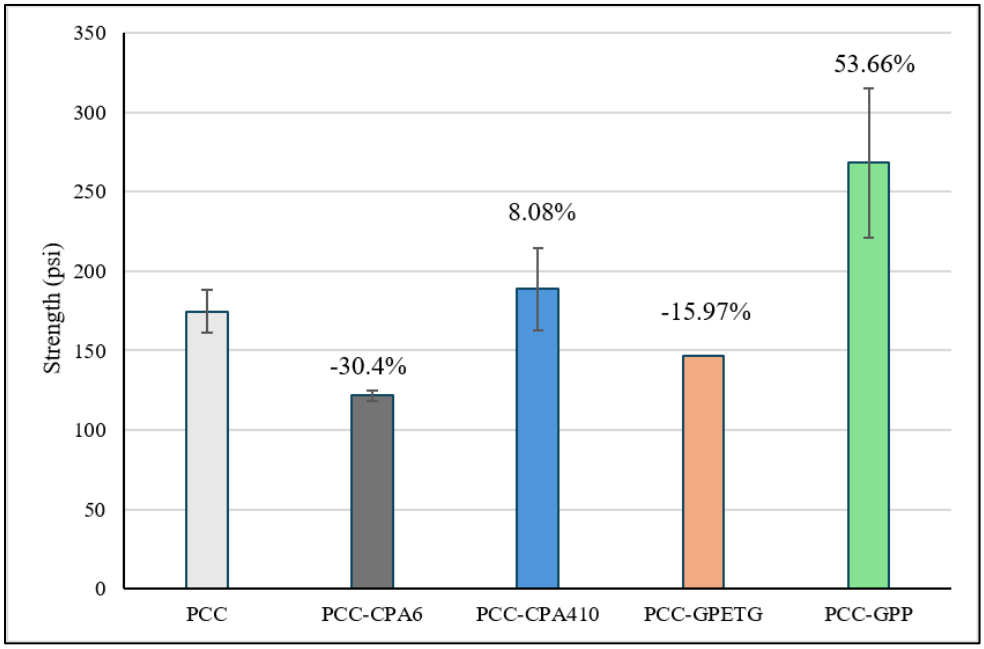

Figure 49: Comparison of Different Polymer Types on Average Interlayer Shear Strength

Among the FRP-reinforced specimens, PCC-CPA6 showed the lowest average ISS value of 121.55 ± 3.25 psi, representing a 30.38% reduction in ISS compared to the control specimen. In contrast, PCC-CPA410 exhibited an average ISS of 188.69 ± 25.65 psi, corresponding to an 8.08% increase relative to the control PCC specimen.

The PCC-GPETG specimen demonstrated an average ISS of 146.71 psi, resulting in a 15.97% reduction in ISS compared to the control specimen. Among all specimen configurations, PCC-GPP achieved the highest average ISS value of 268.27 ± 47 psi, corresponding to a 53.66% increase in ISS relative to the control PCC specimen.

Overall, the results indicate that the type of polymer tape had a significant influence on interlayer shear strength performance. While CPA6 and GPETG reduced the interlayer shear resistance, CPA410 and especially GPP improved the ISS performance of the PCC-based systems.

The post-failure images are shown in Figure 50. All specimens, except PCC-GPP, failed at the interface. This indicates that, in the PCC-GPP specimens, the interlayer bond strength exceeded

the tensile strength of the concrete, causing the crack to propagate into the PCC layer instead of along the interface.

The superior ISS performance observed for the PCC-GPP specimens may be associated with previous research reporting that surface roughness and mechanical interlocking of polypropylene fibers can significantly enhance bonding within the cementitious matrix [101].

The PCC-GPP specimens exhibited crack propagation from the interface into the top layer, as observed in Figure 50 (a). None of the tapes showed visible signs of rupture or damage after testing. However, partial de-bonding was observed in the C-PA6 and C-PA410 specimens, indicating weaker interlayer interaction compared to the G-PP specimens.

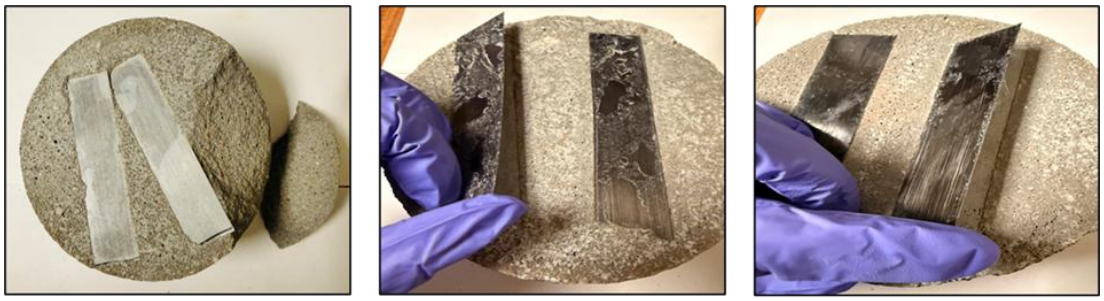

Figure 50: Post-failure images of PCC specimens- (a)G-PP, (b)C-PA6, and (c)C-PA410

6.4 LISST Test Result of PCC-PC Pilot Study Specimens

Figure 51 presents the average interlayer shear strength (ISS) values of different PCC-PC - based specimen configurations along with their corresponding standard deviations and percentage changes relative to the control NF specimen.

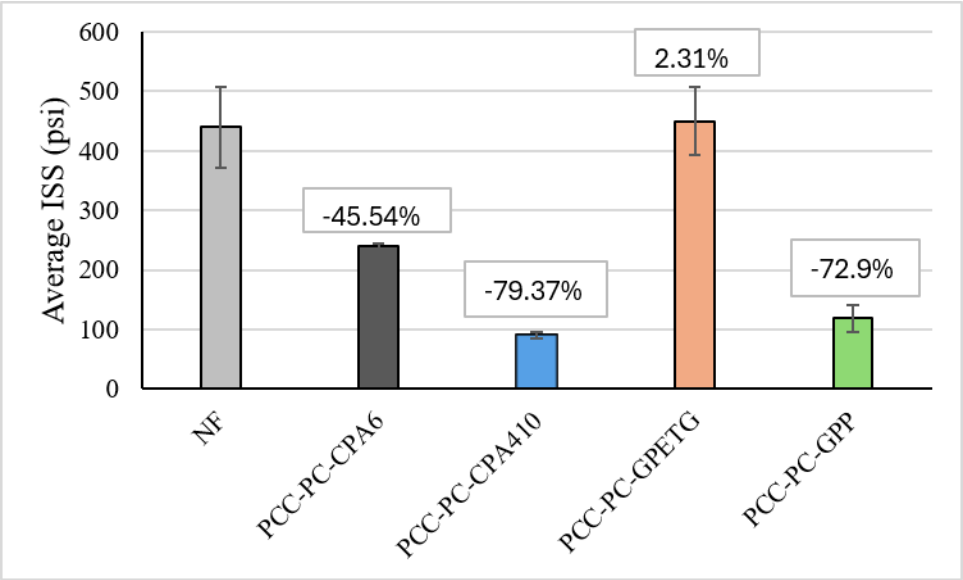

Figure 51: Comparison of Different Polymer Types on Average Interlayer Shear Strength

The PCC-PC-GPP specimens exhibited the highest interlayer shear strength (ISS) among all specimen types, with an average value of 449.5 ± 57.42 psi. Compared to the NF control specimens, the ISS increased by approximately 15%, indicating that the G-PETG reinforcement improved the interfacial bonding performance of the PCC-PC system. Although a COV% of 12.8% was observed, the specimens still demonstrated the best overall bonding behavior.

The NF control specimens exhibited an average ISS value of 439.35 ± 67.67psi with a COV% of 15.4%, demonstrating relatively strong bonding performance even without FRP reinforcement.

The PCC-PC-CPA6 specimens showed an average ISS value of 239.25 psi, corresponding to approximately a 39% reduction in ISS relative to the NF specimens. This reduction suggested that the reinforcement did not improve the bonding behavior of the PCC-PC interface.

The PCC-PC-CPA410 specimens exhibited the lowest ISS value of 90.63 ± 5.13 psi with a COV of 5.7%. Compared to the NF specimens, the ISS decreased by approximately 77%,

indicating significantly weaker interlayer bonding performance despite the relatively consistent test results.

The PCC-PC-GPP specimens exhibited the lowest ISS value of 118.9 ± 22.56 psi with a COV of %. Compared to the NF specimens, the ISS decreased by approximately 72.94%.

To further evaluate the interfacial behavior of the reinforced systems, the load–displacement responses obtained during shear testing were examined.The load-displacement curves obtained from two replicate specimens of each PCC–PC system are presented in Figure 52. All specimens exhibited an increase in load with increasing displacement until a peak load was reached, followed by a sudden load drop indicating brittle failure. The NF specimens developed peak loads ranging from 22.2 to 27.4 kN, demonstrating strong bonding between the PCC substrate and PC overlay. Similar peak loads were observed for the PCC-PC-GPETG specimens (22.3-27.3 kN), indicating that the GPETG tape maintained effective load transfer across the interface. In contrast, the PCC-PC-CFPA6 specimens exhibited peak loads of approximately 13.0-13.2 kN. Substantially lower peak loads were observed for the PCC-PC-GPP specimens (5.6-7.3 kN) and PCC-PC-CFPA410 specimens (4.6-5.0 kN). These results indicate that the type of FRP tape significantly influenced the interfacial behavior, with PCC-PC-GPETG providing the highest load-carrying capacity among the reinforced systems and PCC-PC-CFPA410 exhibiting the lowest resistance to shear loading.

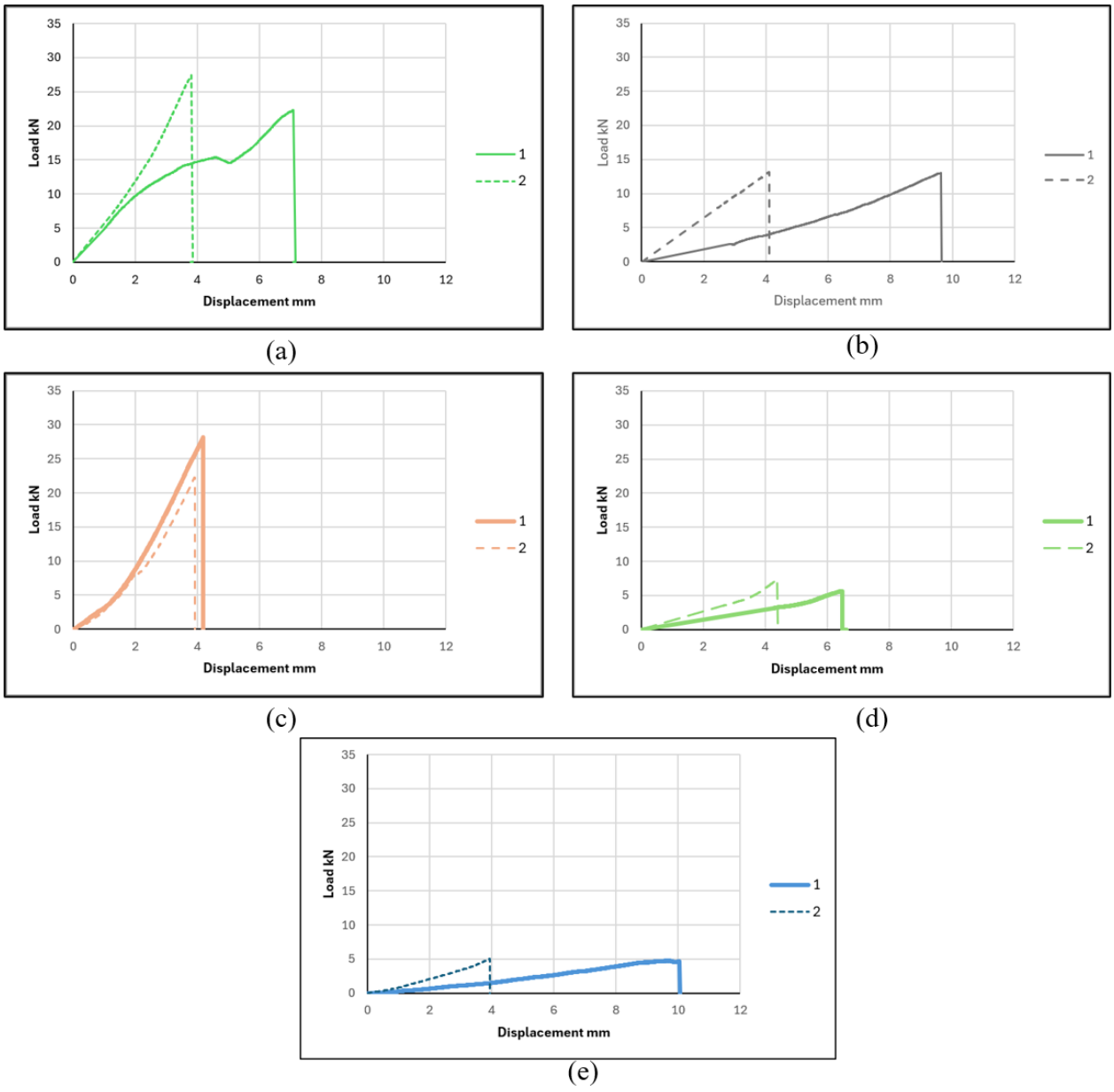

Figure 52: Comparison of Load–Displacement Responses Obtained from Replicate Specimens for (a) NF, (b) PCC–PC–CFPA6, (c) PCC–PC–CFPA410, (d) PCC–PC–GPETG, and (e) PCC-PC-PP

The representative load-displacement curves for the NF and FRP-reinforced PCC-PC systems are presented in Figure 53. Distinct differences in deformation behavior and interfacial stiffness were observed among the evaluated systems. The NF and PCC-PC-GPETG specimens exhibited the steepest load–displacement responses, indicating greater resistance to interfacial deformation and higher stiffness. In contrast, the PCC-PC-CFPA410 and PCC-PC-GPP specimens exhibited

shallower slopes throughout the loading process, suggesting lower stiffness and increased susceptibility to deformation under shear loading. The PCC-PC-CFPA6 specimens exhibited an intermediate response between these two extremes. The results indicate that the GPETG tape maintained interfacial stiffness comparable to that of the NF specimens, whereas the CFPA410 and GPP tapes resulted in a more compliant interface.

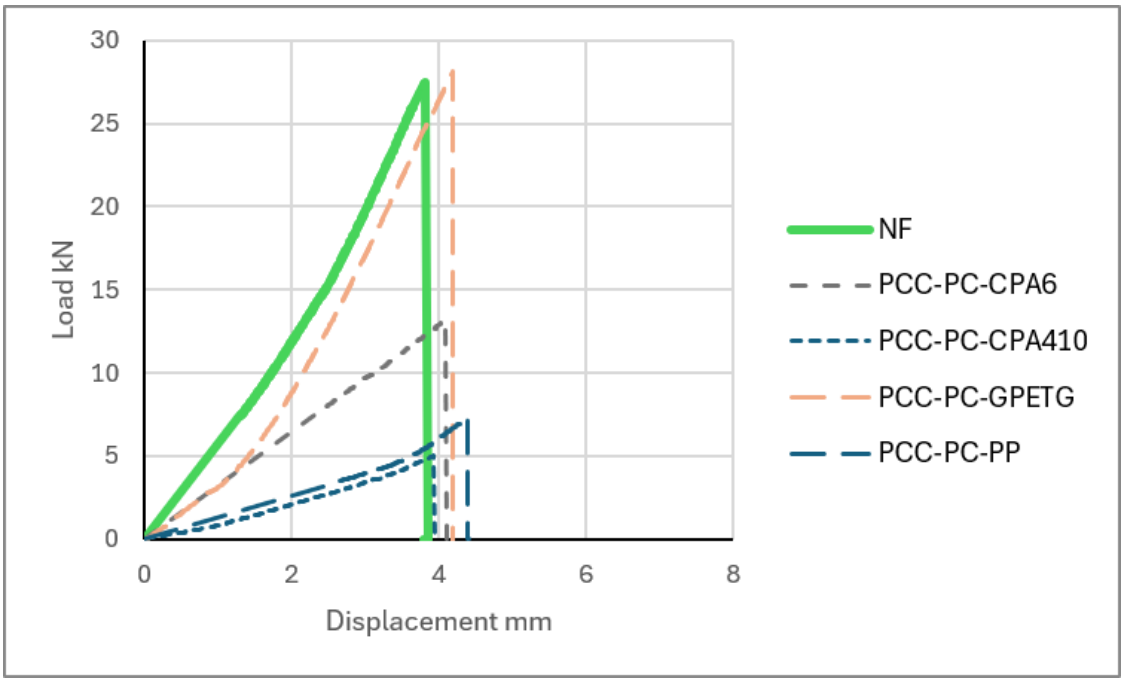

Figure 53: Comparison of Representative Load–Displacement Curves for NF, PCC-PC-CFPA6, PCC-PC-CFPA410, PCC-PC-GPETG, and PCC-PC-GPP Specimens

After analyzing the post-test specimens shown in Figure 54, it was observed that the control specimen (NF) and G-PP exhibited crack propagation from the interlayer into the PCC substrate, indicating relatively good bonding at the interface. In contrast, the PCC-PC-CPA6 and PCC-PC-CPA410 specimens primarily failed at the interlayer, suggesting weaker interlayer bonding between the reinforcement system and the surrounding materials.

However, the PCC-PC-GPETG specimens exhibited a different failure mechanism. The PCC-PC-GPETG tape became strongly embedded within the polymer concrete overlay, and after testing, crack propagation was observed mainly within the PCC substrate rather than along the reinforced interface. This behavior indicated that the bond between the PCC-PC-GPETG reinforcement and the polymer concrete layer was stronger than the internal tensile resistance of the PCC substrate itself.

The improved performance of the PCC-PC-GPETG specimens was therefore associated with the strong embedment and effective mechanical anchorage provided by the GPETG reinforcement within the polymer concrete layer. As a result, the reinforced interface no longer acted as the weakest plane in the system, resulting in superior stress transfer and the highest average ISS among all specimen types.

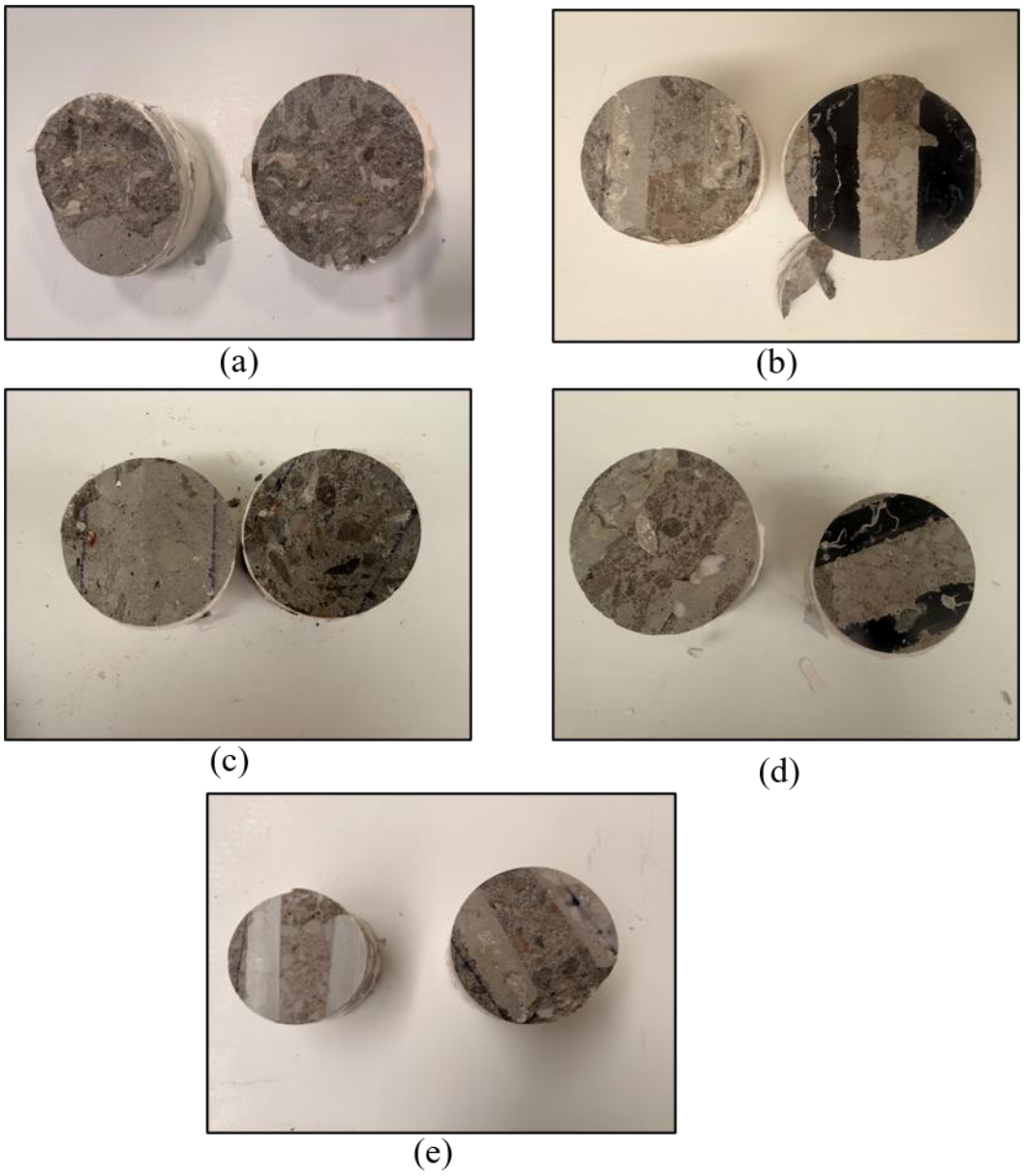

Figure 54: Post-failure image of (a) NF, (b) PCC-PC-CPA410, (c)PCC-PC-GPETG, (d) PCC-PC-CPA6, and (e) PCC-PC-GPP

6.5 LISST Test Result of A-A Slab Specimens

Figure 53 shows the influence of different polymer lattice opening sizes on the interlayer shear strength (ISS) performance of asphalt slab cores. The error bars represent the standard

deviation of the test results, while the percentage values indicate the percent change in ISS relative to the control specimen with only tack coat.

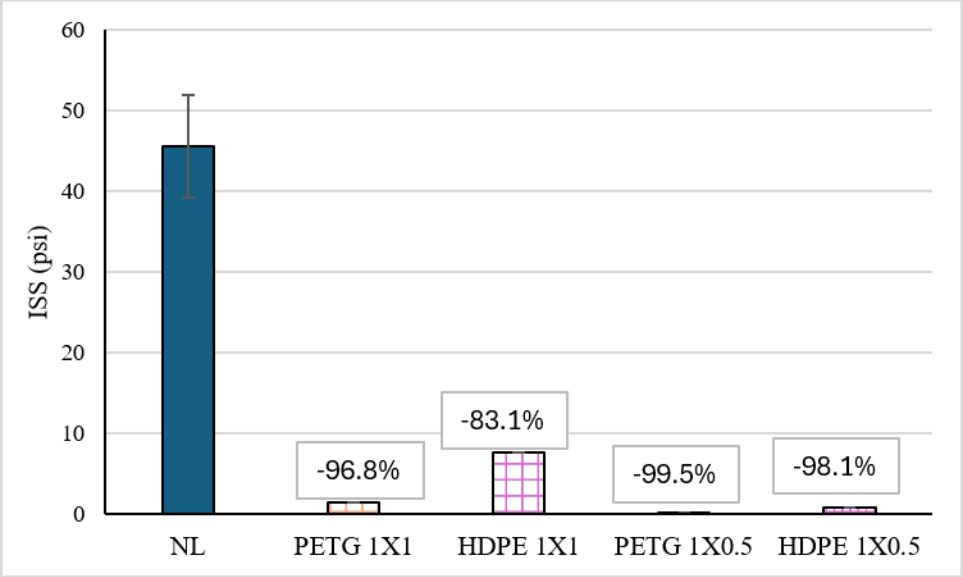

Figure 55: Effect of Polymer Lattice Opening Size on Asphalt Slab Core Performance

The control asphalt specimens without polymer lattice reinforcement exhibited the highest interlayer shear strength (ISS), with an average value of 45.6 ± 6.3 psi and a coefficient of variation (COV) of 13.72%. All polymer lattice systems resulted in substantial reductions in ISS relative to the control specimen.

Among the evaluated lattice systems, the HDPE-1×1 specimens exhibited the highest ISS value of approximately 7.69 psi, corresponding to an 81.3% reduction relative to the control specimen, indicating the best performance among the reinforced asphalt slab specimens. In contrast, the PETG-1 × 0.5 specimens exhibited the lowest ISS value of approximately 0.24 psi, corresponding to a 99.5% reduction, indicating severely reduced interlayer bonding performance.

The PETG-1×1 specimens demonstrated an ISS value of approximately 1.45 psi with a 96.8% reduction relative to the control specimen. Similarly, the HDPE-1×0.5 specimens exhibited

an ISS value of approximately 0.87 psi, corresponding to a 98.1% reduction relative to the control specimen. Although the overall ISS remained low, the larger 1×1 opening size exhibited improved performance compared to the PETG-1×0.5 configuration. Similarly, the HDPE-1×0.5 specimens exhibited an ISS value which was substantially lower than the ISS value of the HDPE-1×1 specimens.

Overall, larger lattice opening sizes generally resulted in improved ISS performance for both PETG and HDPE systems. The improved performance associated with the 1×1 opening configuration may be attributed to enhanced aggregate interlocking and improved mechanical interaction between the asphalt layers through the larger lattice openings.

Although four specimens were cored from each slab, only one valid test result could be reported for each configuration because several specimens failed before testing. In particular, one PETG 1 × 1 specimen was separated immediately after coring. In addition, the slab control specimen showed a comparatively lower ISS value of 45.6 ± 6.3 psi than the pilot study control specimen prepared with the same tack coat, which exhibited an ISS value of 79.8 ± 4.1 psi.

The lower shear strength observed in the asphalt slab specimens may have been influenced by heat loss during slab preparation. Due to the compaction mechanism of the PMW Kneading Roller Compactor, a longer duration was required between placing the asphalt mixture and initiating compaction. In contrast, during Superpave Gyratory Compactor (SGC) specimen preparation, the delay between mixture placement and compaction was minimal. The additional delay during slab preparation likely caused a greater reduction in mixture temperature, which may have reduced mixture workability and bonding around the polymer lattice [81]. As a result, the increased heat loss may have contributed to the reduced interlayer shear strength observed in the slab specimens.

This observation may also be correlated with the post-failure condition of the specimens shown in Figure 54, where all polymer lattices remained attached to the bottom asphalt layer after testing.

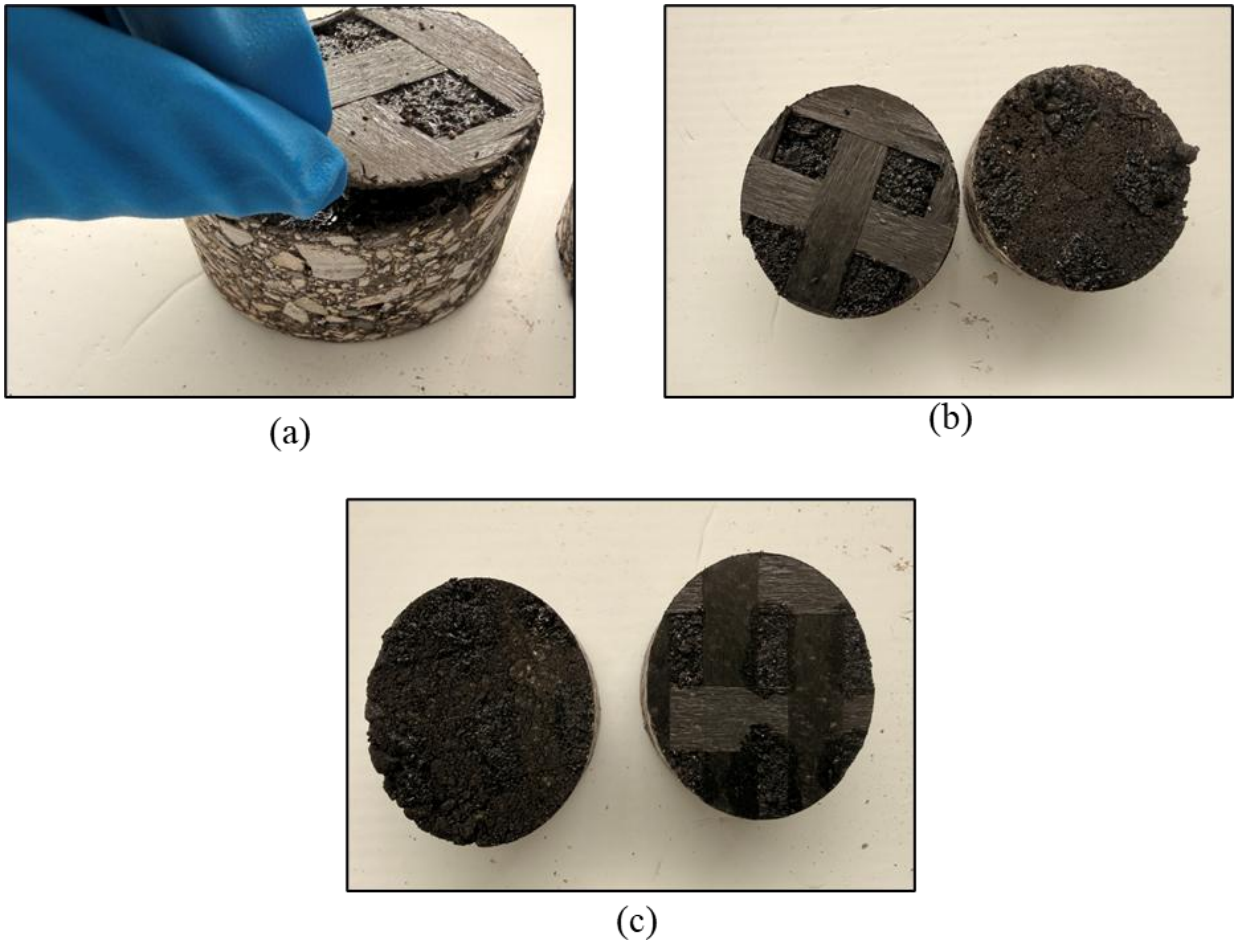

Figure 56: De-bonding of PETG 1X1 Lattice, (b) HDPE 1X1 Specimen After Failure, and (c) PETG 1X0.5 Specimen After Failure

This behavior suggested that the bonding and compaction between the top asphalt layer and the reinforcement system may not have been sufficient, resulting in weaker interfacial adhesion and premature interlayer failure. Poor compaction reduces aggregate interlock and intimate contact between layers, resulting in weaker interlayer bonding performance and reduced shear resistance [102]. In addition, vibrations generated during the coring process may have further weakened the

interfacial bonding between the top asphalt layer and the polymer lattice system, contributing to the reduced ISS performance observed in the slab specimens.

6.6 LISST Test Result of PCC-PC Slab Specimens

Figure 55 shows the influence of different polymer lattice opening sizes on the interlayer shear strength (ISS) performance of PCC-PC slab core specimens, where the error bars represent the corresponding standard deviations of the test results and the percentage values indicate the percent change in ISS relative to the control specimen.

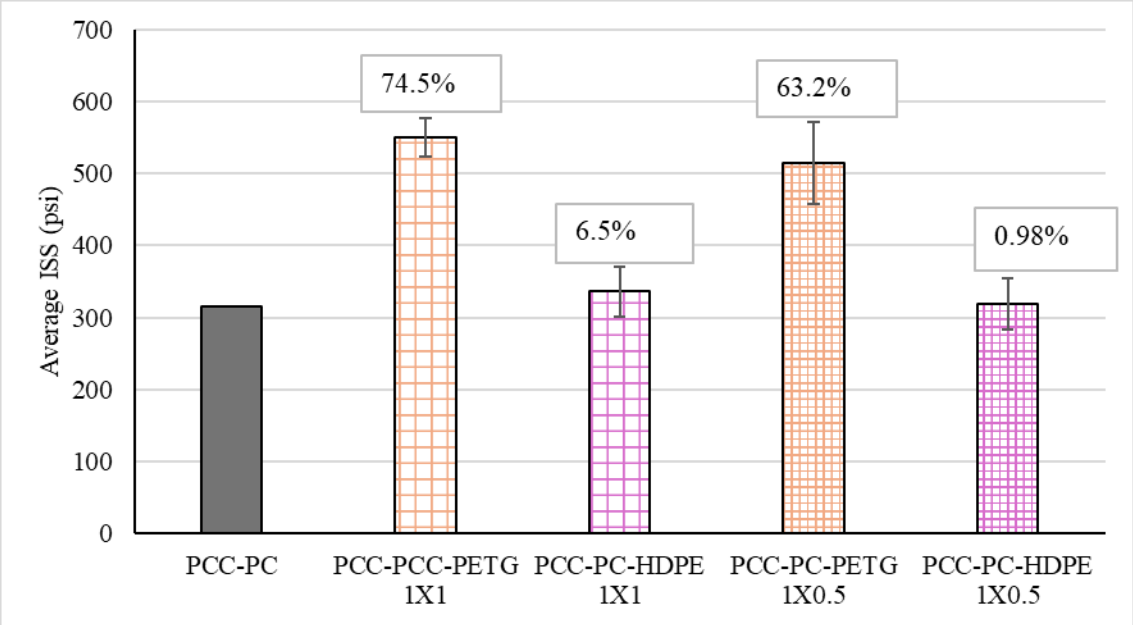

Figure 57: Effect of Polymer Type and Lattice Opening Size on Interlayer Shear Strength of PCC-PC Slab Specimens

Among the evaluated specimens, the PETG-1×1 configuration exhibited the highest average ISS value of 550.5 ± 27.22 psi, together with the lowest coefficient of variation (COV) of 4.94%, indicating both superior interlayer bonding performance and excellent consistency among the tested specimens. The PETG-1×0.5 specimens also demonstrated relatively high ISS values of

514.8 ± 57.29 psi; however, the higher COV value of 11.13% indicated greater variability in interfacial behavior.

The HDPE-1×1 specimens exhibited an average ISS value of 335.9 ± 34.02 psi with a COV of 10.13%. In contrast, the HDPE-1×0.5 specimens exhibited the lowest average ISS value of 318.5 ± 35.53 psi and a COV of 11.15%, indicating comparatively weaker and more variable interfacial bonding behavior among the evaluated systems.

Overall, the results indicated that both polymer type and lattice opening size significantly influenced the interlayer shear performance of PCC-PC slab specimens. For both PETG and HDPE systems, the 1×1 opening configuration consistently exhibited higher ISS values and lower variability compared to the 1×0.5 configuration. This behavior suggested that the larger lattice openings allowed improved polymer concrete penetration, enhanced mechanical interlocking, and more effective stress transfer across the reinforced interface.

Overall, the results indicated that both polymer type and lattice opening size significantly influenced interlayer shear performance. The 1×1 opening configuration consistently exhibited better performance and lower variability than the 1×0.5 configuration for both PETG and HDPE systems. This behavior suggested that the larger opening size allowed improved concrete mixture penetration, aggregate interlock, and stress transfer across the reinforced interface.

The load–displacement curves obtained from replicate specimens are presented in Figure 58. The PCC-PC specimens exhibited the largest displacement at failure, ranging from approximately 3.9 to 7.1 mm, indicating the greatest deformation capacity among the evaluated systems. The PCC-PC-PETG–1×1 specimens exhibited consistent responses, with failure occurring between approximately 1.9 and 2.3 mm. The PCC-PC-PETG-1×0.5 specimens exhibited greater variability, with failure displacements ranging from approximately 2.1 to 3.8 mm. Similar failure displacements were observed for the PCC-PC-HDPE–1×1 and PCC-PC-HDPE-1×0.5

specimens, which generally failed between approximately 1.8 and 2.4 mm. Overall, the replicate specimens exhibited similar load–displacement trends within each group, indicating reasonable repeatability of the test procedure.

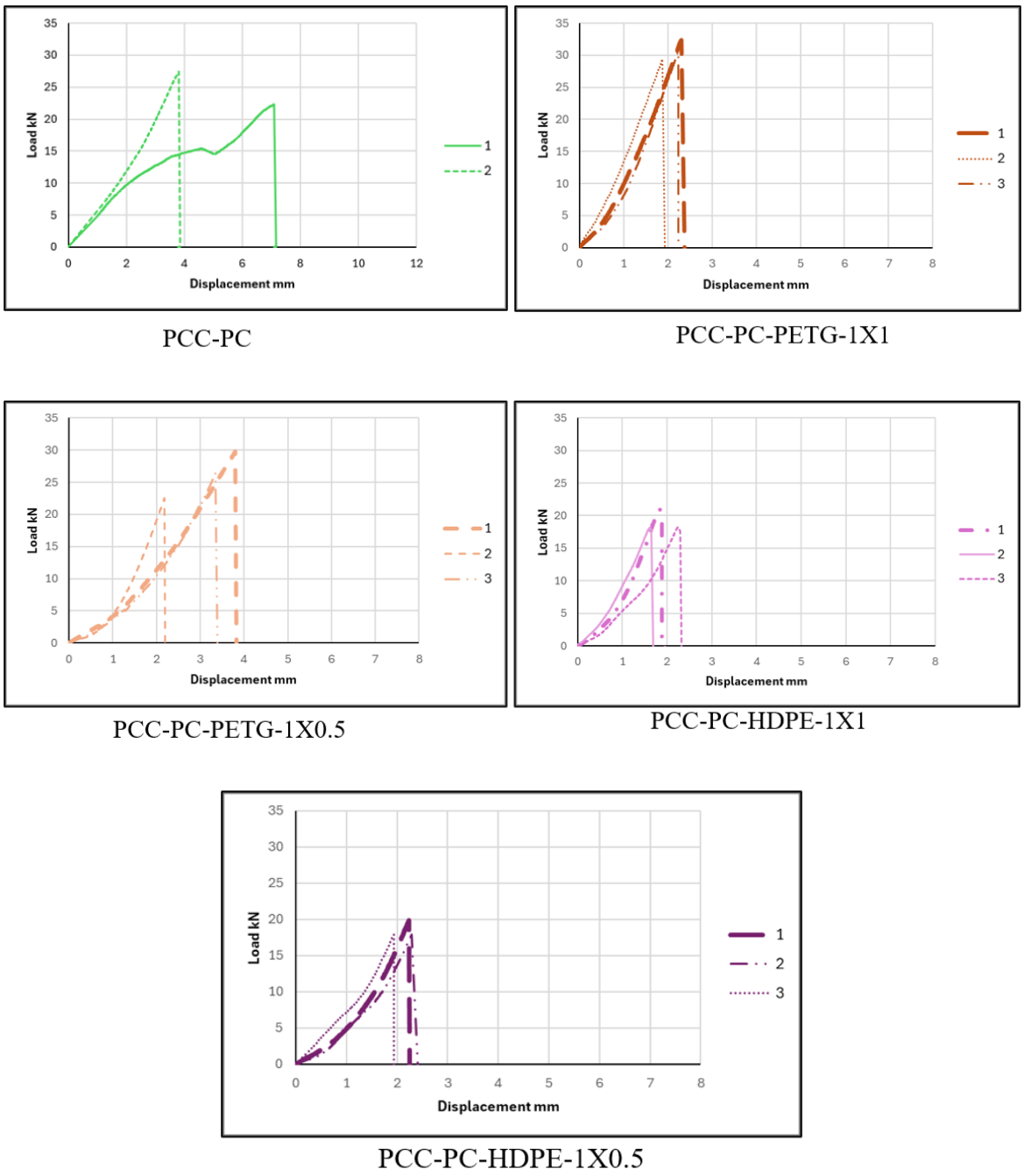

Figure 58:Comparison of Load–Displacement Responses Within Each Polymer Type and Lattice Opening Size

Figure 59 compares the representative load-displacement responses of the PCC-PC-CPETG and PCC-PC-GHDPE systems with different lattice opening sizes. For the CPETG system, the 1×1 lattice developed a peak load of 30.5 kN, compared to 27.5 kN for the 1×0.5 lattice, and exhibited a steeper load-displacement response, indicating greater stiffness. Similarly, the GHDPE-1×1 lattice developed a slightly higher peak load of 20.9 kN than the GHDPE–1×0.5 lattice, which reached 19.8 kN. However, the 1×0.5 lattices exhibited larger failure displacements, indicating greater deformation capacity. Overall, the 1×1 lattices exhibited higher stiffness and load-carrying capacity, whereas the 1×0.5 lattices exhibited greater deformation capacity.

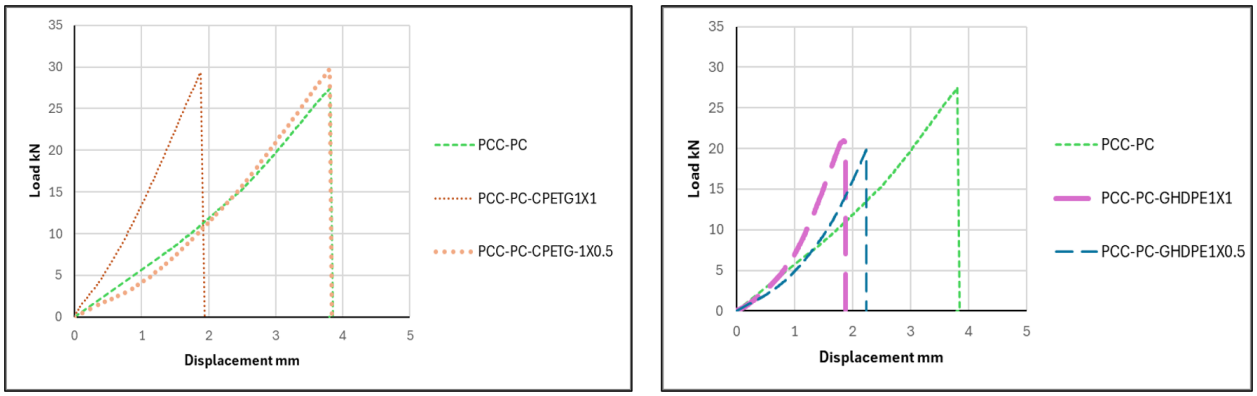

Figure 59: Effect of Lattice Opening Size on the Load–Displacement Response of PCC-PC-CPETG and PCC-PC-GHDPE Systems

Figure 60 compares the representative load–displacement responses of PCC-PC systems reinforced with CPETG and GHDPE lattices having identical opening sizes. For the 1×1 configuration, the PCC-PC-CPETG–1×1 specimen developed a peak load of 30.5 kN, compared to 20.9 kN for the PCC-PC-GHDPE–1×1 specimen. The CPETG-1×1 specimen also exhibited a steeper load–displacement response, indicating greater stiffness and resistance to deformation. A similar trend was observed for the 1×0.5 configuration, where the PCC-PC-CPETG–1×0.5 specimen developed a peak load of 27.5 kN, whereas the PCC-PC-GHDPE–1×0.5 specimen reached 19.8 kN Overall,

the CPETG lattices exhibited higher stiffness and load-carrying capacity than the corresponding GHDPE lattices for both opening sizes, indicating that polymer type significantly influenced the interfacial behavior of the PCC-PC system.

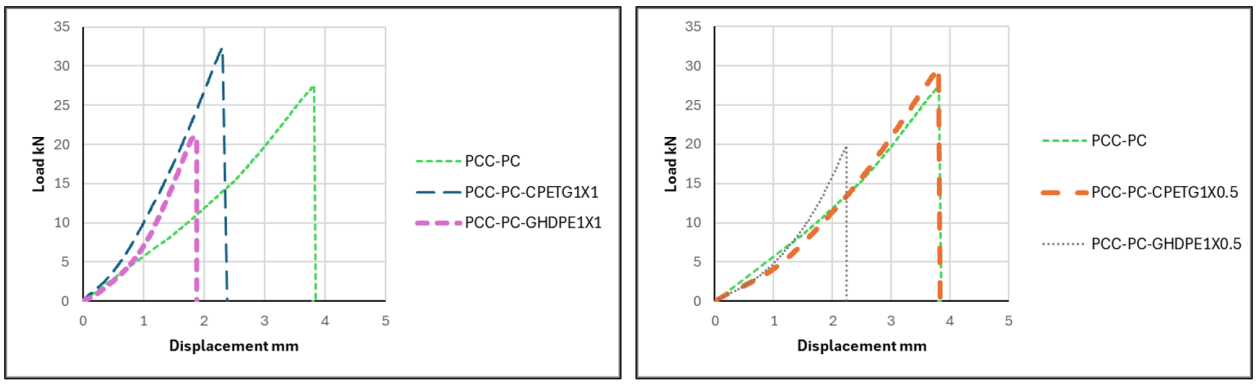

Figure 60: Effect of Polymer Type on the Load-Displacement Response of PCC-PC Systems with 1×1 and 1×0.5 Lattice Opening Sizes

Figure 61 summarizes the influence of thermoplastic FRP type and lattice geometry on the load-displacement response of the PCC-PC system. Distinct differences in stiffness, deformation behavior, and load-carrying capacity were observed among the evaluated systems. The CPETG-reinforced specimens generally exhibited steeper load–displacement responses and greater resistance to deformation than the corresponding GHDPE-reinforced specimens. In addition, the 1×1 lattice configurations exhibited stiffer responses than the corresponding 1×0.5 configurations. Overall, the results indicate that both polymer type and lattice geometry influenced the interlayer shear behavior of the PCC-PC system.

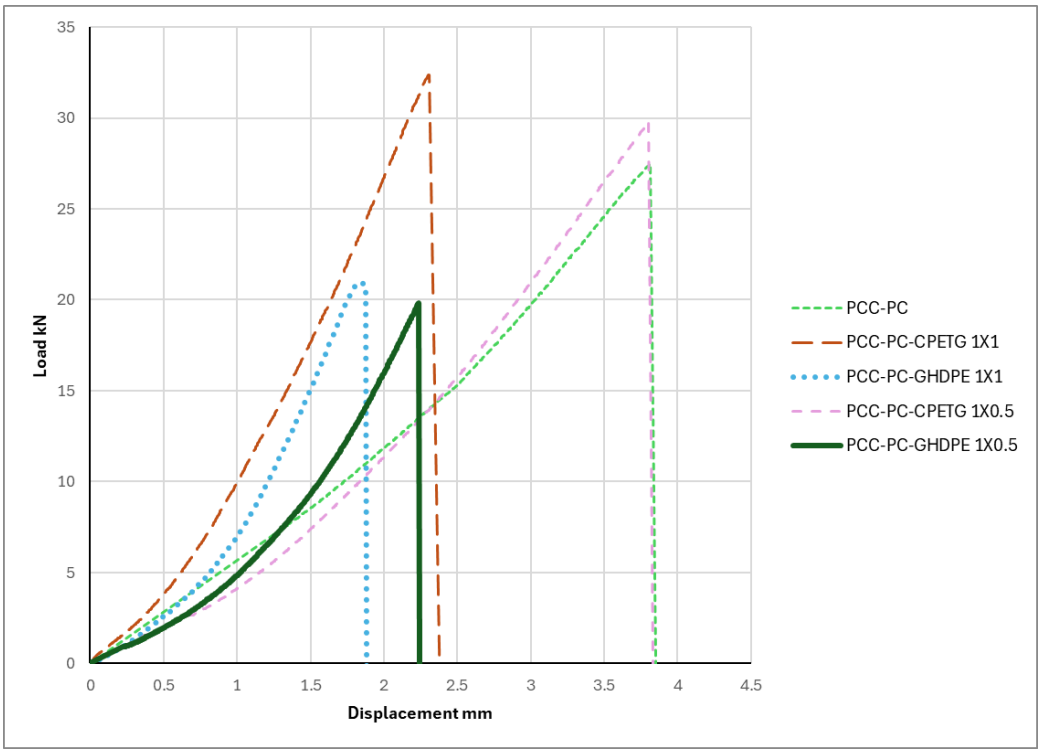

Figure 61: Effect of Thermoplastic FRP Type and Lattice Geometry on the Load–Displacement Response of PCC-PC Systems

To better understand the failure mechanisms responsible for the observed differences in interlayer shear performance, the post-failure conditions of the tested specimens were examined as presented in Figure 62. Examination of the failed specimens indicated that almost all specimens, except HDPE-1×0.5, exhibited crack propagation extending from the interlayer region into the PCC substrate, as shown in Figure 56 (d). The post-failure condition also indicated that the polymer lattice systems remained strongly attached to the polymer concrete overlay after testing, suggesting effective bonding and mechanical interaction between the reinforcement system and the overlay material.

Similar behavior was reported in a previous study involving thermoplastic CFRP reinforcement systems in polymer concrete, where improved load transfer was attributed to the ability of the polymer concrete matrix to penetrate around and beneath the reinforcement during

placement, thereby enhancing mechanical interlocking and anchorage within the surrounding matrix. The enhanced confinement was reported to contribute to improved stress transfer and crack resistance within the composite system [103].

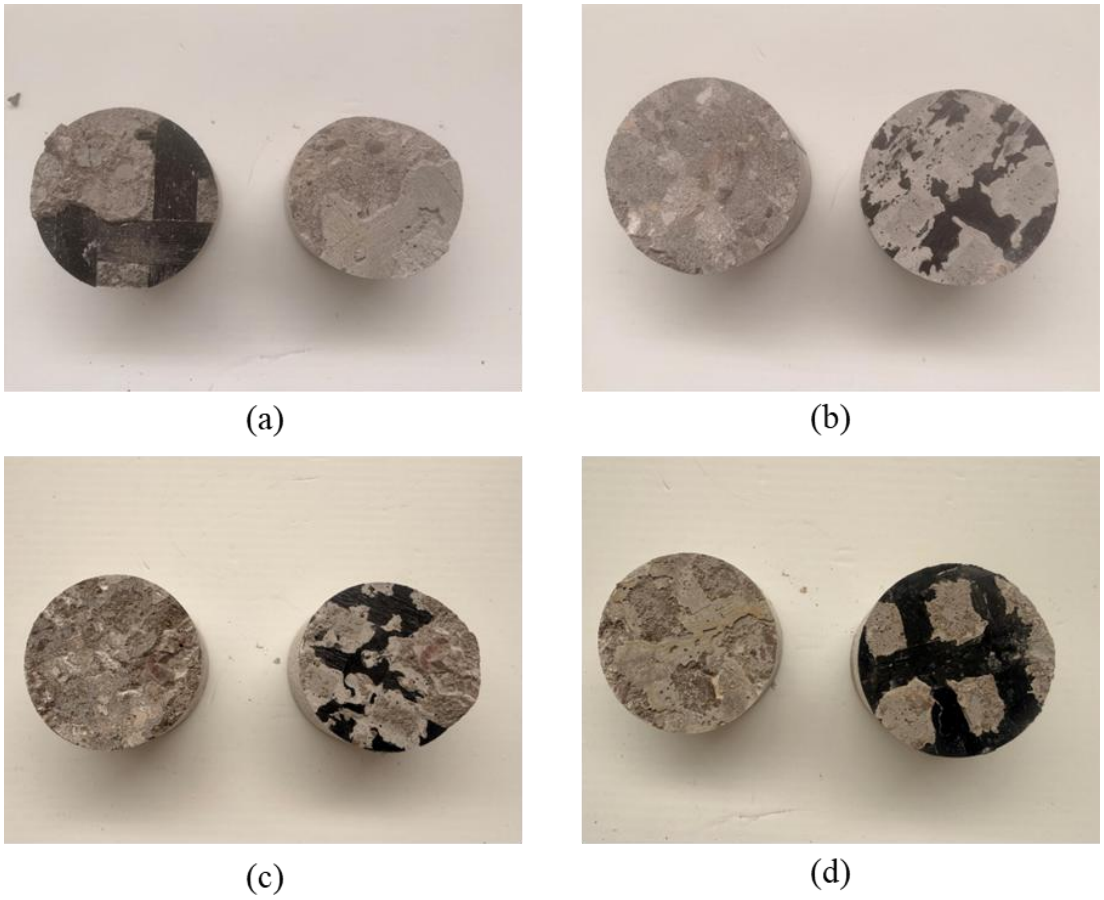

Figure 62: Post Failure Image of - (a) PETG 1×1, (b) PETG 1×0.5, (c) HDPE 1×1, and (d) HDPE 1×0.5

Chapter 07. Mechanics-Based Explanation of Interlayer Performance

The previous chapter presented the experimental interlayer shear strength (ISS) results and post-failure observations of different thermoplastic FRP reinforcement systems incorporated within asphalt-asphalt (A-A), Portland cement concrete-Portland cement concrete (PCC-PCC), and Portland cement concrete-polymer concrete (PCC-PC) systems. However, the measured ISS values alone cannot fully explain the governing mechanisms responsible for the observed interlayer behavior. Therefore, a mechanics-based interpretation was performed to explain the interaction between the thermoplastic reinforcement systems and the surrounding host materials.

7.1 A-A Systems

The asphalt-asphalt systems generally exhibited lower ISS values than the PCC-based systems because of the viscoelastic nature and lower stiffness of asphalt mixtures. Unlike cementitious systems, asphalt mixtures undergo significant localized deformation under shear loading. Consequently, larger interfacial shear strains and localized stress concentrations developed during the LISST test, promoting relative movement and premature de-bonding at the interface [104].

Under shear loading, stresses generated within the asphalt overlay were required to transfer through the tack coat and thermoplastic reinforcement into the underlying asphalt substrate. However, because asphalt mixtures possess relatively low stiffness and time-dependent deformation characteristics, stresses could not be uniformly distributed across the interface. Instead, stress concentration developed around reinforcement boundaries and within localized regions surrounding the lattice structure.

Among the evaluated asphalt systems, G-PETG exhibited the highest ISS values. This behavior may be associated with the comparatively higher stiffness and dimensional stability of PETG at room temperature relative to HDPE systems. PETG possesses a relatively high glass transition temperature (T_g), ranging from approximately 80°C to 82°C, whereas HDPE possesses a substantially lower T_g, ranging from approximately -100°C to -130°C [87, 89]. Since the testing temperature remained significantly below the T_g of PETG, the material remained in a comparatively rigid and glassy state during loading. Consequently, localized deformation within the interlayer region was reduced, allowing more effective stress transfer and improved confinement surrounding the reinforcement system. In contrast, the testing temperature remained substantially higher than the glass transition temperature (T_g) of HDPE. Under these conditions, HDPE generally exhibits increased ductility and greater deformation under loading because of increased molecular chain mobility within the polymer structure [71, 105]. Consequently, larger localized deformation likely developed within the HDPE reinforcement layer during shear loading, reducing confinement efficiency and promoting premature interfacial de-bonding.

The interaction between the tack coat and polymer surface also appeared to significantly influence the interfacial bonding behavior. Polyamide-based systems exhibited improved ISS values following tack coat application because the relatively higher surface energy of polyamides promoted improved wetting and adhesive interaction with the asphalt emulsion. Improved wetting likely increased contact between the tack coat and reinforcement surface, thereby improving resistance to shear-induced sliding [98, 99]. In contrast, lower-surface-energy polymers such as HDPE and polypropylene likely exhibited weaker adhesive interaction with the tack coat, causing the tack coat to behave more similarly to a lubricating layer rather than an effective bonding medium [71].

Fiber orientation also strongly influenced the stress transfer mechanism. Inclined fiber orientations generally produced higher ISS values than parallel and perpendicular orientations. When fibers were aligned at intermediate angles relative to the direction of shear loading, crack propagation and localized sliding were restrained across multiple directions simultaneously. Consequently, stresses could redistribute more gradually throughout the interface. In contrast, fibers aligned strictly parallel or perpendicular to the shear plane allowed more direct crack propagation paths and promoted localized stress concentration along the reinforcement boundaries.

The slab-scale asphalt specimens exhibited substantially lower ISS values than the pilot study specimens. This behavior was likely associated with heat loss during slab fabrication and insufficient confinement surrounding the lattice structure. During slab preparation, longer durations existed between asphalt placement and compaction because of the PMW kneading compactor process. As the asphalt mixture cooled, binder viscosity increased rapidly, reducing workability and limiting aggregate rearrangement around the lattice system. Consequently, inadequate aggregate interlock and incomplete embedment developed around the reinforcement structure, thereby weakening the interfacial bond.

The improved performance observed for the 1 × 1 lattice systems compared to the 1 × 0.5 systems may also be explained through aggregate interaction mechanisms. Larger openings allowed greater aggregate penetration through the lattice structure and improved aggregate interlock between the overlay and substrate layers. Consequently, stresses could transfer more effectively across the interface and distribute more uniformly throughout the surrounding asphalt matrix.

Overall, the asphalt systems were governed primarily by viscoelastic interfacial deformation, localized stress concentration, and adhesive de-bonding. The effectiveness of the thermoplastic reinforcement systems, therefore, depended strongly on the ability of the polymer to

maintain dimensional stability, resist localized deformation, and promote stress redistribution within the surrounding asphalt matrix.

7.2 PCC-PCC Systems

The PCC-PCC systems exhibited significantly higher ISS values than the asphalt systems because of the substantially higher stiffness and confinement provided by the cementitious matrix [48]. Unlike asphalt mixtures, Portland cement concrete undergoes relatively small deformation under loading, thereby reducing relative movement and localized sliding at the interface. The relatively high modulus of the PCC substrate likely reduced interfacial deformation during loading, thereby promoting more gradual stress distribution throughout the surrounding concrete matrix and reducing localized stress concentration near the interface [106].

Among the evaluated PCC-PCC systems, G-PP exhibited the highest ISS values and demonstrated crack propagation extending into the PCC substrate rather than along the interface. This behavior indicated that the interfacial bond strength exceeded the tensile resistance of the surrounding concrete. The transition from adhesive interfacial de-bonding to cohesive substrate cracking indicates a significant improvement in interfacial stress transfer capability [76].

The improved performance of the G-PP systems may be associated with the combined effect of glass-fiber reinforcement and the polypropylene matrix. The glass fibers likely improved crack-bridging capacity and stress transfer across the interface, while the polypropylene matrix may have allowed greater strain accommodation compared to stiffer carbon-fiber-reinforced systems [76]. Consequently, localized stress concentration near the interface may have been reduced, thereby promoting more gradual stress redistribution within the surrounding cementitious matrix.

In contrast, the C-PA6 systems exhibited lower ISS values and partial interlayer de-bonding after failure. Although carbon fiber reinforcement possesses relatively high stiffness, excessive stiffness mismatch between the reinforcement and the surrounding concrete matrix may have promoted localized stress concentration near the interface [72]. Once localized cracking initiated near these regions, rapid crack propagation likely occurred because stresses could not redistribute effectively throughout the surrounding matrix.

The PCC-PCC systems further demonstrated that modulus compatibility between the reinforcement system and the surrounding host material strongly influences interfacial behavior. Reinforcement systems capable of redistributing stresses gradually and reducing localized strain concentration, delayed crack initiation, and improved overall interfacial performance.

Overall, the PCC-PCC systems exhibited improved confinement, reduced interfacial deformation, and more stable stress redistribution than the asphalt systems because of the relatively high stiffness and brittle fracture behavior of the cementitious matrix.

7.3 PCC-PC Systems

The PCC-PC systems exhibited the highest overall interlayer performance among all evaluated systems. This behavior was primarily associated with enhanced mechanical interlocking, improved confinement, and more efficient stress redistribution within the polymer concrete overlay system. Unlike asphalt mixtures, polymer concrete possesses substantially higher stiffness and lower viscoelastic deformation under loading, allowing the reinforced interface to resist relative displacement more effectively [104, 107].

Under shear loading, stresses generated within the polymer concrete overlay were transferred through the reinforcement system into the underlying PCC substrate. In conventional interfaces, stress transfer is governed primarily by adhesive bonding and frictional resistance at the

interface. However, once thermoplastic lattice systems were incorporated within the PCC-PC interface, the governing load transfer mechanism appeared to transition from simple adhesive bonding to a combined anchorage-confinement mechanism.

Among all evaluated configurations, the PETG-based systems demonstrated the highest ISS values and exhibited crack propagation primarily within the PCC substrate rather than along the interface. This behavior indicated that the reinforced interface no longer represented the weakest plane within the composite system. Instead, stresses were redistributed into the surrounding substrate until cohesive cracking developed within the PCC itself. This shift from adhesive interfacial failure to cohesive substrate cracking indicated that the interface developed sufficient stress transfer capability to exceed the tensile resistance of the surrounding substrate material [107].

The superior performance of the PETG systems may be associated with multiple interacting mechanisms related to stiffness compatibility, thermomechanical behavior, and interfacial confinement due to having a large T_g value [1]. In contrast, the testing temperature remained substantially higher than the T_g of HDPE, causing the HDPE systems to behave in a more ductile and deformable manner during loading. Increased localized yielding within the HDPE layer likely reduced confinement efficiency and promoted stress concentration near the interface [103].

The polymer concrete overlay also likely penetrated around and beneath the PETG lattice openings during casting. As curing progressed, the reinforcement became mechanically embedded within the hardened polymer concrete matrix. Consequently, the interface developed a three-dimensional mechanical anchorage mechanism rather than a purely planar adhesive bond. Similar embedment and anchorage behavior has previously been reported in FRP-reinforced cementitious systems, where penetration of the surrounding matrix around the reinforcement geometry improved confinement and increased resistance to interfacial crack propagation [87].

The improved confinement surrounding the PETG systems also likely altered the fracture behavior of the interface. In unreinforced systems, crack initiation generally occurs at localized stress concentration regions near the interface, after which rapid crack propagation produces complete interfacial de-bonding. However, in the reinforced PCC-PC systems, stresses were redistributed around the embedded lattice structure and transferred deeper into the surrounding PCC substrate.

The post-failure observations strongly supported this mechanism. In many PETG-reinforced specimens, the lattice remained strongly attached to the polymer concrete overlay while cracking propagated into the PCC substrate itself. This behavior suggested that the reinforcement system effectively arrested or redirected interfacial crack propagation and forced failure into the surrounding substrate material.

The influence of lattice geometry also appeared to significantly affect the stress transfer mechanism. The larger 1 × 1 lattice systems generally exhibited better overall performance than the denser 1 × 0.5 systems. Larger openings likely allowed improved polymer concrete penetration and enhanced aggregate interlock through the lattice structure. Consequently, stresses could distribute more gradually throughout the surrounding matrix rather than concentrating around closely spaced reinforcement boundaries.

In contrast, the smaller 1 × 0.5 openings increased the proportion of reinforcement material occupying the interface, potentially increasing localized stiffness mismatch and stress concentration near reinforcement boundaries. Once cracking initiated within these constrained regions, rapid localized crack propagation likely occurred despite the relatively high peak ISS values.

7.4 Comparison of Governing Failure Mechanism

The governing interlayer behavior varied significantly depending on the host material system and reinforcement type.

In the asphalt systems, the relatively low stiffness and viscoelastic behavior of asphalt mixtures promoted localized deformation and interfacial sliding. Consequently, adhesive interfacial de-bonding remained the dominant failure mechanism.

In the PCC-PCC systems, the higher stiffness of concrete improved confinement and reduced relative interfacial movement. Reinforcement systems capable of improving stress redistribution shifted failure from the interface into the surrounding concrete substrate.

The PCC-PC systems exhibited the strongest overall interlayer performance because of the combined effects of polymer concrete penetration, enhanced confinement, crack-bridging behavior, and mechanical anchorage surrounding the reinforcement system. In several cases, the reinforced interface became stronger than the PCC substrate itself, resulting in cohesive substrate cracking rather than interfacial de-bonding. A schematic showing the mechanism is given below in Figure 63.

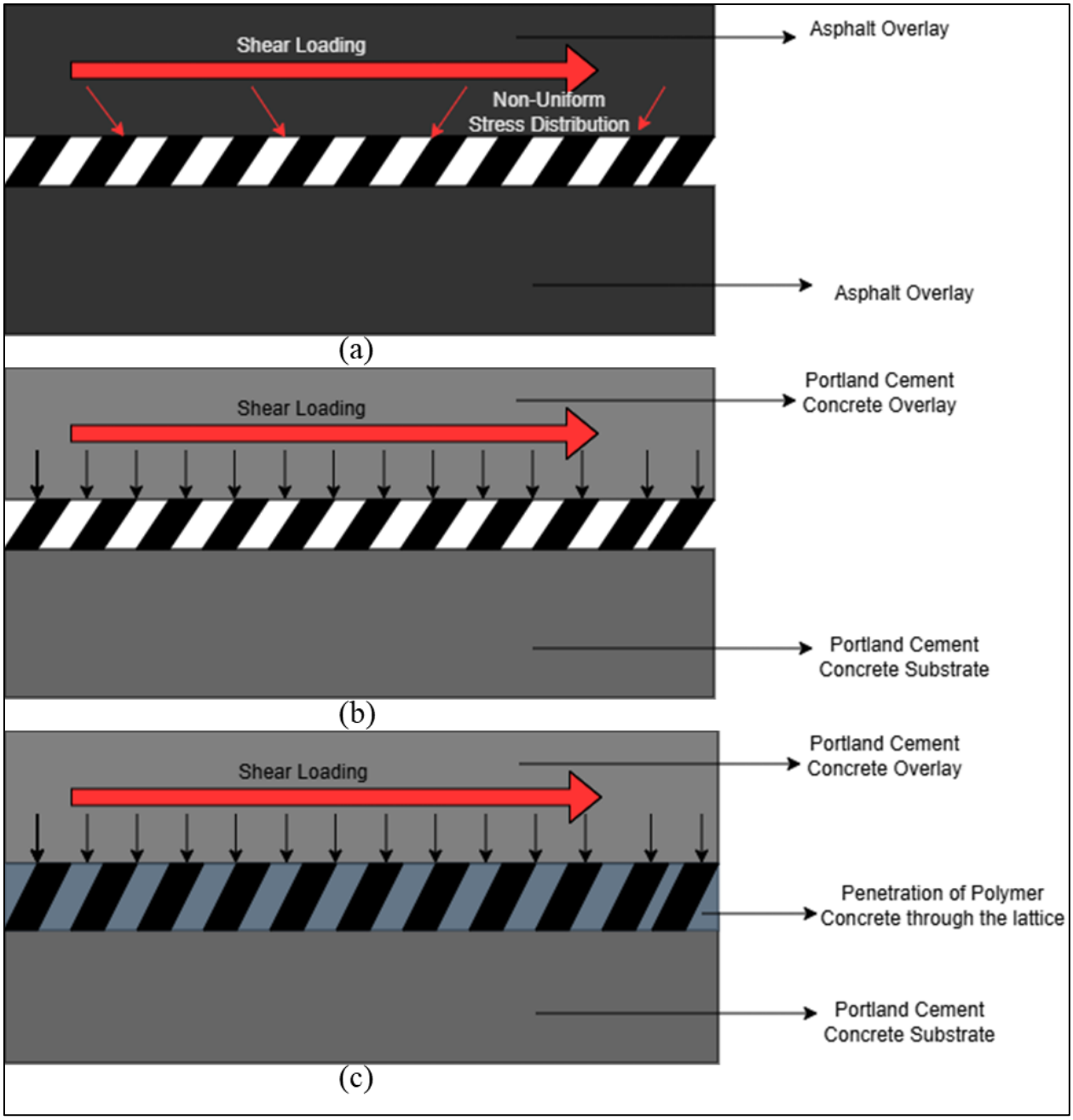

Figure 63: Schematic Showing the Difference in the Failure Mechanism of (a) A-A, (b)PCC-PCC, and (c) PCC-PC

Overall, the results demonstrated that interlayer performance was governed not only by the mechanical properties of the reinforcement system but also by the interaction between the thermoplastic material and the surrounding host matrix, the ability to redistribute stresses away

from localized crack initiation regions, and the effectiveness of confinement surrounding the reinforcement structure.

Chapter 08. Conclusions

This study evaluated the influence of different thermoplastic FRP tapes and polymer lattice systems on the interlayer shear strength (ISS) performance of asphalt-asphalt (A-A), Portland cement concrete-Portland cement concrete (PCC-PCC), and Portland cement concrete-polymer concrete (PCC-PC) composite systems using the Louisiana Interlayer Shear Strength Test (LISST). The effects of polymer type, tack coat application, heating condition, fiber orientation, and lattice opening size were investigated to understand their influence on interlayer bonding behavior and failure mechanisms.

For the asphalt pilot study specimens, polymer type was found to significantly influence ISS performance. Among all evaluated tapes, G-PETG exhibited the highest ISS values, indicating improved interlayer bonding and stress transfer capability. In contrast, G-HDPE exhibited the lowest ISS performance because of its lower stiffness and premature interfacial deformation. Tack coat application improved the performance of the polyamide-based systems but reduced the performance of some glass fiber-reinforced systems because of weaker adhesive interaction and slippage at the interface. Inclined fiber orientation generally produced higher ISS values than parallel and perpendicular orientations, suggesting improved crack resistance and stress redistribution across the interface. Localized heating of G-HDPE tapes negatively affected interlayer bonding and resulted in significant reductions in ISS.

For the PCC-PCC specimens, polymer type also had a substantial influence on interlayer bonding performance. Among all tested configurations, PCC-GPP exhibited the highest ISS values and demonstrated crack propagation into the PCC substrate rather than failure at the interface. This behavior indicated that the interlayer bond strength exceeded the tensile resistance of the concrete

substrate. In contrast, PCC-CPA6 and PCC-GPETG exhibited reduced ISS values compared to the control specimens, while PCC-CPA410 demonstrated only moderate improvement.

For the PCC-PC specimens, C-GPETG exhibited the highest ISS performance among all tested configurations. Post-failure observations indicated that the G-PETG tape became strongly embedded within the polymer concrete overlay, resulting in crack propagation primarily within the PCC substrate rather than along the reinforced interface. This behavior suggested improved mechanical anchorage and stress transfer between the reinforcement system and the overlay material. In contrast, C-CPA6 and C-PA410 specimens primarily failed at the interlayer, indicating weaker bonding performance.

For the slab specimens, both polymer type and lattice opening size significantly influenced ISS performance. The 1 × 1 opening configuration consistently exhibited higher ISS values and lower variability than the 1 × 0.5 configuration for both PETG and HDPE systems. In the asphalt slab specimens, HDPE-1 × 1 exhibited the highest ISS among the reinforced configurations, while PETG-1 × 0.5 exhibited the lowest performance. The reduced ISS observed in the asphalt slab specimens was likely influenced by heat loss during slab fabrication, reduced mixture workability, insufficient compaction around the polymer lattice, and vibration effects during coring. In the PCC-PC slab specimens, PETG-based systems exhibited superior interlayer bonding performance compared to HDPE-based systems. PETG-1 × 1 exhibited the highest ISS values together with the lowest variability among all tested slab configurations. Post-failure observations further indicated that the polymer lattices remained strongly attached to the polymer concrete overlay, suggesting effective mechanical interlocking and confinement within the overlay system.

Overall, the results demonstrated that thermoplastic FRP systems can significantly influence interlayer bonding behavior depending on polymer type, lattice geometry, fiber orientation, and fabrication conditions. Among the evaluated systems, G-PETG demonstrated the

best overall performance in the asphalt pilot study specimens, G-PP exhibited the best performance in PCC-PCC specimens, and PETG-based lattice systems demonstrated superior performance in PCC-PC slab specimens.

The findings of this study indicate that thermoplastic FRP reinforcements have strong potential for use in bridge deck overlay systems and multilayer pavement applications where improved interlayer bonding and enhanced durability are required.

Chapter 09. Limitations and Recommendations for Future Work

9.1 Limitations

Several limitations were identified during the experimental investigation. In the asphalt slab specimens, limited tack coat absorption was observed around the polymer lattice systems, which may have reduced interfacial adhesion and stress transfer efficiency. In addition, the slab compaction process exhibited non-uniformity and excessive heat loss during fabrication. Reduced asphalt workability during compaction may therefore have contributed to lower interlayer shear strength and incomplete confinement surrounding the reinforcement systems.

The moderate variability observed in the concrete slab specimens may also have been associated with slight geometric inconsistencies during the coring process. Although efforts were made to extract cores from regions with similar lattice geometry, minor variations in reinforcement positioning and opening distribution may still have influenced the measured interlayer behavior.

Furthermore, only two lattice opening configurations (1×1 and 1×0.5) were evaluated in this study. Therefore, the influence of larger opening geometries and additional reinforcement configurations on interlayer stress transfer behavior could not be fully assessed.

9.2 Recommendations for Future Work

Future studies should further investigate the influence of fiber type, lattice geometry, tack coat application, and fabrication procedures on interlayer bonding performance and failure behavior. In the asphalt pilot study, G-PETG exhibited superior interlayer performance compared to the lattice-based C-PETG system incorporated within the slab specimens. Therefore, future investigations may evaluate lattice systems fabricated using G-PETG to determine whether

improved bonding performance and stress redistribution can be achieved in asphalt slab applications.

Different tack coat application rates should also be investigated to evaluate their influence on tack coat absorption, adhesive interaction, and interfacial shear resistance surrounding the lattice systems. Since limited tack coat penetration was observed around some reinforcement systems, optimization of tack coat application procedures may improve bonding efficiency and stress transfer across the interface.

Future studies may additionally evaluate the influence of fiber fraction within the reinforcement systems. Variations in fiber density may improve tack coat absorption, aggregate interaction, and matrix penetration surrounding the lattice structure, thereby potentially improving confinement and reducing localized stress concentration near the interface.

Improved slab fabrication and compaction procedures should also be developed to minimize heat loss during asphalt slab preparation. Enhanced temperature control and improved compaction uniformity may improve asphalt workability, reinforcement embedment, and overall interlayer bonding performance.

Since both asphalt and concrete slab specimens generally exhibited improved performance with the 1×1 opening configuration compared to the 1×0.5 configuration, future studies should investigate larger lattice opening sizes and additional reinforcement geometries to evaluate their influence on stress redistribution, crack propagation resistance, and interlayer shear strength performance.

Chapter 010. References

1. Teng, L. and K.H. Khayat, *Effect of overlay thickness, fiber volume, and shrinkage mitigation on flexural behavior of thin bonded ultra-high-performance concrete overlay slab.* Cement and Concrete Composites, 2022. **134**: p. 104752.
2. Du, J., et al., *Highly thixotropic ultra-high-performance concrete (UHPC) as an overlay.* Construction and Building Materials, 2023. **366**: p. 130130.
3. Rambabu, D., et al., *A review of application of UHPFRC in bridges as an overlay.* Innovative Infrastructure Solutions, 2023. **8**(1): p. 57.
4. Al-Rousan, R.Z. and R.A. Bara'a. *The influence of prestress level on the behavior of prefabricated precast concrete bridge deck panel systems with different overlay thicknesses*. in *Structures*. 2023. Elsevier.
5. Krauss, P.D., J.S. Lawler, and K.A. Steiner, *Guidelines for selection of bridge deck overlays, sealers and treatments.* NCHRP Project, 2009: p. 20-07.
6. Nian, T., et al., *Method to predict the interlayer shear strength of asphalt pavement based on improved back propagation neural network.* Construction and Building Materials, 2022. **351**: p. 128969.
7. Nian, T., et al., *Mechanical response of interlayer structural shear performance of asphalt pavement with functional layer considering interlayer contact state.* Case Studies in Construction Materials, 2023. **18**: p. e01934.
8. Collop, A.C., N.H. Thom, and C. Sangiorgi, *Assessment of bond condition using the Leutner shear test.* Proceedings of the Institution of Civil Engineers - Transport, 2003. **156**(4): p. 211-217.

9. Shahin, M.Y., et al., *Effect of layer slippage on performance of asphalt-concrete pavements*. 1986.

10. Leischner, S., et al., *Mechanical testing and modeling of interlayer bonding in HMA pavements.* Transportation Research Record, 2019. **2673**(11): p. 879-890.

11. Ktari, R., et al., *Pavement interface damage behavior in tension monotonic loading.* Construction and Building Materials, 2016. **106**: p. 430-442.

12. Kumar, V.V. and S. Saride, *Evaluation of cracking resistance potential of geosynthetic reinforced asphalt overlays using direct tensile strength test.* Construction and Building Materials, 2018. **162**: p. 37-47.

13. Wang, J., et al., *Application of tack coat in pavement engineering.* Construction and Building Materials, 2017. **152**: p. 856-871.

14. Yang, K. and R. Li, *Characterization of bonding property in asphalt pavement interlayer: A review.* Journal of Traffic and Transportation Engineering (english edition), 2021. **8**(3): p. 374-387.

15. Xing, C., et al., *A comprehensive review on the blending condition between virgin and RAP asphalt binders in hot recycled asphalt mixtures: Mechanisms, evaluation methods, and influencing factors.* Journal of Cleaner Production, 2023. **398**: p. 136515.

16. Lytton, R.L., et al., *Models for predicting reflection cracking of hot-mix asphalt overlays*. 2010.

17. Baek, J., et al., *Effects of Interface Conditions on Reflective Cracking Development in Hot-Mix Asphalt Overlays.* Road Materials and Pavement Design, 2010. **11**(2): p. 307-334.

18. Ozer, H., et al., *Characterisation of interface bonding between hot-mix asphalt overlay and concrete pavements: modelling andin-situresponse to accelerated loading.* International Journal of Pavement Engineering, 2012. **13**(2): p. 181-196.

19. Attanayake, U. and A.F. Mazumder, *Performance-based approach for deciding the age of new concrete for thin epoxy overlay application.* Transportation Research Record, 2021. **2675**(10): p. 1055-1068.

20. Mazumder, A.F., H. Amunugama, and U. Attanayake, *Impact of concrete mix ingredients and surface treatments on epoxy overlay performance.* Transportation Research Record, 2021. **2675**(10): p. 1161-1173.

21. Mazumder, A.F., U. Attanayake, and N.S. Berke, *Performance of two thin epoxy overlays on new concrete under laboratory and outdoor exposure conditions.* Transportation Research Record, 2021. **2675**(10): p. 1406-1419.

22. Al-Rousan, R.Z. and B.A.R. Alnemrawi, *Interface Shear Strength Prediction of CFRP-Strengthened Sulfate-Damaged Shear Keys Using NLFEA.* International Journal of Civil Engineering, 2023. **21**(8): p. 1385-1402.

23. Vanelstraete, A. and L. Franken, *Prevention-of-reflective-cracking-in-pavements (RILEM TC 157 PRC report).* 1997.

24. 348, C.A., *Reinforcement of Pavements with Steel Meshes and Geosynthetics (REIPAS)*. (2006), Cost Action: Final report. COST, Brussels, Belgium.

25. Nguyen, M.-L., et al., *Review of glass fibre grid use for pavement reinforcement and APT experiments at IFSTTAR.* Road Materials and Pavement Design, 2013. **14**(sup1): p. 287-308.

26. Beer, F.P., et al., *3 Torsion.* 2002.

27. Raab, C. and M.N. Partl. *Interlayer shear performance: experience with different pavement structures*. in *PROCEEDINGS OF THE 3RD EURASPHALT AND EUROBITUME CONGRESS HELD VIENNA, MAY 2004*. 2004.

28. Romanoschi, S.A., *Characterization of pavement layer interfaces*. 1999: Louisiana State University and Agricultural & Mechanical College.

29. Canestrari, F., et al., *Advanced testing and characterization of interlayer shear resistance.* Transportation Research Record, 2005. **1929**(1): p. 69-78.

30. Mohammad, L.N., M. Raqib, and B. Huang, *Influence of asphalt tack coat materials on interface shear strength.* Transportation Research Record, 2002. **1789**(1): p. 56-65.

31. Diakhaté, M., et al., *Experimental investigation of tack coat fatigue performance: Towards an improved lifetime assessment of pavement structure interfaces.* Construction and Building Materials, 2011. **25**(2): p. 1123-1133.

32. Correia, N.d.S., *Performance of flexible pavements enhanced using geogrid-reinforced asphalt overlays.* PhD Tesis), São Carlos School of Engineering, São Paulo, Brazil, 2014.

33. Kampf, L., *Repair of concrete bridge pavements.* 1968.

34. Interactive, P. *Slippage Cracking*. Available from: https://pavementinteractive.org/reference-desk/pavement-management/pavement-distresses/slippage-cracking.

35. Kumari, M., P. Gupta, and S.S. Deshwal, *Integrated Life Cycle Cost Comparison and Environment Impact Analysis of the Concrete and Asphalt Roads.* Materials Today: Proceedings, 2022. **60**: p. 345-350.

36. McConnell, W., *EPOXY SURFACE TREATMENTS FOR PORTLAND-CEMENT CONCRETE PAVEMENTS.* 1968.

37. Rooney, H., *Epoxies in concrete construction and maintenance.* Special Publication, 1968. **21**: p. 5-8.

38. Whitesides, G., *Stresses in epoxy compounds for portland cement concrete.* Special Publication, 1968. **21**: p. 93-106.

39. Ghabchi, R., M.M. Zaman, and S. Rani, *Development Of Guidelines For Selection And Evaluation Of Tack Coats In Oklahoma*. 2018, Oklahoma. Department of Transportation.

40. Centre, C.K.i.P., *Glass Transition Temperature (Tg)-A210*. April 24,2021.

41. Haber, Z.B., et al., *Bond characterization of UHPC overlays for concrete bridge decks: Laboratory and field testing.* Construction and Building Materials, 2018. **190**: p. 1056-1068.

42. Bajaber, M. and I. Hakeem, *UHPC evolution, development, and utilization in construction: A review.* Journal of Materials Research and Technology, 2021. **10**: p. 1058-1074.

43. Santos, P.M.D. and E.N.B.S. Júlio, *Factors affecting bond between new and old concrete.* ACI Materials Journal, 2011. **108**(4): p. 449.

44. Momayez, A., et al., *Comparison of methods for evaluating bond strength between concrete substrate and repair materials.* Cement and Concrete Research, 2005. **35**(4): p. 748-757.

45. Silfwerbrand, J. and H. Beushausen. *Bonded concrete overlays: bond strength issues*. in *International Conference on Concrete Repair, Rehabilitation and Retrofitting. Cape Town, South Africa, November 21-23*. 2005.

46. Roberts, F.L., et al., *Hot mix asphalt materials, mixture design and construction.* 1996.

47. Huber, G. and G. Heiman, *Effect of asphalt concrete parameters on rutting performance: a field investigation.* 1986.

48. Huang, Y.H., *Pavement analysis and design*. Vol. 2. 2004: Pearson/Prentice Hall Upper Saddle River, NJ.

49. Advanced Asphalt Technologies, L., *A manual for design of hot mix asphalt with commentary*. Vol. 673. 2011: Transportation Research Board.

50. Fowler, D.W., *Polymers in concrete: a vision for the 21st century.* Cement and concrete composites, 1999. **21**(5-6): p. 449-452.

51. Vipulanandan, C. and E. Paul, *Characterization of polyester polymer and polymer concrete.* Journal of Materials in Civil Engineering, 1993. **5**(1): p. 62-82.

52. Stevens, R.J., et al., *Field evaluation of polyester-polymer concrete overlays on bridge decks using nondestructive testing.* Journal of Materials in Civil Engineering, 2021. **33**(7): p. 04021155.

53. Tashman, L., et al., *Evaluation of construction practices that influence the bond strength at the interface between pavement layers.* Journal of Performance of Constructed Facilities, 2008. **22**(3): p. 154-161.

54. Kong, L., et al., *Microscale mechanism and key factors of waterborne epoxy resin emulsified asphalt enhancing interlayer bonding performance and shear resistance of bridge deck pavement.* Construction and Building Materials, 2024. **419**: p. 135570.

55. Song, W., et al., *Preparation and performance characterization of waterborne epoxy resin modified asphalt emulsion for tack coat.* Journal of Cleaner Production, 2024. **475**: p. 143715.

56. Shafabakhsh, G. and S. Ahmadi, *Laboratory investigation of modified bitumen for interlayer in rigid–flexible composite pavement.* Journal of Thermoplastic Composite Materials, 2022. **35**(11): p. 1866-1888.

57. Fu, H., et al., *Design Optimization and Performance Evaluation of the Open-Graded Friction Course with Small Particle Size Aggregate.* Advances in Civil Engineering, 2021. **2021**(1): p. 1-11.

58. Pei, Z., et al., *DEM analysis of the evolution of reflection cracks in old cement concrete pavement with an ATB layer.* International Journal of Pavement Engineering, 2023. **24**(2): p. 1-10.

59. Kim, Y.K., M. Rith, and S.W. Lee, *Bond Strength Recovery of Tack Coat between Asphalt Concrete Surface and Roller-Compacted Concrete Base in Composite Pavements.* KSCE Journal of Civil Engineering, 2021. **25**(10): p. 3750-3757.

60. Hu, X., et al., *Effect of tack coat dosage and temperature on the interface shear properties of asphalt layers bonded with emulsified asphalt binders.* Construction and Building Materials, 2017. **141**: p. 86-93.

61. Yaacob, H., et al., *Curing of Asphalt Emulsified Tack Coat Subjected to Malaysian Weather Conditions.* Journal of Materials in Civil Engineering, 2015. **27**(4): p. 04014147.

62. Uzan, J., M. Livneh, and Y. Eshed. *Investigation of adhesion properties between asphaltic-concrete layers*. in *Association of Asphalt Paving Technologists Proc*. 1978.

63. Chen, J.-S. and C.-C. Huang, *Effect of surface characteristics on bonding properties of bituminous tack coat.* Transportation research record, 2010. **2180**(1): p. 142-149.

64. Lee, S.J., *Mechanical performance and crack retardation study of a fiberglass-grid-reinforced asphalt concrete system.* Canadian Journal of Civil Engineering, 2008. **35**(10): p. 1042-1049.

65. Ahmad, A.S., *Bridge preservation guide: Maintaining a state of good repair using cost effective investment strategies*. 2011, United States. Federal Highway Administration.

66. Chen, J.-S., C.K. Ober, and M.D. Poliks, *Characterization of thermally reworkable thermosets: materials for environmentally friendly processing and reuse.* Polymer, 2002. **43**(1): p. 131-139.

67. Hollaway, L., *A review of the present and future utilisation of FRP composites in the civil infrastructure with reference to their important in-service properties.* Construction and building materials, 2010. **24**(12): p. 2419-2445.

68. Bank, L.C., *Composites for construction: Structural design with FRP materials*. 2006: John Wiley & Sons.

69. Teng, J.-G., et al., *FRP: strengthened RC structures*. 2002.

70. Haibe, A.A., *Investigation of flexural behavior of reinforced concrete with 3D printed glass fiber reinforced polymer.* 2022.

71. Osswald, T.A. and G. Menges, *Materials science of polymers for engineers*. 2012: Carl Hanser Verlag GmbH Co KG.

72. Rousakis, T., *Retrofitting and strengthening of contemporary structures: materials used.* Encyclopedia of earthquake engineering, 2021: p. 1-15.

73. Karbhari, V.M., *Rehabilitation of Metallic Civil Infrastructure Using Fiber Reinforced Polymer (FRP) Composites: Types Properties and Testing Methods*. 2014: Elsevier.

74. Bakis, C.E., et al., *Fiber-reinforced polymer composites for construction—State-of-the-art review.* Journal of composites for construction, 2002. **6**(2): p. 73-87.

75. Wrightson, I., *Communicating Chemistry (2019w209)*. 2019.

76. J.G. Teng, J.-F.C., Scott Thomas Smith,Lik Lam, *FRP-strengthened RC structures.* Proceedings of the Institution of Civil Engineers - Structures and Buildings, 2003. **156**(1).

77. Hollaway, L.C. and J.-G. Teng, *Strengthening and rehabilitation of civil infrastructures using fibre-reinforced polymer (FRP) composites*. 2008: Elsevier.

78. Karsli, N.G. and A. Aytac, *Effects of maleated polypropylene on the morphology, thermal and mechanical properties of short carbon fiber reinforced polypropylene composites.* Materials & Design, 2011. **32**(7): p. 4069-4073.

79. NETZSCH, *PA6.6: Polyamide 6.6*.

80. Envalior, *PA410-EcoPaXX*®. Envalior.

81. Leszczyńska, A., P. Kiciliński, and K. Pielichowski, *Biocomposites of polyamide 4.10 and surface modified microfibrillated cellulose (MFC): influence of processing parameters on structure and thermomechanical properties.* Cellulose, 2015. **22**(4): p. 2551-2569.

82. Lukianchuk, I., et al., *Didactic principles of education students 3D-printing.* 2022.

83. Ltd, I.P., *GLASS REINFORCED POLYETHYLENE TEREPHTHALATE GLYCOL (PETG-GF)*.

84. Industries, P., *Advantages And Disadvantages Of PP Glass Filled*. April 15, 2023.

85. Chemistry, A., *High-Density Polyethylene (HDPE): A Comprehensive Scientific Overview*.

86. Ltd, I.P., *GLASS REINFORCED HIGH-DENSITY POLYETHYLENE (HDPE-GF)*.

87. Al-Atroush, M.E., et al., *Exploring the potential of 3d printing technology for sustainable plastic roads: a preliminary investigation.* Sustainability, 2023. **15**(24): p. 16777.

88. SOLUTION, M., *Polypropylene (PP) Datasheet (General Overview)*. 2025.

89. Katharina, *High-density polyethylene (HDPE): An inside look*. 2024, Linnseis.

90. Weav3D, *The WEAV3D® Process for Plastic Composites How To Make Rebar For Plastics*. 2023.

91. AASHTO, T., *209; Standard Method of Test for Theoretical Maximum Specific Gravity (Gmm) and Density of Asphalt Mixtures.* American Association of State Highway and Transportation Officials: Washington, DC, USA, 2005.

92. Highway, A.A.o.S. and T. Officials, *AASHTO T166-10-UL.* Standard Method of Test for Bulk Specific Gravity of Compacted Hot Mix Asphalt (HMA) Using Saturated Surface-Dry Specimen, AASHTO, Washington, DC, 2010.

93. HIGHWAY, A.A.O.S. and T. OFFICIALS, *Standard method of test for air voids in compacted dense and open asphalt mixtures (AASHTO T 269).* Washington, DC: AASHTO, 2012.

94. ASTM, *Standard Test Method for Residue by Evaporation of Emulsified Asphalt*, in *D6934*. 2022.

95. ODOT, *Oklahoma Department of Transportation 2019 Standard Specifications For Highway Construction.* 2019.

96. AASHTO, *Standard Method of Test for Determining the Interlayer Shear Strength (ISS) of Asphalt Pavement Layers (TP 114)*. 2023: Washington, DC.

97. ASTM, *Standard Practice for Making and Curing Concrete Test Specimens in the Laboratory*, in *C192/C192M*. 2026.

98. Owens, D.K. and R. Wendt, *Estimation of the surface free energy of polymers.* Journal of Applied Polymer Science, 1969. **13**(8): p. 1741-1747.

99. Demchenko, H., et al., *Naphthyl end-capped bithiophene film on plant-based polyamide-4, 10.* Thin Solid Films, 2024. **788**: p. 140170.

100. JONES, R.M., *Mechanics of Composite Material*. 1999.

101. Bentur, A., S. Mindess, and G. Vondran, *Bonding in polypropylene fibre reinforced concretes.* International Journal of Cement Composites and Lightweight Concrete, 1989. **11**(3): p. 153-158.

102. West, R., *Evaluation of bond strength between pavement layers.* NCAT report, 2005.

103. Adhikari, S., et al., *Thermoplastic carbon fiber reinforced polymer tapes in cementitious and polymer concretes.* Functional Composites and Structures, 2025. **7**(2): p. 025005.

104. Deb, P. and K. Lakshman Singh, *Mix design, durability and strength enhancement of cold mix asphalt: a state-of-the-art review.* Innovative Infrastructure Solutions, 2022. **7**(1): p. 61.

105. Callister Jr, W.D. and D.G. Rethwisch, *Materials science and engineering: an introduction*. 2020: John wiley & sons.

106. Bazant, Z.P. and J. Planas, *Fracture and size effect in concrete and other quasibrittle materials*. 2019: Routledge.

107. Vitalis, N. and M. Ephather, *Improvement of the algorithm for computing adjusted structure number for determination of backlog maintenance.* World Journal of Engineering and Technology, 2022. **10**(02): p. 158-178.